Thermal neutron capture gamma rays from sulfur isotopes: Experiment and theory

S. Raman, R. F. Carlton,* and J. C. Wells†
Oak Ridge National Laboratory, Oak Ridge, Tennessee 37831

E. T. Jurney and J. E. Lynn‡
Los Alamos National Laboratory, Los Alamos, New Mexico 87545
(Received 6 September 1984)

We have carried out a systematic investigation of γ rays after thermal neutron capture by all stable sulfur isotopes (^{32}S, ^{33}S, ^{34}S, and ^{36}S). The measurements were made at the internal target facility at the Los Alamos Omega West Reactor. We detected a larger number of γ rays: ~100 in ^{33}S, ~270 in ^{34}S, ~60 in ^{35}S, and ~15 in ^{37}S. Before developing detailed level schemes, we culled and then consolidated the existing information on energies and J^{π} values for levels of these nuclides. Based on the current data, we have constructed detailed decay schemes, which imply that there are significant populations of 26 excited states in ^{33}S, 70 states in ^{34}S, 20 states in ^{35}S, and 7 states in ^{37}S. By checking the intensity balance for these levels and by comparing the total intensity of primary transitions with the total intensity of secondary γ rays feeding the ground state, we have demonstrated the relative completeness of these decay schemes. For strongly populated levels, the branching ratios based on the current measurements are generally better than those available from previous measurements. In all four cases, a few primary electric dipole ($E1$) transitions account for a large fraction of the capture cross section for that particular nuclide. To understand and explain these transitions, we have recapitulated and further developed the theory of potential capture. Toward this end, we reviewed the theory relating off-resonance neutron capture to the optical-model capture. We studied a range of model-dependent effects (nature and magnitude of imaginary potential, surface diffuseness, etc.) on the potential capture cross section, and we have shown how experimental data may be analyzed using the expression for channel capture suitably modified by a factor that takes into account the model-dependent effects. The calculations of cross sections for most of the primary transitions in the sulfur isotopes are in good agreement with the data. Some discrepancies for weaker transitions can be explained well by an interfering compound-nucleus contribution to capture. This contribution is of the magnitude expected from statistical surveys of resonance capture data. Estimates of the cross section due to the valence-capture mechanism in s-wave resonances show that this cross section should dominate the more complicated compound-nucleus contributions.

I. INTRODUCTION

We have carried out a systematic investigation of γ rays following thermal neutron capture by all stable sulfur isotopes (^{32}S, ^{33}S, ^{34}S, and ^{36}S). We began with a study of the ^{33}S(n,γ) reaction, the initial aim being the determination of the neutron separation energy (S_n) of ^{34}S. This value, together with the proton separation energy (S_p) of ^{34}Cl from an independent ^{33}S(p,γ) measurement, yielded an accurate energy for the $^{34}\text{Cl} \rightarrow {}^{34}\text{S}$ superallowed β decay.[1] In the process of determining $S_n(^{34}\text{S})$, a great deal of spectroscopic information was amassed on the energy levels in ^{34}S. The ^{33}S(n,γ) study was soon extended to include studies of the ^{32}S(n,γ) and the ^{34}S(n,γ) reactions, at first because they helped to identify interfering γ rays and later because they were interesting in themselves. Recently, we have also studied the ^{36}S(n,γ) reaction to complete the series, and the results have been reported separately.[2] Brief descriptions of the above (n,γ) measurements on all stable S isotopes have also been presented elsewhere.[3]

The study of (n,γ) reactions has traditionally and consistently yielded significant level information, and the current experiment is no exception. At one extreme, the relatively simple γ-ray spectrum from the ^{34}S(n,γ) reaction contained nearly 60 γ rays. These could be incorporated into a ^{35}S level scheme consisting of only 20 excited states. At the other extreme, the complex spectrum from the ^{33}S(n,γ) reaction contained over 270 γ rays, and the resulting ^{34}S level scheme required nearly 70 excited states. The ^{32}S(n,γ) reaction was intermediate with over 100 γ rays and 26 excited states. This relative complexity was expected because for the isotopes studied the neutron separation energy of ^{35}S is lowest (S_n = 6986 keV), that for ^{34}S is highest (S_n = 11417 keV), and that for ^{33}S is intermediate (S_n = 8642 keV). Going beyond this vast amount of spectroscopic information, it is noted that in all three cases a few primary transitions account for the bulk of the capture cross section—5 transitions in ^{35}S account for 94% of the cross section; 8 in ^{34}S, for 54%; and 6 in ^{33}S, for 94%. The physics of the capture process is contained in these primary transitions, and we have devoted considerable attention to understanding them.

The most significant primary γ transitions occurring in the slow neutron-capture process are normally of electric dipole ($E1$) and magnetic dipole ($M1$) character. With this limitation on the multipolarity, analysis of the

experimental data on slow neutron capture has shown considerable evidence for the importance of single-particle effects in such transitions—i.e., the transition strength has the properties associated with the transition of a single nucleon moving in the potential field of an otherwise apparently inert core formed from the remainder of the nucleons in the system. This picture is to be contrasted with that explaining $E1$ transitions (for example) of much higher energy, in which a collective state of isovector character involving many particle-hole pairs with a special phase relationship is formed by the particle-hole interactions in the major nucleon shells. Indeed, the giant resonance effect thus created in this latter picture is believed to be sufficiently broadly spread over the individual states of the compound nucleus that even in its wings this resonance will account for the bulk of the transitions observed at the much lower γ-ray energies involved in slow neutron capture. Nevertheless, there are sufficient anomalies in the experimental data as compared with the transition strengths to be expected in the giant resonance model (or indeed in other models that can be expressed in a statistical form) to have led to a series of papers on single-particle effects in slow neutron capture stemming from the work of Lane and Lynn.[4]

These first papers dealt principally with the notion of a smooth background cross section underlying the sharply fluctuating resonance capture in which more complicated compound nucleus mechanisms are involved, but the concept of a simple "valence" mechanism in the resonances involving a simple transition of a neutron in the field of the target nucleus was also invoked. The theory of the valence mechanism was elaborated more fully in later works by Lynn,[4] by Cugnon and Mahaux,[5] and by Allen and Musgrove.[6] The first significant experimental results confirming the existence of valence capture were reported by Mughabghab *et al.*[7] for p-wave resonances in ^{98}Mo and ^{92}Mo. More data on ^{98}Mo, not only confirming the predominance of valency capture in strong resonances but also revealing its limitations in weak resonances, were presented by Chrien *et al.*,[8] while a clear case of the operation of the valence mechanism in an s-wave resonance was described by Raman *et al.*[9] from a study of the ^{54}Fe(n,γ) reaction.

Meanwhile the formal theory of direct and valency capture, emphasizing particularly the dependence of correlations between neutron and radiation widths on the existence of doorway states and the importance of threshold effects in suppressing the contribution of excited states of the target nucleus to the valence nucleon transition strength, was developed further in a series of papers by Lane[10] and by Lane and Mughabghab.[11] Further experimental evidence on direct single-neutron-transition effects in off-resonance thermal neutron capture was compiled particularly by Mughabghab,[12] who showed that the channel-capture approximation (with only the extranuclear contribution to the matrix element taken into account) was remark-

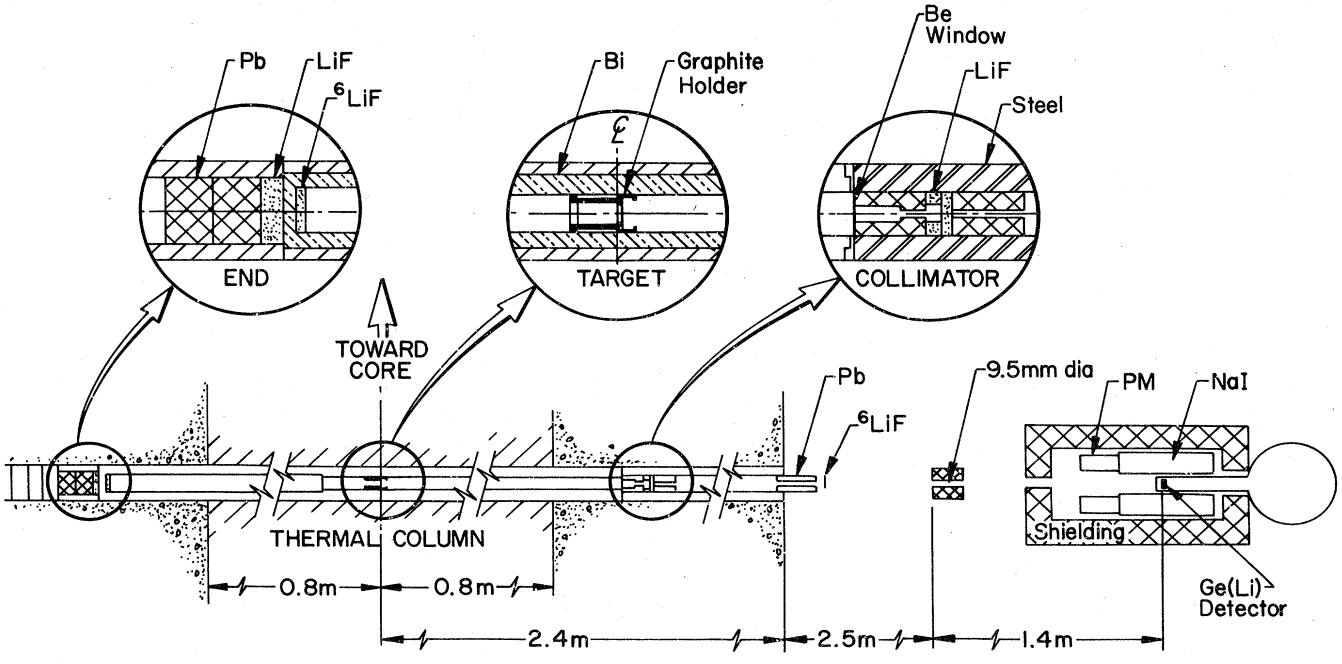

FIG. 1. Experimental arrangement of the target, collimator, and detector at the Los Alamos Omega West Reactor.

ably successful in explaining the cross sections for a number of $E1$ transitions in the $^{136}Xe(n,\gamma)$ reaction, and by Kopecky, Spits, and Lane,[13] who demonstrated that the correlation between (d,p) and reduced (n,γ) strengths to common final states of ^{38}Cl was strongest when the radiation strengths were assumed to have a linear dependence on γ-ray energy, as given by the hard-sphere approximation (extranuclear capture associated with the limiting case of hard-sphere scattering) to the direct capture theory.

The current data are characterized by their high precision and therefore seem able to provide a critical test of current theory. For this purpose, the theory is rather fully recapitulated in a definitive way and somewhat further developed with special emphasis placed on assessing its ability and accuracy.

II. CAPTURE FACILITY

A. Reactor

Figure 1 shows schematically the internal target facility at the Los Alamos Omega West Reactor. The normal target position is at the center line of the graphite thermal column, approximately 1.5 m from the edge of the reactor core. The entire thermal column is shielded from core γ rays by thicknesses of 7.6 cm of Pb and 12.7 cm of Bi between the core and the column. At the nominal 8-MW reactor power level, the thermal neutron flux at the target position is $\approx 6 \times 10^{11}$ n/cm^2 s and the Cd(In) ratio is ≈ 2000. The thermal flux approximates a Maxwellian distribution corresponding to a temperature of 350 K, for which the most probable neutron velocity is 2400 m/s.

The channel into which targets are inserted is built onto a graphite skid that replaces one of the transverse thermal-column graphite stringers. The walls of the channel are of Pb-plated Bi and are designed to attenuate the equilibrium γ intensity at the target position. Collimation of the γ rays from the target is such that capture γ rays from the channel wall do not reach the detector. The end wall of the channel (opposite the detector) is recessed into the reactor shield and covered with a disk of LiF to reduce greatly neutron captures that would otherwise contribute to background. Any γ rays originating in the reactor core must, because of the transverse arrangement of the collimation, undergo at least one scattering to reach the detector. The entire channel is evacuated to eliminate background γ rays from neutron capture in the nitrogen and argon constituents of air. Thermal neutrons in the collimated γ beam are screened with an external disk of 2.5-mm-thick ^6LiF. Targets to be studied are contained in graphite holders of 3.4 cm diam that can easily be inserted into or extracted from the channel after the primary collimator is removed. Graphite is especially suitable for this use because of its low neutron capture cross section and simple capture γ spectrum. An external collimator built into a cylinder of Pb shields the detector from γ rays that might stream through incomplete mating of the surfaces of the removable shielding pieces that surround the primary collimator.

TABLE I. Energies and intensities of γ rays from the $^{34}S(n,\gamma)^{35}S$ reaction.

Energy[a] (keV)		Intensity[b]		Energy[a] (keV)		Intensity[b]		Energy[a] (keV)		Intensity[b]		Energy[a] (keV)		Intensity[b]	
356.66[c]	9	0.110	12	1250.61	5	0.63	7	2555.492	14	9.1	9	4188.96	4	8.0	8
368.5	4	0.06	2	1381.67[d]	24	0.070	24	2615.2[f]	2	3.2[f]	3	4268.65	14	1.00	12
619.23	19	0.122	22	1404.967	24	1.76	17	2616.8[f]	3	0.7[f]	2	4637.91	4	163	15
631.32[c]	24	0.175	25	1454.09	4	1.33[e]	32	2716.99	16	0.89	13	4902.96	4	11.0	11
663.41[d]	7	0.266	30	1566.7	3	1.38	25	2796.73	4	15.9	15	4962.63	5	8.6	8
692.16	5	0.39	5	1572.333	7	103	10	2905.1	4	0.41	11	5752.0	8	0.052	15
775.398	6	46	5	1760.55	11	0.43	6	2938.58	11	2.62	27	6018.2	6	0.06	2
803.81[d]	9	0.27	4	1841.426	15	6.3	6	2972.0	4	0.54	17	6077.87	11	1.06	11
863.28	28	0.10	3	1964.8	2	1.1[e]	3	3139.9	5	0.23	7	6293.2	4	0.19	4
907.607	14	1.79[e]	30	1991.27	5	1.59	16	3183.94	4	18.2	17	6355.0	6	0.136	20
1084.79	15	0.16	3	2022.954	9	33.6	30	3330.80	4	21.8	21	6419.3	11	0.048	15
1101.92	31	0.096	23	2082.681	12	46	5	3390.55	5	16.2	15	6628.5	6	0.089	16
1144.591	20	1.63	16	2229.510	16	8.4	8	3558.1	5	0.25	5	6760.3	12	0.056	22
1161.05	20	0.161	24	2347.701	11	148	13	3801.74	3	9.1	9	6985.7	10	0.106	23
1210.28	4	0.74	8	2508.39	8	1.11	12	4105.3	8	0.14	5				

[a] In our notation, 356.66 *9* is 356.66 ± 0.09 keV, etc. See Section III for a detailed discussion of uncertainties in the energy and intensity values presented in this paper.

[b] γ-ray cross section in mb. Multiply by 0.340 to obtain photons per 100 thermal neutron captures. In our notation 0.110 *12* is 0.110 ± 0.012, etc.

[c] γ ray placed more than once on the level scheme.

[d] γ ray not placed on the level scheme.

[e] After corrections due to a γ ray of similar energy in the $^{32}S(n,\gamma)^{33}S$ reaction.

[f] Peak observed at 2615.49 *4* with intensity 3.9 *4* was reanalyzed as a doublet.

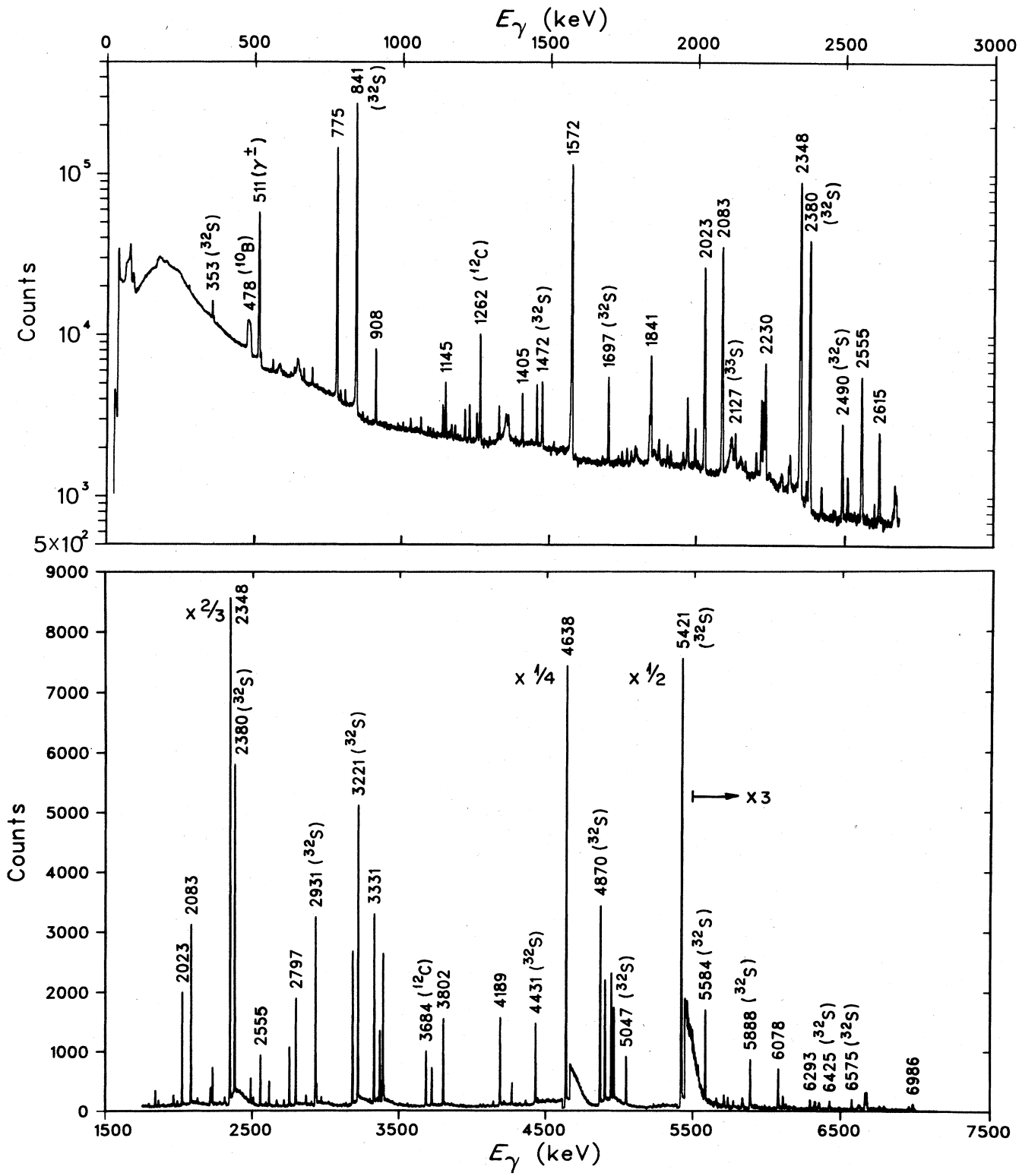

FIG. 2. Gamma-ray spectra from thermal neutron capture by ^{34}S. The Ge(Li) detector was operated either in the Compton-suppression mode (top part) or in the pair-spectrometer mode (bottom part). All energies are in keV. The peaks with energy labels but without isotope labels arise from the ^{34}S target. A more detailed list of γ rays observed in ^{35}S is given in Table I.

B. Detector

The 26-cm^3 coaxial Ge(Li) detector is positioned inside a 20-cm-diam by a 30-cm-long NaI(Tl) annulus. The annulus is optically divided lengthwise so that at energies >2 MeV the system can be operated as a double-escape spectrometer. In this mode, only double-escape peaks appear in the pulse-height spectrum, and, in addition, continuum background is substantially reduced. At lower energies the two annulus halves are connected together electrically, and the system is operated in a conventional anticoincidence mode for the suppression of continuum background caused by the escape of Compton-scattered photons. The entire detector system is housed in a cylindrical shield of lead and steel having a wall thickness of 10 cm. The detector preamplifier signals are fed into a Tennelec TC-205 amplifier and a 4096-channel analyzer. The system gain is stabilized by a precision double pulser. In the pair-spectrometer mode, the gain was fixed at 1.30 keV per channel; in the Compton suppressed mode, it was fixed at 0.65 keV per channel. The system resolution (full width at half maximum) was typically 2.3 keV at 1 MeV, 5.5 keV at 6 MeV, and 8.8 keV at 11 MeV. The pulse-height data were analyzed on a CDC-6600 computer.

III. CALIBRATIONS

A. Energy calibrations

It is necessary to make corrections for the system nonlinearity, which arises mainly in the analog-to-digital converter, to arrive at the unknown γ-ray energies from known standard energies. We have applied the same general procedure in determining corrections for both modes of operation of the system. Using a spectrum of precisely known γ rays appropriate to the range of energies of interest, we choose two well-spaced energies and establish a linear energy-channel relationship. The remainder of the γ rays are used to generate a correc-

TABLE II. Previously reported levels in ^{35}S.

Level energy[a] (keV)		J^{π} [b]	Excited in which experiment	Level energy[a] (keV)		J^{π} [b]	Excited in which experiment
0.0		$3/2^+$	(d,$\alpha\gamma$), (d,p), (d,pγ), (p,^{3}He), (n,γ)	**4903.5**	*3*	$1/2^-$	(d,p), (n,γ)
1572.20	*12*	$1/2^+$	β-decay, (d,$\alpha\gamma$), (d,p), (d,pγ), (p,^{3}He), (n,γ)	**4963.2**	*3*	$3/2^-$	(d,p), (p,^{3}He), (n,γ)
				4990	*30*		(p,^{3}He)
1991.5	*7*	$7/2^-$	(d,$\alpha\gamma$), (d,p), (d,pγ), (p,^{3}He)	5058	*8*	$7/2^-$	(d,p)
2347.6	*2*	$3/2^-$	(d,$\alpha\gamma$), (d,p), (d,pγ), (n,γ)	5126	*11*		(d,p), (p,^{3}He)
2718.0	*6*	$5/2^+$	(d,$\alpha\gamma$), (d,p), (d,pγ), (p,^{3}He), (n,γ)	5342	*8*		(d,p), (p,^{3}He)
2939	*3*	$3/2^+$,$5/2^+$	(d,$\alpha\gamma$), (d,p), (d,pγ), (p,^{3}He)	5475?	*10*		(d,p)
3421.0	*10*	$5/2^+$	(d,$\alpha\gamma$), (d,p), (d,pγ), (p,^{3}He)	5542	*8*		(d,p), (p,^{3}He)
3563	*3*		(d,$\alpha\gamma$), (d,p), (d,pγ)	5771	*30*		(p,^{3}He)
3598	*2*		(d,$\alpha\gamma$), (d,p), (d,pγ), (p,^{3}He)	5915?	*30*		(p,^{3}He)
3675	*10*		(d,p)	5980	*20*		(d,p)
3802.2	*3*	$3/2^-$	(d,$\alpha\gamma$), (d,p), (d,pγ), (n,γ)	**6078.3**	*5*		(d,p), (n,γ)
3818	*3*		(d,$\alpha\gamma$), (d,pγ), (p,^{3}He)	6129	*30*		(p,^{3}He)
3866?	*10*		(d,p)	**6292**	*8*		(d,p)
3886	*2*		(d,$\alpha\gamma$), (d,p), (d,pγ)	6339.5	*6*		(d,p), (p,^{3}He), (n,γ)
3907	*10*		(d,p)	**6344**	*8*		(d,p)
4025.5	*15*		(d,$\alpha\gamma$), (d,p), (d,pγ), (p,^{3}He)	6446	*8*		(d,p)
4108	*2*		(d,$\alpha\gamma$), (d,p), (d,pγ), (p,^{3}He)	6496	*8*		(d,p)
4189.9	*3*	$1/2^-$	(d,$\alpha\gamma$), (d,p), (d,pγ), (p,^{3}He), (n,γ)	6543	*8*		(d,p)
4304	*3*		(d,$\alpha\gamma$), (d,p), (d,pγ), (p,^{3}He)	6584	*8*		(d,p)
4482	*2*	$7/2^-$	(d,$\alpha\gamma$), (d,p), (d,pγ), (p,^{3}He)	**6634**	*8*		(d,p), (p,^{3}He)
4575	*8*		(d,p), (p,^{3}He)	6677	*8*		(d,p), (p,^{3}He)
4617	*30*		(p,^{3}He)	6892	*10*		(d,p)
4837	*8*		(d,p), (p,^{3}He)	7022	*10*		(d,p)

[a] In our notation 1572.20 *12* is 1572.20 ± 0.12 keV, etc. If a correspondence can be established with a level determined in the present experiment, the entry is given in bold type.

[b] Detailed references are as follows: (d,$\alpha\gamma$) - Th. W. van der Mark and L. K. ter Veld, Nucl. Phys. **A181**, 196 (1972); (d,p) - C. E. Moss, Nucl. Phys. **A131**, 235 (1969), J. G. van der Baan and H. G. Leighton, Nucl. Phys. **A170**, 607 (1971); (d,p) vector analyzing power - R. Abegg and S. K. Datta, Nucl. Phys. **A287**, 94 (1977); (d,pγ) - K. S. Burton and L. C. McIntyre, Jr., Nucl. Phys. **A154**, 551 (1970), Th. W. van der Mark and L. K. ter Veld, Nucl. Phys. **A181**, 196(1972), R. M. Freeman, R. Faerber, M. Toulemonde, and A. Gallmann, Nucl. Phys. **A197**, 529 (1972);(p,^{3}He) - A. Guichard, H. Nann, and B. H. Wildenthal, Phys. Rev. C **12**, 1109 (1975); (n,γ) - Dzh. D. Dzhafar, A. A. Abdullah, N. Kh. Al-Kuraishi, M. S. Al'vash, M. A. Khalil, and A. M. Demidov, Yad. Fiz. **15**,1093 (1972) [transl.: Sov. J. Nucl. Phys. **15**, 605 (1972)]; (β^- decay) - K. E. Apt and J. D. Knight, Phys. Rev. C **6**, 842 (1972). For an independent evaluation of ^{35}S levels, see P. M. Endt and C. van der Leun, Nucl. Phys. **A310**, 1 (1978).

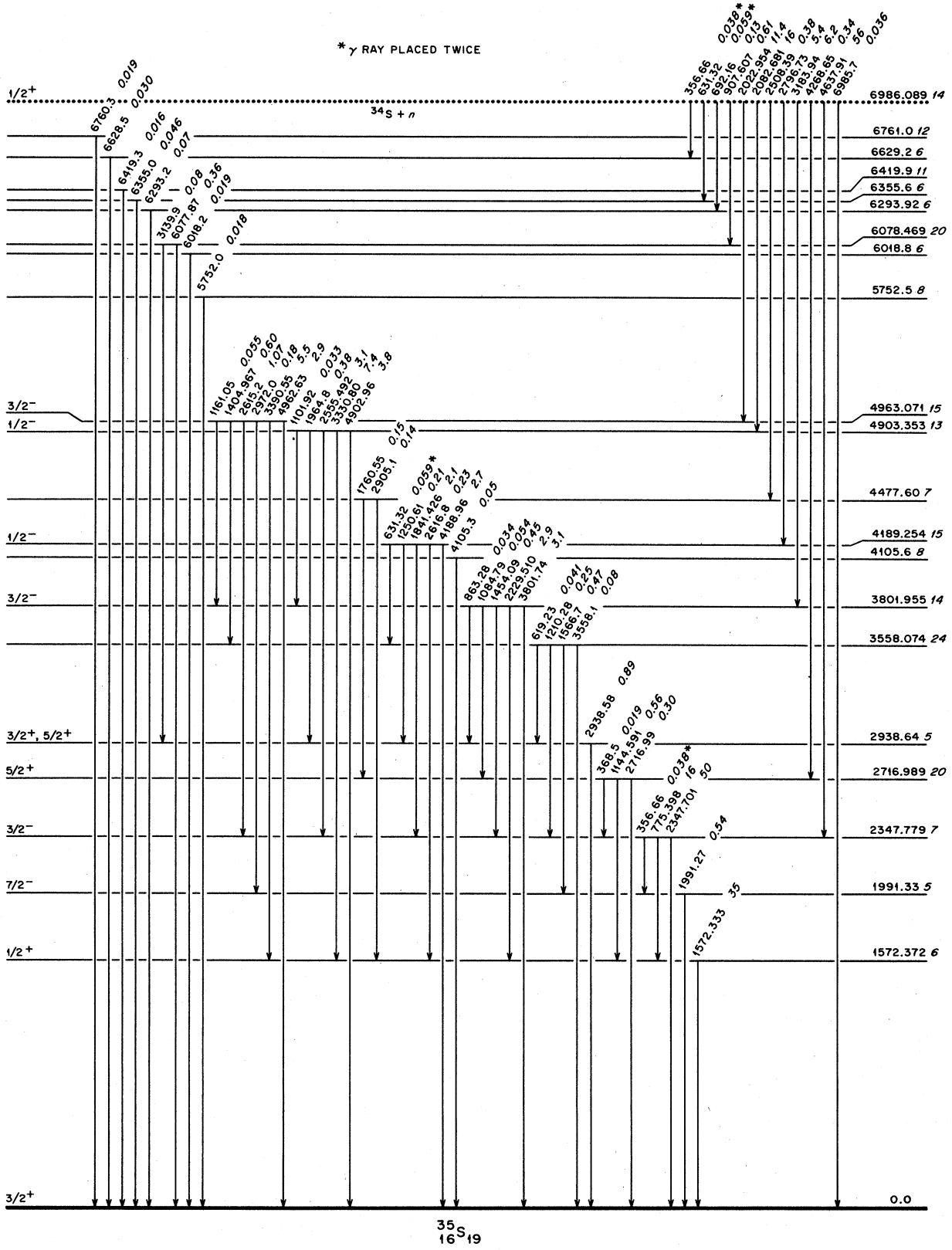

FIG. 3. Level scheme for ^{35}S based on the current measurements. All energies are in keV. The italic numbers next to the γ-ray energies refer to absolute intensities per 100 neutron captures. In our notation for level energies, 1572.372 *6* = 1572.372 ± 0.006 keV, etc. In deducing these level energies, nuclear recoil has been taken into account.

tion curve of deviations from perfect linearity. In the double-escape mode, we find it convenient to use the prompt γ-ray spectrum from neutron capture in melamine ($C_3H_6N_6$). Energies of capture γ rays from all three constituents are well known[1] and extend from under 2 MeV to nearly 11 MeV. In the anticoincidence mode, the prompt γ rays from ^1H plus those from a set of radioactive sources are employed.

In applying this technique, it is necessary to record the spectrum from the target under study simultaneously with the calibration γ rays to ensure against drifts in the system gain. At this stage in the procedure, the energies of prominent γ rays in the unknown spectrum are precisely determined and are subsequently used as secondary standards in determining the energies of weaker γ rays in a spectrum recorded without the calibration γ rays.

The energies of the γ rays above 2 MeV given in this paper are based on a mass-doublet standard scale derived from the neutron binding energies[14] of ^2H, ^{13}C, and ^{15}N. This scale and a subsequent ^{198}Au(411.8044 $\pm$ 0.0011 keV) standard scale are discussed in a separate publication.[1] The adoption of the latter standard will result in a lowering of the vast bulk of the >2-MeV γ-ray energies reported in this paper by approximately 50 eV. Because the construction of level schemes depends more on energy differences than on absolute energy values, we have made no attempt to convert our values to the ^{198}Au standard even though indications are strong that this standard may be more valid.[1,15] For the same reasons, we have quoted only the statistical uncertainties in presenting the measured γ-ray energies. By combining the uncertainties in the calibration standards themselves and the above systematic change, we conservatively estimate that an additional uncertainty of 0.1 keV should apply to the γ-ray energies and level energies presented in this paper. Our final values, including all uncertainties, for the neutron separation energies of ^{33}S, ^{34}S, ^{35}S, and ^{37}S have been given already in Ref. 1.

B. Intensity calibrations

All capture cross sections reported here are based on σ_γ(2200 m/s) = 332 $\pm$ 0.002 mb for ^1H (Ref. 16). Because the most probable neutron velocity is greater than 2200 m/s, we assume a $1/v$ dependence of the capture cross section of ^1H and of the S isotopes. The spectrum from a 180-mg target of CH_2 placed at the normal target position in the thermal column was recorded either just preceding or just after recording that part of the spectrum (from each S isotope) which included the 2.2-MeV region. The partial cross sections of prominent γ rays from S isotopes thus determined relative to ^1H were employed, in turn, to determine the cross sections for all remaining lines by a bootstrapping procedure. The effect of possible variations in neutron flux was eliminated by measuring the neutron fluence for each run with a small fission counter located near the target position in the thermal column.

The energy dependence of detector efficiency in the Compton-suppressed mode was determined from a set of standard radioisotopic sources with precalibrated γ-ray intensities. The efficiency curve in the double-escape mode was derived from the relative intensities of the γ rays from $^{14}N(n,\gamma)$ as discussed in Ref. 17.

Our stated uncertainties in the partial capture cross-section values are composed of a 7% minimum uncertainty combined with a statistical uncertainty related to the measured number of counts under a given peak. The minimum uncertainty is the algebraic sum of 3% related to the cross section (approximately 1% each for the hydrogen standard, fluence measurements, and the bootstrapping procedure) and 4% related to the efficiency curve, which had to span from 90 keV to 11.5 MeV.

IV. RESULTS: $^{34}S(n,\gamma)^{35}S$

A. γ rays in ^{35}S

The (n,γ) measurements were made with a 1.09-g, 77.7% enriched ^{34}S target. Approximately 60 γ rays were observed (see Table I), some with intensities as low as 0.05 mb ($\approx$2 photons per 10^4 captures). The spectrum is shown in Fig. 2. Twenty of these γ rays (especially the strong ones) have been observed also by Jafar *et al.*,[18] who employed a 1.5-g, 97% enriched ^{34}S target. This study is the only previously known relevant study of the $^{34}S(n,\gamma)$ reaction with thermal neutrons. The

TABLE III. Gamma-ray intensity balance in the reaction $^{34}S(n,\gamma)^{35}S$.

E(level) (keV)	Intensity in (mb)	Intensity out (mb)	Intensity net (mb)
0	294		
1572	96	102	−6
1991	2.0	1.6	0.4
2348	184	194	−10
2717	1.6	2.6	−1.0
2939	2.3	2.6	−0.3
3558	1.9	2.5	−0.6
3802	18.5	19.1	−0.6
4106		0.1	−0.1
4189	15.9	15.8	0.1
4478	1.1	0.8	0.3
4903	46	43	3
4963	34	30	4
5752		<0.1	−<0.1
6019		<0.1	−<0.1
6078	1.8	1.3	0.5
6294	0.4	0.2	0.2
6356	<0.2	0.1	<0.1
6420		<0.1	−<0.1
6629	<0.1	0.1	0.0
6761		<0.1	−<0.1
6986		282	

agreement between the current study and that by Jafar *et al.*[18] is excellent. A γ ray at 646.9 keV with intensity $\approx$2 mb, reported in the latter study as belonging to ^{35}S, was not observed and probably belongs to ^{37}S instead. A γ ray at 646.2 keV is the strongest transition observed in the ^{36}S(n,γ) reaction.[2] Interfering γ rays (see Fig. 2) arose mainly from ^{12}C (in the graphite target-holder) and from ^{32}S (21.8% of the target material).

B. Known energy levels in ^{35}S

The construction of a level scheme based on (n,γ) data is somewhat akin to solving a jigsaw puzzle. Because the problem is rendered easier to the extent to which the energy levels and their branching ratios have been determined, it behooves us to make as detailed an evaluation of the literature as possible concerning the known energy levels in ^{35}S. This we have done as shown in Table II, which also contains detailed references. Each and every level listed there which could reasonably be expected to receive population in the (n,γ) reaction was checked against the γ-ray data. With the aid of computers, this process was straightforward, though laborious.

The spin and parity (J^π) assignments listed in Table II are mainly from the work of Abegg and Datta,[19] who studied the angular distribution of vector-analyzing power and cross section for the reaction ^{34}S$(\vec{d},p)$ utilizing vector-polarized 11.8-MeV deuterons. The spectroscopic factors obtained by them are invoked later in this paper for all levels except the poorly resolved 4903- and 4963-keV levels. For this doublet, we have employed the spectroscopic factors determined recently by Piskoř *et al.*[20]

C. Level scheme for ^{35}S

Figure 3 shows the level scheme based on the current data. All but three of the γ rays listed in Table I have been incorporated into this scheme, which consists of 20 excited states. Fifteen of these states correspond to known levels (see Table II). The five new ones are at 4478, 5752, 6019, 6420, and 6761 keV. Because the S_n (^{35}S) value is 6986 keV and because there are no known low-lying levels below 1572 keV, the 5752-, 6018-, 6419-, and 6760-keV transitions (see Fig. 3) are perforce ground-state transitions from levels at these energies (except for recoil correction). Low-energy primary transitions to these levels are expected to be weak (from intensity balance) and below the detection limits of the current experiment.

The three unplaced transitions of energies 663, 804, and 1382 keV, though weak, are probably genuine because they do not correspond to either prompt or delayed impurity lines.[21] These transitions cannot be placed anywhere among the bound states shown in Fig. 3. The most plausible explanation for them is that they are primary transitions leading to levels (not shown in Fig. 3) at 6323, 6294, and 5604 keV, respectively. The intensities out of these levels are expected to be fractionated so that the corresponding secondary γ rays again fall below our detection limits.

The 4478-keV level shown in Fig. 3 is based on good energy fit and intensity balance involving the 2508-keV primary transition and the 2905- and 1761-keV secondary transitions. If the placement of the 2508-keV γ ray is correct, the 4478-keV level cannot be $7/2^-$ because the capturing state is $1/2^+$. The $7/2^-$ assignment is from (d,p) studies.[19] However, $(p,^3\text{He})$ studies[22] indicate positive parity for a level around this energy. The $l_n = 3$ fit for this level in (d,p) is quite poor. The existence of a narrow level doublet at $\approx$4480 keV thus becomes a distinct possibility.

The five strongest primary transitions of energies 4638, 3184, 2797, 2083, and 2023 keV are definitely $E1$ transitions (see Fig. 3). Primary $E2$ transitions are very rare in (n,γ) reactions,[17] but a fairly strong (0.34%) $E2$ transition was observed to populate the 2717-keV level. An extremely weak (0.036%) $M1$ transition was also observed to directly populate the ^{35}S ground state.

TABLE IV. Gamma-ray branching ratios (in %) of selected ^{35}S levels (E_x in keV).

J_i	E_{x_i}	$J_f\rightarrow$ / $E_{x_f}\rightarrow$ 3/2+ 0	1/2+ 1572	7/2− 1991	3/2− 2348	5/2+ 2717	3/2+,5/2+ 2939	3558	3/2+ 3802
7/2−	1991	≈100	<2						
3/2−	2348	76 *2*	24 *1*	<0.1					
5/2+	2717	35 *5*	63 *2*	<2	2 *1*				
3/2+,5/2+	2939	≈100	<2	<4	<2	<2			
	3558	10 *2*	<5	55 *6*	30 *2*	a	5 *1*		
3/2+	3802	48 *3*	44 *3*	<0.5	7 *1*	0.8 *2*	0.5 *2*	<0.3	
1/2−	4189	51 *3*	4 *2*	<2	40 *2*	<2	4 *1*	<2	<1
	4478		49 *14*			51 *7*			
1/2−	4903	25 *2*	51 *2*	<0.3	21 *2*	<0.3	3 *1*	<0.3	<0.2 *1*
3/2−	4963	28 *2*	53 *3*	2 *1*	10 *1*	<0.3	a	6 *1*	0.5 *1*

[a]Obscured by a nearby strong peak.

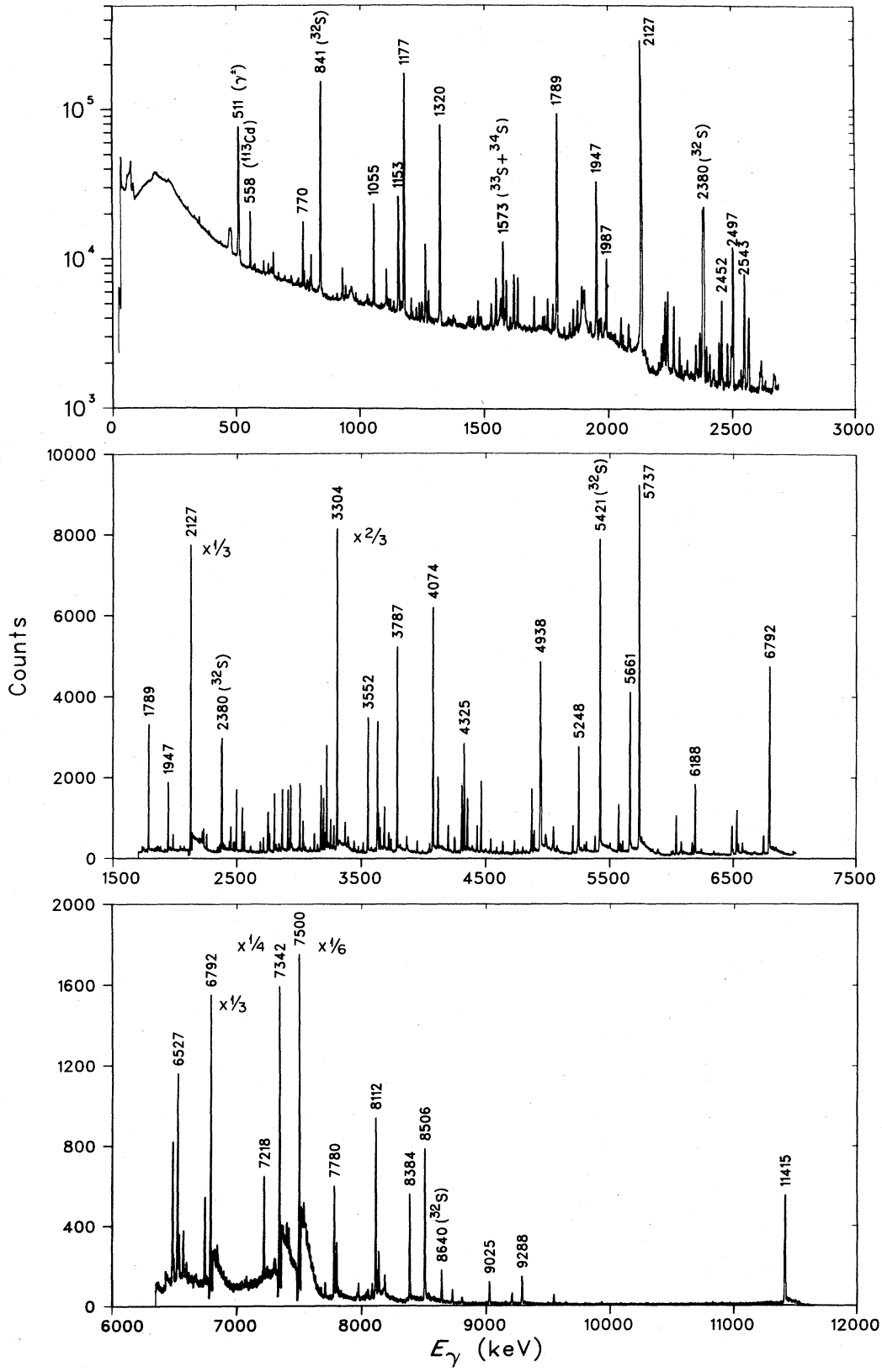

FIG. 4. Gamma-ray spectra from thermal neutron capture by ^{33}S. The Ge(Li) detector was operated either in the Compton-suppression mode (top part) or in the pair-spectrometer mode (middle and bottom parts). All energies are in keV. The peaks with energy labels but without isotope labels arise from the ^{33}S target. A more detailed list of γ rays observed in ^{34}S is given in Table V.

TABLE V. Energies and intensities of γ rays from the $^{33}S(n,\gamma)^{34}S$ reaction.

Energy[a] (keV)		Intensity[b]		Energy[a] (keV)		Intensity[b]		Energy[a] (keV)		Intensity[b]		Energy[a] (keV)		Intensity[b]	
95.45[c]	18	0.012	3	1564.8	5	0.91	20	2749.24	5	7.0	7	4252.38	22	1.23	15
229.71[c]	16	0.054	10	1572.57	5	5.6[e]	6	2753.3	13	0.93[f]	23	4306.44	6	8.3	8
281.34	24	0.023	8	1580.50	6	0.66	7	2762.10	8	3.0	3	4325.397	30	12.7	12
306.63	16	0.089	20	1585.510	20	2.52	23	2801.33	5	10.1	10	4350.85	9	6.2	7
334.21	15	0.042	10	1602.06	15	0.43	7	2810.3[c]	3	0.87	13	4391.77	29	0.44	9
392.28	11	0.124	20	1615.24	10	2.25	27	2817.76[d]	25	0.84	13	4462.44	20	7.9	8
516.86	12	0.32	5	1617.00	12	1.94	25	2839.3	4	1.00	16	4499.7	10	0.23	7
571.7	6	0.08	3	1627.2	10	0.19	7	2843.7	6	0.59	13	4532.6	7	0.23	7
576.80	19	0.146	21	1631.641	25	2.88	27	2864.56	4	10.9	11	4540.68	15	1.70	20
612.16	5	0.263	28	1640.7	10	0.17	10	2910.28	5	10.0	10	4568.9	4	0.30	6
631.13	6	0.283	31	1732.39	11	0.44	6	2919.7	5	0.43	11	4588.37	26	0.59	10
672.00	10	0.152	20	1739.32	9	0.48	6	2940.42	31	1.05	15	4624.2	5	0.21	5
698.18	13	0.101	14	1751.431	29	1.44	14	2945.8[d]	10	0.30	9	4670.1	6	0.11	6
722.95	14	0.175	22	1772.82	4	1.40	14	2989.9	7	0.18	9	4731.37	10	1.58	16
725.25	22	0.115	19	1788.794	20	79	8	2995.8	6	0.37	10	4758.79	27	0.46	8
743.50[c]	20	0.098	15	1795.28[d]	30	0.19	5	3005.39	5	10.0	10	4799.11	28	0.52	8
748.43	14	0.127	17	1818.96	14	0.38	6	3022.0	10	0.16	9	4826.0	5	0.11	5
752.30[c]	8	0.222	26	1840.52	12	0.56[e]	9	3031.69	8	4.6	6	4889.30	8	2.68	26
767.20	21	0.098	16	1854.28	4	1.28	13	3038.18	32	1.27	17	4903.4	5	0.28[e]	8
770.428	20	2.75	25	1871.04	8	2.04	22	3051.83[c]	26	0.64	12	4938.06	3	22.2	21
789.1	6	0.39	7	1887.66[c]	4	1.78	17	3089.53	26	0.56	11	4982.44	20	1.31	14
798.92	10	0.29	4	1922.92	22	0.61	11	3122.65	15	2.7	4	4988.6	4	0.63	9
803.103	27	1.14	11	1925.94	17	0.28	8	3149.29[c]	15	0.89	12	5036.4	7	0.25	6
846.1	13	0.28	18	1947.060	20	29.2	26	3174.37	5	10.5	10	5043.3	4	1.59	26
925.79	14	0.171	21	1951.77	19	0.53	11	3183.9	7	0.12[e]	8	5074.79	25	0.42	8
929.436	21	1.07	10	1959.67	17	0.88	11	3194.74	5	7.4	8	5084.2	5	0.14	5
941.59	6	0.41	5	1980.15[c]	12	0.64	9	3211.69	9	2.36	23	5202.06	6	3.00	29
982.68	9	0.187	27	1984.2[c]	4	0.50	14	3231.89	20	0.84	11	5239.8	4	0.65	9
989.08[d]	28	0.079	23	1987.19	3	6.5	7	3241.9	5	0.36	7	5247.94	4	11.8	11
1029.23[c]	8	0.32	4	1998.3	4	0.14	5	3253.21	6	3.8	4	5268.9[d]	6	0.27	7
1035.82[c]	17	0.108	31	2046.29[c]	5	1.78	18	3278.79	11	3.2	4	5294.94	24	0.42	8
1055.491	20	7.0	7	2053.94	14	0.59	9	3304.031	20	63	6	5311.10	15	0.80	10
1105.673	21	1.49	14	2076.89	8	1.48	16	3311.6	5	0.62	11	5380.59	9	1.97	20
1113.27	9	0.41	6	2127.499	20	318	29	3392.86	24	1.57	19	5501.4	5	0.46	9
1121.33	9	0.35	5	2152.41	23	0.17	5	3442.24	25	1.02	16	5569.30	5	5.6	6
1153.492	20	10.0	9	2173.55	21	0.16	5	3451.5	9	0.35	10	5602.78	15	1.15	14
1156.39	7	1.57	18	2209.10	6	0.86	9	3476.95	18	0.71	10	5660.78	6	18.4	18
1164.83[c]	25	0.21	6	2230.14	14	0.80[e]	10	3500.3	5	0.48	11	5736.76	4	43	4
1176.650	20	75	7	2233.49	4	5.0	5	3515.07	11	1.43	16	5755.5	5	0.51	8
1205.05	4	0.61	6	2258.430	23	3.7	4	3552.08	4	17.34	17	5847.4	5	0.25	6
1210.04	13	0.162	22	2282.17[c]	4	1.70	16	3581.2	4	0.37	7	5884.6	6	0.27	6
1237.61	5	0.52	6	2290.26	15	0.27	5	3628.10	4	17.6	16	5997.30	31	0.34	6
1244.32	21	0.120	26	2326.2[d]	10	0.05	4	3635.83	8	5.2	6	6010.3	3	0.50	8
1247.92	6	0.59	7	2328.8	5	0.14	4	3644.8	8	0.48	10	6035.68	7	4.4	5
1266.11	5	0.66	7	2353.06	21	0.23	4	3649.88	12	3.11	31	6077.27	12	1.19	13
1274.30	4	1.17	11	2363.97	8	2.1	11	3664.8	4	0.47	10	6094.4	4	0.21	5
1277.81[c]	18	0.190	26	2375.657	20	26.0	24	3719.68	16	1.91	20	6152.1	5	0.18	5
1320.169	20	38	4	2390.82	6	1.33	14	3738.69	17	1.18	17	6166.24	13	1.55	17
1325.22	26	0.33	7	2404.04	6	1.07	11	3787.096	20	26.5	25	6188.45	6	8.7	9
1353.46	16	0.38	5	2441.31[c]	4	1.75	17	3812.0	5	0.25	6	6236.3	11	0.19	5
1364.4	4	0.32	9	2451.557	20	5.2	5	3864.25	11	1.68	17	6241.0	5	0.45	7
1374.34	20	0.37	8	2475.15[c]	4	1.71	17	3870.51	31	0.56	8	6341.58	32	0.45	8
1435.00[c]	11	0.30	5	2490.6	13	0.62[f]	16	3949.27	12	1.54	17	6487.48	6	3.6	4
1443.05[c]	10	0.37	5	2496.726	20	15.4	14	3990.7	7	0.29	7	6496.62	23	0.56	7
1469.67	24	0.23	4	2530.25	10	0.51	7	3994.8	8	0.25	7	6526.84	6	5.5	6
1479.73	15	0.263	32	2543.13[d]	10	9.6	9	4040.63	29	0.54	8	6539.66	16	0.99	12
1484.06	19	0.33	5	2558.82	13	1.24	14	4049.68	15	1.17	13	6573.6	4	1.09	19
1486.7[c]	8	0.18	5	2561.36	5	3.6	4	4074.418	20	31.3	29	6600.1	7	0.23	5
1525.39	6	1.13	11	2611.7	4	1.2	3	4114.52	4	8.6	9	6727.5	9	0.07	4
1544.41[d]	10	2.58	24	2689.50	10	2.16	24	4197.69	9	3.0	4	6745.64	16	2.71	30
1562.3	5	0.80	20	2714.50	19	2.8	5	4248.28	21	1.59	18	6792.10	3	24.2	23

TABLE V. *(continued)*

Energy[a] (keV)		Intensity[b]		Energy[a] (keV)		Intensity[b]		Energy[a] (keV)		Intensity[b]		Energy[a] (keV)		Intensity[b]	
6846.37	*32*	0.56	*7*	7708.32	*30*	0.44	*7*	8136.98	*17*	1.40	*16*	9024.95	*17*	0.80	*9*
7218.48	*13*	2.71	*28*	7780.22	*10*	3.8	*5*	8173.8	*9*	0.157	*31*	9206.65	*26*	0.35	*5*
7302.2	*8*	0.28	*5*	7973.45	*25*	0.42	*6*	8184.70	*24*	0.64	*7*	9288.28	*16*	1.10	*12*
7341.67	*6*	36.5	*34*	8036.6	*7*	0.18	*4*	8384.28	*9*	3.43	*33*	9544.83	*28*	0.38	*5*
7499.90	*5*	62	*6*	8051.1	*6*	0.26	*5*	8505.68	*10*	4.7	*5*	9932.1	*6*	0.082	*19*
7536.2	*7*	0.44	*10*	8083.49	*31*	0.47	*7*	8726.78	*24*	0.44	*6*	11415.17	*11*	7.1	*7*
7675.0	*8*	0.16	*4*	8111.99	*9*	6.1	*7*	8804.4	*4*	0.24	*4*				

[a] In our notation, 95.45 *18* is 95.45 ± 0.18 keV, etc. See Section III for a detailed discussion of uncertainties in the energy and intensity values presented in this paper.

[b] γ-ray cross section in mb. Multiply by 0.220 to obtain photons per 100 thermal neutron captures. In our notation, 0.012 *3* is 0.012 ± 0.003, etc.

[c] γ ray not placed on the level scheme.

[d] γ ray placed more than once on the level scheme.

[e] After corrections due to a γ ray of similar energy in the $^{34}S(n,\gamma)$ ^{35}S reaction.

[f] After corrections due to a γ ray of similar energy in the $^{32}S(n,\gamma)^{33}S$ reaction.

A good indication of the soundness and completeness of the $^{34}S(n,\gamma)$ level scheme is provided by the intensity balance for each level listed in Table III. Uncertainties are not explicitly given there, but the net intensity values themselves, given in the last column, provide a clue. We expect, for instance, satisfactory intensity balance for the strongly populated levels at 1572, 2348, 3802, 4189, 4903, and 4963 keV as well as balance between the intensity feeding the ground state and that emerging from the capturing state. In the worst case of the 4963-keV level, this imbalance is only 4 mb (≈13% of its population). Even here, removing ≈2 mb intensity out of 30 mb from the 2023-keV primary transition to this level (see Fig. 3) and ascribing it to a putative 2024.4-keV γ ray deexciting this level to the 2939-keV level would easily remedy the imbalance. This possibility is not precluded (or confirmed) by any previous detailed branching-ratio measurements; these are limited to levels below 4.5 MeV.

Branching-ratio measurements have been reported by van der Mark and ter Veld[23] and by Freeman *et al.*,[24] both from $(d,p\gamma)$ studies. It was noted by Endt and van der Leun[25] that for several levels the agreement between the above two studies was quite poor. The branching ratios determined in our study are given in Table IV. The branching ratios are more accurate than those implied by the absolute intensities listed in Table I because a portion of the 7% minimum uncertainty in the absolute values does not apply. Our branching ratios are in good agreement with values reported earlier for all levels, except the 2717-, 3806-, and 4186-keV levels. For the last two levels, our values agree with those obtained by Freeman *et al.*[24] and conversely disagree with those by van der Mark and ter Veld.[23] Both $(d,p\gamma)$ studies report that the 2717-keV level decays 100% to the ground state, whereas we show three γ rays out of this level (see Fig. 3). Finally, it can be seen either from Fig. 3 or Table IV that the 4903-keV, $1/2^-$ state and the 4963-keV, $3/2^-$ state have strikingly similar branchings.

V. RESULTS: $^{33}S(n,\gamma)^{34}S$

A. γ rays in ^{34}S

The (n,γ) measurements were made with a 1.10-g, 88.2% enriched ^{33}S target. The main interfering constituent (11.0%) was again ^{32}S. The γ-ray spectrum is shown in Fig. 4. This spectrum was 4-5 times more complex, especially in the region 1.7–7.0 MeV, than in the preceding case (see Fig. 2). Approximately 270 γ rays were observed (see Table V). The $^{33}S(n,\gamma)$ reaction with thermal neutrons has not been reported previously by any group, probably because ^{33}S has low natural abundance (0.75%) and a small thermal neutron capture cross section (≈450 mb). The sensitivity of the current experiment was such that ≈15% of the observed γ rays (see Table V) had intensities <0.23 mb (<5 photons per 10^4 captures).

Based on a recent compilation[21] of γ rays from the (n,γ) reaction on all naturally occurring elements and on a study of the (n,γ) Q values[26] for stable and reasonably long-lived target nuclides, the 11415-keV transition (see Fig. 4) appears to be the second highest-energy γ ray ever reported in any (n,γ) reaction with thermal neutrons. The highest-energy γ ray appears to be the 11447-keV transition (6 photons per 100 neutron captures) reported in the $^{10}B(n,\gamma)$ reaction.[27]

B. Known energy levels in ^{34}S

Because the data presaged a complex level scheme, we expended considerable effort in gathering all relevant information on the energy levels in ^{34}S (see Table VI) preparatory to constructing our scheme. Footnote b of Table VI lists 17 primary references to the existing data. Six different $^{31}P(\alpha,p\gamma)$ studies have provided not only accurate level energies and branching ratios for a large number of levels but also spin assignments based

on angular correlation studies. The $^{32}S(t,p)$ reaction has also served to limit the spin choices for a large number of levels. The parity assignments are provided mainly by the angular distributions in the (t,p) and (d,p) reactions. The (d,p) spectroscopic factors extracted by Crozier[28] are employed later in this paper.

TABLE VI. Previously reported levels in ^{34}S.

Level energy[a] (keV)		J^π	Excited in which experiment[b]	Level energy[a] (keV)		J^π	Excited in which experiment[b]
0.0		0^+	β^- decay, β^+ decay, $(\alpha,p\gamma)$, (t,p), (d,p), (p,p′), (p,p′γ), (p,α)	**6950**	*5*	2^-	$(\alpha,p\gamma)$, (t,p), (d,p), (p,p′)
				7112	*5*	(3^-)	$(\alpha,p\gamma)$, (t,p), (d,p), (p,p′)
2127.4	*2*	2^+	β^- decay, β^+ decay, $(\alpha,p\gamma)$, (t,p), (d,p), (p,p′), (p,p′γ), (p,α)	**7220**	*2*	2^+	$(\alpha,p\gamma)$, (γ,γ)
				7248	*2*	2^+	$(\alpha,p\gamma)$, $(\alpha,^2He)$, (t,p), (p,p′)
3303.5	*4*	2^+	β^- decay, β^+ decay, $(\alpha,p\gamma)$, (t,p), (d,p), (p,p′), (p,α)	7264?	*18*		(p,p′)
				7360?	*18*		(p,p′)
3913.9	*7*	0^+	β^- decay, $(\alpha,p\gamma)$, (t,p), (p,p′), (p,α)	7392	*1*	$3^-,5^-$	$(\alpha,p\gamma)$, (t,p), (d,p), (p,p′)
4073.0	*8*	1^+	β^- decay, $(\alpha,p\gamma)$, (t,p), (p,p′), (p,α)	**7476**	*10*		(t,p), (p,p′)
4114.5	*4*	2^+	β^- decay, β^+ decay, $(\alpha,p\gamma)$, (t,p), (d,p), (p,p′), (p,α)	**7547**	*15*		(t,p), (d,p), (p,p′)
				7629	*1*	3^-	$(\alpha,p\gamma)$, (t,p), (d,p), (p,p′)
4622.8	*6*	3^-	β^- decay, $(\alpha,p\gamma)$, $(\alpha,^2He)$, (t,p), (d,p), (p,p′), (p,α)	7655	*9*	$(3,4)^-$	(d,p), (p,p′)
				7714	*16*		(t,p)
4687.9	*4*	4^+	β^- decay, β^+ decay, $(\alpha,p\gamma)$, (t,p), (d,p), (p,p′), (p,α)	**7734**	*9*	2^+	(t,p), (d,p)
				7753	*9*	$(0\text{-}3)^-$	(d,p)
4875.8	*5*	3^+	β^- decay, β^+ decay, $(\alpha,p\gamma)$, (p,p′), (p,α)	**7781**	*2*	1^-	(d,p), (γ,γ)
4890	*2*	2^+	β^- decay, $(\alpha,p\gamma)$, (t,p), (d,p), (p,p′)	7788	*1*	6^-	$(\alpha,p\gamma)$
5227	*10*	0^+	(t,p), (p,p′)	7801	*16*	2^+	(t,p)
5319	*2*	2^-	$(\alpha,p\gamma)$, (t,p), (d,p), (p,p′)	**7971**	*16*		(t,p)
5383	*3*	1^+	$(\alpha,p\gamma)$, (t,p), (d,p), (p,p′)	8025	*16*	0^+	(t,p)
5680	*2*	$2^-,3^-$	$(\alpha,p\gamma)$, (t,p), (d,p), (p,p′)	8083	*1*	5^-	$(\alpha,p\gamma)$
5689	*2*	5^-	$(\alpha,p\gamma)$, $(\alpha,^2He)$, (d,p)	**8142**	*12*	$(0\text{-}3)^-$	(d,p)
5753	*2*	1^-	$(\alpha,p\gamma)$, (t,p), (d,p), (p,p′)	**8185**	*3*	$(1,2^+)$	(γ,γ)
5848	*3*	0^+	$(\alpha,p\gamma)$, (t,p), (p,p′)	8255	*16*	2^+	(t,p)
5993	*3*	2^+	$(\alpha,p\gamma)$, (t,p), (p,p′)	**8293**	*2*	4	$(\alpha,p\gamma)$, (t,p), (d,p)
6120	*2*	2^+	$(\alpha,p\gamma)$, (t,p), (d,p), (p,p′)	8369	*1*	$7^-(5^-)$	$(\alpha,p\gamma)$
6173	*2*	3^-	$(\alpha,p\gamma)$, (t,p), (d,p), (p,p′)	**8385**	*3*	1^-	(t,p), (γ,γ)
6250	*2*	4^+	$(\alpha,p\gamma)$, (t,p), (d,p), (p,p′)	8418	*16*	4^+	(t,p)
6251	*2*	$4^-(3^-)$	(d,p), (t,p), (p,p′)	8450	*70*	6^+	$(\alpha,^2He)$
6347	*3*	1^-	$(\alpha,p\gamma)$, (t,p), (d,p), (p,p′)	8502	*2*	$(4,6^+)$	$(\alpha,p\gamma)$
6415	*2*	4^-	$(\alpha,p\gamma)$, (t,p), (d,p), (p,p′)	**8511**	*3*	1^-	(t,p), (γ,γ)
6480	*5*	1^-	$(\alpha,p\gamma)$, (t,p), (d,p), (p,p′)	**8622**?	*14*		(d,p)
6535	*15*		(t,p)	8657	*7*	$(1,2^+)$	(γ,γ)
6639	*1*	4^-	$(\alpha,p\gamma)$, (t,p), (d,p), (p,p′)	9478	*4*	$(1,2^+)$	(γ,γ)
6688	*6*	$(0\text{-}3)^-$	(t,p), (d,p), (p,p′)	9640	*4*	$(1,2^+)$	(γ,γ)
6731	*2*	$2^+,4^+$	$(\alpha,p\gamma)$, (p,p′)	9711	*5*	$(1,2^+)$	(γ,γ)
6742	*15*	$2^+,4^+$	(t,p), (p,p′)	9860	*7*	$(1,2^+)$	(γ,γ)
6830	*5*	2^+	$(\alpha,p\gamma)$, (t,p), (d,p), (p,p′)	10171	*5*	$(1,2^+)$	(γ,γ)
6864	*1*	$2^+,4^+,5^-$	$(\alpha,p\gamma)$, (t,p), (p,p′)	10700	*99*	6^+	$(\alpha,^2He)$
6890	*1*	$(3,4)^+$	$(\alpha,p\gamma)$, (t,p), (p,p′)	10786	*13*	$(1,2^+)$	(γ,γ)

[a] In our notation 2127.4 *2* is 2127.4 ± 0.2 keV, etc. If a correspondence can be established with a level determined in the present experiment the entry is given in bold type.

[b] Detailed references are as follows: (β^- decay) - D. R. Goosman, C. N. Davids, and D. E. Alburger, Phys. Rev. C **8**, 1324 (1973); (β^+ decay) - R. G. Miller and R. W. Kavanagh, Phys. Lett. **22**, 461 (1966), M. A. van Driel, H. Klijnman, G. A. P. Engelbertink, H. H. Eggenhuisen, and J. A. J. Hermans, Nucl. Phys. **A240**, 98 (1975); $(\alpha,p\gamma)$ - C. E. Moss, R. V. Poore, N. R. Roberson, and D. R. Tilley, Nucl. Phys. **A144**, 577 (1970), M. W. Greene, P. R. Alderson, D. C. Bailey, J. L. Durell, L. L. Green, A. N. James, and J. F. Sharpey-Shafer, Nucl. Phys. **A148**, 351 (1970), P. J. Mulhern, G. D. Jones, I.G. Main, B. T. McCrone, R. D. Symes, M. F. Thomas, and P. J. Twin, Nucl. Phys. **A162**, 259 (1971), G. D. Jones, E. M. Jayasinghe, P. J. Mulhern, I. G. Main, and P. J. Twin, J. Phys. A **5**, 1073 (1972), H.Grawe and R. König, Z. Physik **266**, 41 (1974), H.Grawe and K.Kändler, Proc. Intern. Conf. Nuclear Structure, Tokyo, 1977, edited by T. Marumori (Physical Society of Japan, 1978), p. 217; $(\alpha,^2He)$ - R. Jahn, D. P. Stahel, G. J. Wozniak, R. J. de Meijer, and J. Cerny, Phys. Rev. C **18**, 9 (1978); (t,p) - D. J. Crozier, H. T. Fortune, R. Middleton, and S. Hinds, Phys. Rev. C **17**, 455 (1978); (d,p) - M. W. Brenner, Phys. Rev. **129**, 765 (1963), D. J. Crozier, Nucl. Phys. **A198**, 209 (1972); (γ,γ) - V. E. P. Berg, K. Bangert, G. Junghans, R. Stock, and K. Wienhard, Nucl. Phys. **A306**, 178 (1978); (p,p′) - C. E. Moss, Nucl. Phys. **A121**, 285 (1968); (p,p′γ) - G. J. Bock, E. A. Samworth, J. W. Olness, and E. K. Warburton, Phys. Rev. C **5**, 284 (1972); (p,α) - P. M. Endt, C. H. Paris, A. Sperduto, and W. W. Buechner, Phys. Rev. **103**, 961 (1956). For an independent evaluation of ^{34}S levels, see P. M. Endt and C. van der Leun, Nucl. Phys. **A310**, 1 (1978).

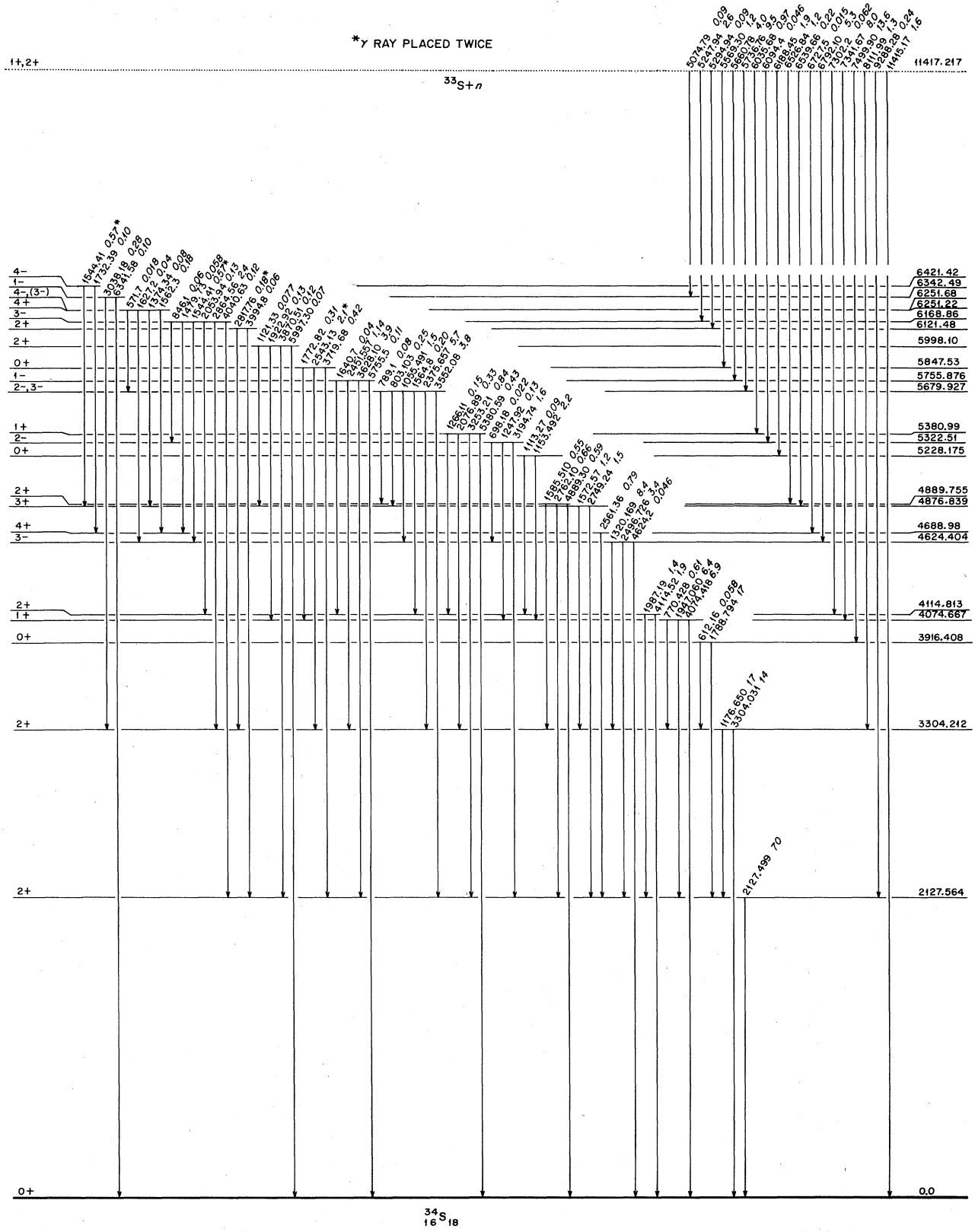

FIG. 5. A partial level scheme for ^{34}S based on the current measurements. All energies are in keV. The complete level scheme is given in Table VII. The italic numbers next to the γ-ray energies refer to absolute intensities per 100 neutron captures. In deducing level energies, nuclear recoil has been taken into account. The uncertainties in level energies are given in Table VII.

C. Level scheme for ^{34}S

Because $J^\pi = 3/2^+$ for the ^{33}S ground state, the capturing state is a 1^+ and 2^+ mixture. Figure 5, which is based on the current data, shows the level scheme up to 6425 keV. These energy levels correspond well with the known levels (see Table VI). The only known level missed is at 5689 keV. This level is expected to be populated only weakly because it has a relatively high J^π value of 5^-. Twenty-three states are shown in Fig. 5, and 19 of these (all except those at 5998, 6251, 6252, and 6421 keV) are directly populated by primary transitions. Twelve of these 19 primary transitions are $M1$, accounting for ≈30% of the total capture cross section; and six are $E1$, accounting for ≈20%. An extremely weak (0.015%) primary $E2$ transition was observed to the 4689-keV, 4^+ level.

TABLE VII. Level scheme of ^{34}S in tabular form.

Level energy[a] (keV)		De-exciting γ rays[b]
0.0		
2127.564	*13*	2127.499
3304.212	*13*	3304.031, 1176.650
3916.408	*21*	1788.794, 612.16
4074.667	*14*	4074.418, 1947.060, 770.428
4114.813	*23*	4114.52, 1987.19
4624.404	*16*	4624.2, 2496.726, 1320.169
4688.98	*5*	2561.36
4876.839	*24*	2749.24, 1572.57
4889.755	*22*	4889.30, 2762.10, 1585.510
5228.175	*23*	1153.492, 1113.27
5322.51	*3*	3194.74, 1247.92, 698.18
5380.99	*4*	5380.59, 3253.21, 2076.89, 1266.11
5679.927	*17*	3552.08, 2375.657, 1564.8, 1055.491, 803.103, 789.1
5755.876	*21*	5755.5, 3628.10, 2451.557, 1640.7
5847.53	*3*	3719.68, 2543.13[c], 1772.82
5998.10	*8*	5997.30, 3870.51, 1922.92, 1121.33
6121.48	*12*	3994.8, 2817.76[c]
6168.86	*3*	4040.63, 2864.56, 2053.94, 1544.41[c], 1479.73, 846.1
6251.22	*19*	1562.3, 1374.34
6251.68	*9*	1627.2, 571.7
6342.49	*10*	6341.58, 3038.18
6421.42	*12*	1732.39, 1544.41[c]
6428.12[d]	*8*	2353.06, 1739.32, 306.63
6478.770	*22*	4350.85, 3174.37, 2404.04, 1854.28, 1602.06, 1156.39, 798.92, 722.95, 631.13
6685.33	*3*	929.436
6828.82	*18*	2753.3
6847.91	*7*	6846.37, 1525.39
6954.22	*3*	4826.0, 3649.88, 2839.3, 1631.641, 1274.30
7110.45	*4*	4982.44, 2995.8, 2233.49, 989.08[c], 941.59, 281.34
7164.46	*17*	5036.4, 3089.53
7219.28	*7*	7218.48, 2530.25, 2328.8
7248.05	*11*	2558.82
7367.42	*10*	5239.8, 3451.5, 2490.6
7467.72	*10*	3392.86, 1469.67, 989.08[c]
7552.69	*8*	4248.28, 2230.14, 1210.04
7629.907	*21*	4325.397, 3515.07, 3005.39, 2940.42
7730.79	*15*	5602.78
7781.22	*6*	7780.22, 1353.46
7974.72	*16*	7973.45, 5847.4, 4670.1
8036.30	*14*	8036.6, 925.79
8138.10	*8*	8136.98, 6010.3, 2290.26, 1795.28[c]
8175.1	*5*	8173.8, 2945.8[c]
8185.46	*13*	8184.70
8205.40	*8*	6077.27, 3581.2
8294.39	*9*	6166.24, 1951.77
8385.40	*6*	8384.28
8506.77	*4*	8505.68, 5202.06, 4391.77, 3183.9
8615.74	*4*	6487.48, 5311.10, 4540.68, 3990.7, 3738.69, 2363.97
8702.35	*13*	6573.6, 3812.0, 3022.0, 2945.8[c], 516.86
8727.63	*8*	8726.78, 6600.1, 3500.3, 1617.00
8805.66	*25*	8804.4, 5501.4, 2326.2[c]
8874.02	*8*	6745.64, 4799.11, 4758.79, 1244.32
9026.31	*6*	9024.95, 3644.8
9158.71	*3*	5084.2, 5043.3, 3311.6
9208.04	*6*	9206.65, 1959.67, 1840.52, 334.21
9546.09	*7*	9544.83, 6241.0, 2326.2[c], 672.00
9598.41	*8*	3476.95, 982.68
9665.74	*4*	7536.2, 2817.76[c]
9801.88	*10*	7675.0, 6496.62, 5884.6
9836.70	*6*	7708.32, 2989.9
9933.35	*13*	9932.1, 2152.41, 1795.28[c], 725.25
10092.21	*15*	3664.8, 1364.4
10179.59	*6*	8051.1, 4499.7
10212.15	*5*	8083.49, 4532.6
10311.53	*3*	6236.3, 4988.6, 2843.7, 2173.55, 1925.94
10650.11	*20*	5268.9[c], 2919.7
10840.62	*15*	6152.1, 748.43
11024.94	*11*	5268.9[c], 4903.4, 1998.3
11417.217	*16*	11415.17, 9288.28, 8111.99, 7499.90, 7341.67, 7302.2, 6792.10, 6727.5, 6539.66, 6526.84, 6188.45, 6094.4, 6035.68, 5736.76, 5660.78, 5569.30, 5294.94, 5247.94, 5074.79, 4938.06, 4731.37, 4588.37, 4568.9, 4462.44, 4306.44, 4252.38, 4197.69, 4049.68, 3949.27, 3864.25, 3787.096, 3635.83, 3442.24, 3278.79, 3241.9, 3231.89, 3211.69, 3122.65, 3031.69, 2910.28, 2801.33, 2714.50, 2689.50, 2611.7, 2543.13[c], 2390.82, 2258.430, 2209.10, 1871.04, 1818.96, 1751.431, 1615.24, 1580.50, 1484.06, 1325.22, 1237.61, 1205.05, 1105.673, 767.20, 576.80, 392.28

[a] In our notation, 2127.564 *13* is 2127.564 ± 0.013 keV, etc. See Section III for a discussion of additional possible systematic uncertainties in the level energies.

[b] See Table V or Fig. 5 for the appropriate intensity values in units of mb or photons per 100 captures, respectively.

[c] γ ray placed more than once on the level scheme.

[d] Levels in the 6.4-11.3 MeV region and the corresponding γ rays are not shown in Fig. 5.

Including secondary γ rays, $\approx$80 transitions, or 30% of the observed total, are shown in Fig. 5. The 11 transitions feeding the ground state account for >95% of the capture cross section. At this juncture, we could have formally abandoned further construction of the level scheme. Nevertheless, spurred on by the quality and quantity of the remaining data and by the extent to which the level scheme has been previously studied to higher energies, we forged ahead and, consequently, have extended the (n,γ) scheme right up to the neutron separation energy. Because of the high density of levels, we have resorted to an alternate form (see Table VII) for presenting these results, thus forgoing our preference for level-scheme figures. The uncertainties in the level energies are also given in Table VII.

We next tackled the energy region of 6.43—8.52 MeV. There are $\approx$39 known levels (see Table VI) in this region. Possible transitions between these levels and those below were checked against the γ-ray data. Possible primary transitions to these levels were similarly checked. The resulting level scheme is shown in Table VII. There are 25 proposed levels in the region 6.43–8.52 MeV. This part of the scheme accounts for an additional $\approx$85 transitions bringing the total to $\approx$165 or $\approx$60% of all observed transitions. Nineteen of these 25 levels correspond reasonably well with the known levels. The six new ones are at 6428, 6848, 7165, 8036, 8175, and 8205 keV.

There still remained $\approx$105 unplaced transitions. Approximately 84 of these were placed either as transitions emerging from levels in the region 8.52 – 11.1 MeV (see Table VII) or as primary transitions to these levels. Because the level scheme below 6 MeV is firmly established, the possible placements of high-energy γ rays (e.g., transitions of energies 9932, 9545, 9207, 9024, 8804, 8727, etc.), which would normally be considered as primary transitions, become quite restrictive. While several proposed levels in the region of 8.52–11.1 MeV are quite certain for this reason, the overall scheme of 21 levels should be viewed with caution,

TABLE VIII. Gamma-ray intensity balance in the $^{33}S(n,\gamma)^{34}S$ reaction.

E(level) (keV)	Intensity in (mb)	Intensity out (mb)	Intensity net (mb)	E(level) (keV)	Intensity in (mb)	Intensity out (mb)	Intensity net (mb)
0	454			7553	1.7	2.5	−0.8
2128	292	318	−26	7630	27	25	2
3304	140	138	2	7731	0.4	1.1	−0.7
3916	63	79	−16	7781	5.4	4.2	1.2
4075	56	63	−7	7975	1.0	0.8	0.2
4115	8	15	−7	8036		0.3	−0.3
4624	45	54	−9	8138	3.3	2.2	1.1
4689	5.1	3.6	1.5	8175	0.3	≈0.3	≈0.0
4877	11	12	−1	8185	1.1	0.6	0.5
4889	5.9	8.2	−2.3	8205	2.4	1.6	0.8
5228	9.3	10.5	−1.2	8294	2.7	2.1	0.6
5323	7.7	8.1	−0.4	8385	4.9	3.4	1.5
5381	5.1	8.0	−2.9	8507	10.0	8.3	1.7
5680	45	52	−7	8616	10.4	9.7	0.7
5756	20	23	−3	8702	2.8	2.0	0.8
5848	7	9	−2	8728	2.5	3.0	−0.5
5998	≈1.8	1.8	≈0	8806	1.2	0.7	0.5
6121	1.6	≈0.8	≈0.8	8874	3.8	3.8	0.0
6169	12	13	−1	9026	1.5	1.2	0.3
6251		1.2	−1.2	9159	3.7	2.4	1.3
6252	2.1	0.3	1.8	9208	1.0	1.8	−0.8
6342	1.2	1.7	−0.5	9546	2.0	1.0	1.0
6421		1.1	−1.1	9598	0.4	0.9	−0.5
6428	0.9	0.8	0.1	9666	1.4	≈0.9	≈−0.5
6479	22	22	0	9802	2.3	1.0	1.3
6685	1.6	1.1	0.5	9837	0.7	0.6	0.1
6829	0.6	0.9	−0.3	9933	0.3	0.4	−0.1
6848	≈0.9	1.7	≈−0.8	10092	0.5	0.8	−0.3
6954	7.9	8.3	−0.4	10180	0.5	0.5	0.0
7110	10	7	3	10212	0.6	0.7	−0.1
7164	1.2	0.8	0.4	10312	1.5	1.8	−0.3
7219	3.0	3.4	−0.4	10650	0.1	≈0.6	≈−0.5
7248	0.9	1.2	−0.3	10840	0.1	0.3	−0.2
7367	1.7	1.6	0.1	11025	0.1	0.4	−0.3
7468	2.1	1.8	0.3	11417		379	

based as the levels are only on energy fits and not on coincidence data or corroboration in another reaction experiment.

Multiple placements of γ rays are inevitable in a complex level scheme. In the current case, we initially placed γ rays in all possible positions in the level scheme warranted by the spin change and agreement—within twice the uncertainty in the γ-ray energy—between the level energy difference and the γ-ray energy. We then either removed or retained multiple placements, depending on the intensity balance considerations for each level. Multiply placed γ rays were excluded in the overall least-squares routine used to determine the best level energies and their uncertainties.

The intensity balance for each of the 70 levels is listed in Table VIII. From the difference between the intensities feeding the ground state and emerging from the capturing state, it is noted that $\approx$75 mb of intensity (17% of the total capture cross section) is contained in numerous unobserved (and fewer unplaced or misplaced) primary transitions. Whenever either the intensity in or intensity out exceeds 10 mb, the intensity balance is satisfactory (<20% imbalance) for all levels, except the 4115-keV, 2^+ state. This agreement is not contrived but emerges naturally from a skeleton level scheme (see later discussion) eschewing the weaker transitions.

Table IX shows branching ratios for strongly populated levels. In most cases, these ratios are better than those currently available from the ^{31}P $(\alpha,p\gamma)$ reaction. A definite but weak (0.4%) $E3$ branch was observed between the 4624-keV, 3^- state and the 0^+ ground state.

VI. RESULTS: ^{32}S$(n,\gamma)^{33}$S

A. γ rays in ^{33}S

Of all the stable S isotopes, ^{32}S is the most abundant (natural abundance—95.02%) and has the largest thermal neutron capture cross section ($\approx$520 mb). A study of the ^{32}S(n,γ) reaction is therefore a *sine qua non* to most studies of thermal capture by S isotopes, and especially to ours because the ^{34}S and ^{33}S targets that we employed both contained significant amounts of ^{32}S. Previous studies of this reaction were of limited utility because they were made long ago with either NaI(Tl) detectors[29,30] or a small (6-cm^3) Ge(Li) detector.[31]

The current measurements were made with a 1.10-g natural S target in which 96.9% of neutron captures take place in ^{32}S. The γ-ray spectrum is shown in Fig. 6. The high-energy part of this spectrum is dominated by the 5420-keV transition (shown crunched by a factor of 4 in the middle part of Fig. 6) and the low-energy part by the 2380- and 841-keV transitions. Approximately 100 γ rays were observed (see Table X), three times the number reported previously.[31] The limit of detection was $\approx$0.05 mb (1 photon per 10^4 captures). The use of a natural S target instead of an enriched ^{32}S

TABLE IX. Gamma-ray branching ratios (in %) of selected ^{34}S levels (E_x in keV).

J_i	E_{x_i}	$J_f\rightarrow$ / $E_{x_f}\rightarrow$	0^+ 0	2^+ 2128	2^+ 3304	0^+ 3916	1^+ 4075	2^+ 4115	3^- 4624	4^+ 4689	3^+ 4877	2^+ 4890	0^+ 5228	2^- 5323
2^+	3304		46 3	54 3										
0^+	3916			99.7 1	0.3 1									
1^+	4075		50 3	46 3	4.4 4	<0.1								
2^+	4115		57 4	43 4	<0.4	<0.2								
3^-	4624		0.4 1	29 3	71 3	<0.2	<0.1							
3^+	4877		<2	55 4	45 4	<0.6	<5	<0.9	<0.2	<0.2				
2^+	4890		32 3	37 3	31 3	<0.6	<0.7	<1.1	<0.3	<0.3				
0^+	5228			<2	<2		96.1 7	3.9 7	<0.4	<0.4	<1.0	<0.3		
2^-	5323		<3	92 2	<1.4	<1.3	7.2 10	<2	1.2 3	<1.4	<0.7	<0.7		
1^+	5381		25 3	48 3	19 2	<1.3	<1.3	8.4 9	<0.7	<0.7	<0.7	<0.7	<0.3	
$2^-,3^-$	5680		<1	33 3	49 3	<0.2	<0.2	1.7 4	13 2	<0.2	2.2 3	0.8 2	<0.1	<0.1
1^-	5756		2.2 4	75 2	22 2	<3	<0.4	0.7 5	<0.4	<0.4	<0.3	<0.3	<0.2	<0.2
0^+	5848			21 3	64 3		15 2	<5	<1.3	<1.7	<0.9	<0.9	<0.6	<0.6
3^-	6169			3.7 6	76 3	<0.8	<0.8	4.1 7	13 3	1.8 3	<0.6	<0.8	<2	2 1
1^-	6479		<0.1	28 3	48 3		4.9 5		5.9 6		2.0 4	<0.5	<1.0	7.2[a] 8
3^-	7630		<1.3		50 3	<0.7		5.7 7	40 3	4.2 6		<0.7	<0.5	<0.5

[a]Additional branches of 1.4% to 5680 keV level and 0.8% to 5756 keV level.

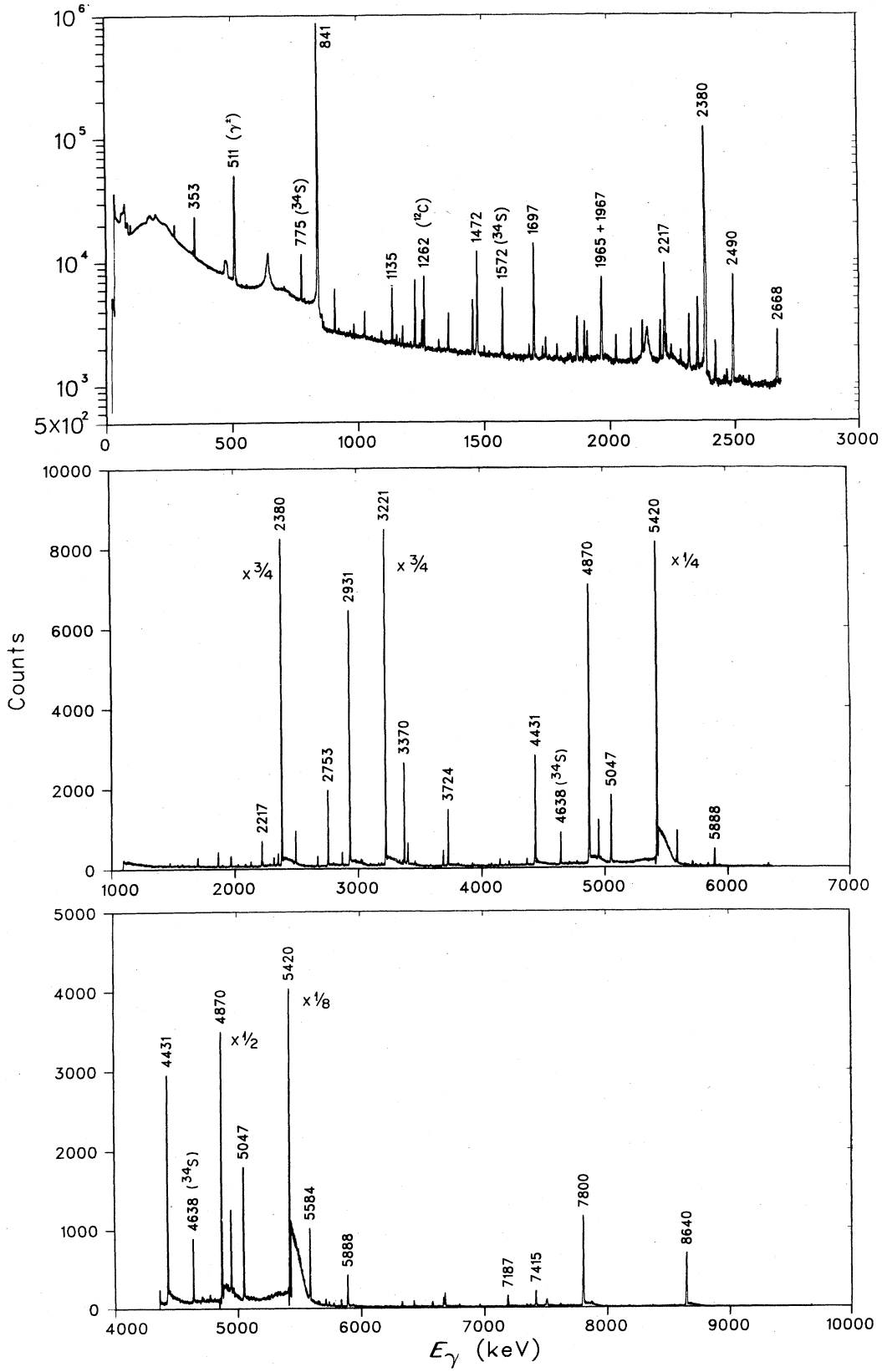

FIG. 6. Gamma-ray spectra from thermal neutron capture by ^{32}S. The Ge(Li) detector was operated either in the Compton-suppression mode (top part) or in the pair-spectrometer mode (middle and bottom parts). All energies are in keV. The peaks with energy labels but without isotope labels arise from the ^{32}S target. A more detailed list of γ rays observed in ^{33}S is given in Table X.

TABLE X. Energies and intensities of γ rays from the $^{32}S(n,\gamma)^{33}S$ reaction.

Energy[a] (keV)		Intensity[b]		Energy[a] (keV)		Intensity[b]		Energy[a] (keV)		Intensity[b]		Energy[a] (keV)		Intensity[b]	
97.90	4	0.092	10	1621.4[e]	3	0.02	1	3093.7[e]	3	0.08	3	5047.14	4	16.2	15
273.559	24	0.34	4	1677.96[c]	10	0.41	6	3161.60	34	0.74	15	5420.58	4	302	27
346.19	14	0.141	27	1697.296	14	13.5	13	3220.59	5	124	12	5479.7	8	0.11	4
353.034	19	1.41	14	1744.06	7	0.99	11	3355.35	34	0.81	18	5583.68	8	7.5	8
707.07	16	0.11	2	1897.48	4	2.11	20	3369.78	6	26.7	26	5648.4	6	0.30	8
840.974	14	345	32	1964.841	31	7.1	7	3397.51	8	5.6	6	5710.40	25	0.91	13
856.44[d]	17	0.19	3	1967.13	6	4.1	5	3455.75	25	0.96	16	5773.8	5	0.36	7
862.55	19	0.11	2	1967.6[e]	3	0.06	3	3582.74	29	0.36	9	5835.61	20	0.82	11
907.315	20	1.42	13	2110.3	4	0.12	4	3723.68	4	13.5	13	5888.09	8	3.8	4
923.48	24	0.117	26	2214.00	8	2.40	29	3809.2	5	0.33	8	6327.79	23	0.64	8
967.91	32	0.104	21	2216.729	18	13.3	12	3831.9	9	0.17	5	6345.8	9	0.084	24
970.0	6	0.06	3	2280.54	15	0.57	10	3920.99	22	0.69	9	6424.72	28	0.56	9
983.20	7	0.28	4	2313.401	23	3.9	4	3934.7	12	0.29	7	6574.93	22	0.60	9
1025.874	31	0.81	8	2379.657	11	230	21	4055.2	5	0.29	8	6664.82	15	1.15	13
1067.1[e]	3	0.03	2	2456.12	24	0.32	5	4076.2	7	0.35	10	6676.13	13	1.58	16
1092.48[d]	15	0.32	5	2465.84	14	0.38	7	4144.36	14	1.41	18	6958.3[d]	5	0.23	5
1135.314	17	2.48	23	2490.221	14	13.5	13	4217.53	21	1.14	15	7187.19	15	1.54	17
1153.40[f]	16	0.20	6	2532.07	28	0.26	4	4363.14	13	1.57	18	7415.31	15	2.25	25
1164.71[d]	23	0.14	4	2667.72	15	3.8	5	4423.5[e]	5	0.90	20	7487.6	9	0.18	4
1209.23	27	0.134	21	2753.26	6	28.7	28	4430.75	5	25.2	23	7505.6	4	0.82	11
1225.744	15	3.4	4	2867.54	8	4.8	5	4444.1	5	0.80	28	7528.2	9	0.10	3
1253.59	4	0.96	10	2930.71	7	87	9	4638.8[g]	8	0.63	14	7614.9	6	0.26	5
1453.900	19	2.83	26	2935.0[e]	6	0.088	19	4708.7	5	0.51	11	7799.77	12	13.7	14
1472.411	13	9.2	9	2973.0	9	0.70	15	4771.1	4	0.73	16	8366.8	6	0.15	3
1500.15	13	0.20	4	3020.35	31	1.05	23	4869.56	4	65	6	8640.45	12	9.2	9
1518.7[e]	20	0.05	2	3029.1	5	0.93	20	4917.7	6	0.56	13				

[a] In our notation, 97.90 *4* is 97.90 ± 0.04 keV, etc. See Section III for a detailed discussion of uncertainties in the energy and intensity values presented in this paper.

[b] γ-ray cross section in mb. Multiply by 0.197 to obtain photons per 100 thermal neutron captures. In our notation 0.092 *10* is 0.092 ± 0.010, etc.

[c] γ ray placed more than once on the level scheme.

[d] γ ray not placed on the level scheme.

[e] Not observed but inferred from the known level branching ratios.

[f] After corrections due to a γ ray of similar energy in the $^{33}S(n,\gamma)^{34}S$ reaction.

[g] Not observed but inferred from the intensity balance requirement and the known branching ratio for the 5480 keV level.

target caused no serious problems, except in the case of the 4638.8-keV transition (see Table X), which was completely obscured (see Fig. 6) by the 4637.9-keV transition due to ^{34}S (see Table I).

B. Known energy levels in ^{33}S

Beginning with the pioneering (d,p) study of Endt and Paris,[32] numerous experiments over the last 25 years have spawned information on ≈126 levels in ^{33}S below 8.4 MeV. Except for this (d,p) study and the (n,γ) study by Kennett, Archer, and Hughes,[31] both of which dealt with levels and their energies, the remaining 14 out of 16 studies referenced under footnote b of Table XI contain some relevant information concerning the J^π values for several of these levels. We have first culled and then consolidated this information under the J^π column of Table XI. We will be especially interested in the (d,p) spectroscopic factors obtained by Mermaz *et al.*[33] for later use.

C. Level scheme for ^{33}S

The ^{33}S level scheme based on the current data (see Fig. 7) was aesthetically the most pleasing of the three schemes that we have constructed. Given a detailed and reliable outline scheme (see Table XI), it was not surprising that the γ rays fell into place readily and almost effortlessly. The current scheme was pleasing because (1) there was no need to invoke new levels, (2) unplaced γ rays constituted only 4 out of 103, (3) primary γ rays were observed to 21 out of 26 levels (the missing ones being $M1$ or $E2$ and hence weak), and (4) the imbalance was at worst only 12% whenever the intensity in or intensity out exceeded 5 mb (see Table XII).

The overall γ-decay pattern, especially the population of low-lying levels as inferred from their deexciting γ rays, is instructive. In the case of ^{33}S, the (n,γ) reaction with thermal neutrons appears to be far more selective than we would have imagined at first. Remembering

TABLE XI. Previously reported levels in ^{33}S.

Level energy[a] (keV)		J^π	Excited in which experiment[b]	Level energy[a] (keV)		J^π	Excited in which experiment[b]
0.0		$3/2^+$	(α,γ), $(\alpha,n\gamma)$, (d,p), $(d,p\gamma)$, (^{3}He,α), (^{3}He,p), (n,γ), (p,d)	6261	*6*		(d,p)
				6310	*6*		(d,p)
840.9	*1*	$1/2^+$	(α,γ), $(\alpha,n\gamma)$, (d,p), $(d,p\gamma)$, (^{3}He,α), (^{3}He,p), (n,γ), (p,d)	6326	*6*		(d,p)
				6362	*3*	$3/2^+$,$5/2^+$	(d,p), (^{3}He,α), (^{3}He,p), (p,d)
1966.3	*1*	$5/2^+$	(α,γ), $(\alpha,n\gamma)$, (d,p), $(d,p\gamma)$, (^{3}He,α), (^{3}He,p), (n,γ), (p,d)	6372	*6*		(d,p)
				6416	*6*		(d,p)
2312.5	*1*	$3/2^+$	(α,γ), $(\alpha,n\gamma)$, (d,p), $(d,p\gamma)$, (^{3}He,α), (^{3}He,p), (n,γ), (p,d)	**6428**	*2*	$1/2^-$,$3/2^-$	(d,p), (n,γ)
				6487	*6*		(d,p)
2866.4	*1*	$5/2^+$	(α,γ), $(\alpha,n\gamma)$, (d,p), $(d,p\gamma)$, (^{3}He,α), (^{3}He,p), (n,γ), (p,d)	6513	*6*		(d,p), (^{3}He,p)
				6526	*6*		(d,p)
2933.7	*1*	$7/2^-$	(α,γ), $(\alpha,n\gamma)$, (d,p), $(d,p\gamma)$, (^{3}He,α), (^{3}He,p), (n,γ), (p,d)	6559	*6*		(d,p)
				6616	*6*		(d,p)
2968.6	*1*	$7/2^+$	(α,γ), $(\alpha,n\gamma)$, (d,p), $(d,p\gamma)$, (^{3}He,α), (^{3}He,p), (p,d)	**6676**	*6*		(d,p), (^{3}He,p)
				6689	*6*	$5/2^-$,$7/2^-$	(d,p)
3219.9	*1*	$3/2^-$	(α,γ), $(\alpha,n\gamma)$, (d,p), $(d,p\gamma)$, (^{3}He,α), (^{3}He,p), (n,γ), (p,d)	6710	*6*		(d,p)
				6720	*6*		(d,p)
3831.6	*2*	$5/2^+$	(α,γ), $(\alpha,n\gamma)$, (d,p), $(d,p\gamma)$, (^{3}He,α), (^{3}He,p), (p,d)	6788	*6*		(d,p)
				6892	*6*		(d,p), (n,γ)
3934.6	*2*	$3/2^+$	(α,γ), $(\alpha,n\gamma)$, (d,p), $(d,p\gamma)$, (^{3}He,α), (^{3}He,p), (p,d)	6905	*3*	$3/2^+$	(d,p), (^{3}He,α), (^{3}He,p), (p,d)
				6967	*3*		(d,p), (^{3}He,p), (p,d)
4047.8	*1*	$9/2^+$	(α,γ), $(\alpha,n\gamma)$, (d,p), $(d,p\gamma)$, (p,d)	6999	*6*		(d,p)
4053.0	*5*	$1/2^+$	$(\alpha,n\gamma)$, (d,p), $(d,p\gamma)$, (^{3}He,p), (n,γ), (p,d)	7017	*6*		(d,p)
				7038	*4*		(d,p), (^{3}He,p), (p,d)
4094.0	*2*	$7/2^+$	$(\alpha,n\gamma)$, (d,p), $(d,p\gamma)$, (p,d)	7133	*6*		(d,p)
4143.7	*3*	$3/2^+$,5/2	$(\alpha,n\gamma)$, (d,p), $(d,p\gamma)$, (^{3}He,p), (p,d)	7164	*6*		(d,p), (^{3}He,p)
4210.4	*2*	$3/2^-$	(α,γ), $(\alpha,n\gamma)$, (d,p), $(d,p\gamma)$, (^{3}He,p), (n,γ), (p,d)	7183	*6*		(d,p)
				7193	*2*	$3/2^-$	(d,p), (n,γ), (p,d)
4374.9	*3*	$1/2^+$	$(\alpha,n\gamma)$, (d,p), $(d,p\gamma)$, (^{3}He,p), (p,d)	7254	*6*		(d,p)
4424.5	*2*	$1/2^+$,3/2	(α,γ), $(\alpha,n\gamma)$, (d,p), $(d,p\gamma)$, (p,d)	7330	*6*		(d,p)
4435	*5*	$7/2^+$	(α,γ), (^{3}He,p)	7337	*4*	$3/2^+$,$5/2^+$	(d,p), (p,d)
4729.4	*1*	$9/2^-$	$(\alpha,n\gamma)$, (d,p), (p,d)	7353	*6*	$5/2^+$	(d,p), (^{3}He,α), (^{3}He,p)
4746	*1*		$(\alpha,n\gamma)$, (d,p), (^{3}He,p), (p,d)	7359	*6*		(d,p)
4865.7	*2*	$11/2^-$	$(\alpha,n\gamma)$, (d,p)	7369	*6*		(d,p)
4919	*2*	$1/2^-$	(α,γ), $(\alpha,n\gamma)$, (d,p), (^{3}He,α), (^{3}He,p), (n,γ)	7401	*6*		(d,p)
				7421	*2*	$1/2^-$,$3/2^-$	(d,p), (n,γ)
4942	*2*	$5/2^-$,$7/2^-$	$(\alpha,n\gamma)$, (d,p), (^{3}He,α), (p,d)	7452	*6*		(d,p), (^{3}He,α)
5177	*3*		(d,p), (^{3}He,α), (p,d)	7460	*6*		(d,p), (^{3}He,p)
5209	*2*		$(\alpha,n\gamma)$, (d,p)	7475	*6*		(d,p)
5273	*2*		(d,p), (p,d)	7482	*6*		(d,p)
5282	*2*		$(\alpha,n\gamma)$, (d,p), (^{3}He,α), (^{3}He,p), (p,d)	**7487**	*6*		(d,p)
5337	*3*	$3/2^+$,$5/2^+$	(d,p), (p,d)	**7503**	*6*		(d,p)
5347	*6*		(d,p)	7560	*6*		(d,p), (^{3}He,p)
5395	*3*		(d,p), (^{3}He,α), (p,d)	7579?	*6*		(d,p)
5475.1	*14*	$1/2^+$	(α,γ), (d,p), (^{3}He,α), (^{3}He,$\alpha\gamma$), (^{3}He,p), (p,d)	7589?	*6*		(d,p)
				7595?	*6*		(d,p)
5597	*6*		(d,p)	7601?	*6*		(d,p)
5616	*3*	$1/2^+$	(d,p), (^{3}He,p), (p,d)	**7615**	*6*		(d,p)
5622	*6*		(d,p), (^{3}He,α)	7629	*6*		(d,p)
5715	*2*	$1/2^-$	(α,γ), (d,p), (^{3}He,α), (^{3}He,p), (n,γ), (p,d)	7658	*6*		(d,p)
				7693	*6*		(d,p)
5726	*2*	$1/2^-$	(α,γ), (p,d)	7711	*6*		(d,p)
5869	*6*		(d,p)	7749	*6*		(d,p)
5894	*2*	$3/2^-$	(d,p), (n,γ)	7766	*6*		(d,p)
5916	*3*	$1/2^+$	(d,p), (^{3}He,p), (p,d)	7779	*6*		(d,p)
5982	*6*		(d,p), (^{3}He,α)	7797	*6*		(d,p)
6067	*6*		(d,p)	7828	*6*		(d,p)
6079?	*6*		(d,p)	7840	*6*		(d,p)
6101	*6*		(d,p)	7862	*6*		(d,p)
6131	*6*		(d,p)	7892	*6*		(d,p)
6234	*6*		(d,p)	7906	*6*		(d,p), (^{3}He,p)

TABLE XI. *(continued)*

Level energy[a] (keV)	J^π	Excited in which experiment[b]	Level energy[a] (keV)	J^π	Excited in which experiment[b]
7983	6	(d,p)	8107	12	(^{3}He,p)
7991	6	(d,p)	8329	12	(^{3}He,p)
8015	6	(d,p), (^{3}He,p)	8334	2	(α,γ)

[a] In our notation 840.9 *1* is 840.9 ± 0.1keV, etc. If a correspondence can be established with a level determined in the present experiment, the entry is given in bold type.

[b] Detailed references are as follows: (α,γ) - O. B. Okon, H. Bakhru, P. Sen, and N. Cue, Z. Phys. A **285**, 207 (1978); ($\alpha,n\gamma$) - M. Toulemonde and N. Schulz, Nucl. Phys. **A181**, 273 (1972), R. G. Hirko and A. D. W. Jones, Nucl. Phys. **A192**, 329 (1972), P. E. Carr, D. C. Bailey, J. L. Durell, L. L. Green, A. N. James, J. F. Sharpey-Schafer, and D. A. Viggars, J. Phys. A **6**, 685 (1973), P. A. Butler, A. J. Brown, P. E. Carr, L. L. Green, A. N. James, C. J. Lister, J. D. MacArthur, P. J. Nolan, and J. F. Sharpey-Schafer, J. Phys. G **1**, 543 (1975), W. A. Sterrenburg, G. van Middelkoop, and F. E. H. van Eijkern, Nucl. Phys. **A275**, 48 (1977); (d,p) - P. M. Endt and C. H. Paris, Phys. Rev. **110**, 89 (1958), M. C. Mermaz, C. A. Whitten, Jr., J. W. Champlin, A. J. Howard, and D. A. Bromley, Phys. Rev. C **4**, 1778 (1971); (d,pγ) - J. R. Southon, A. R. Poletti, and D. J. Beale, Aust. J. Phys. **30**, 23 (1977); (^{3}He,α) - J. Dubois, Nucl. Phys. **A117**, 533 (1968); H. G. Leighton and A. C. Wolff, Nucl. Phys. **A151**, 71 (1970); (^{3}He,$\alpha\gamma$) - J. Dubois, Nucl. Phys. **A117**, 533 (1968); (^{3}He,p) - A. Graue, J. R. Lien, L. Rasmussen, G. E. Sandvik, and E. R. Cosman, Nucl. Phys. **A162**, 593 (1971); (n,γ) - G. van Middelkoop and P. Spilling, Nucl. Phys. **72**, 1 (1965), G. van Middelkoop and H. Gruppelaar, Nucl. Phys. **80**, 321 (1966), T. J. Kennett, N. P. Archer, and L. B. Hughes, Nucl. Phys. **A96**, 658 (1967); (p,d) - A. Moalem and B. H. Wildenthal, Phys. Rev. C **11**, 654 (1975). For an independent evaluation of ^{33}S levels, see P. M. Endt and C. van der Leun, Nucl. Phys. **A310**, 1 (1978).

that the total capture cross section is ≈520 mb, the decay from the $1/2^+$ capturing state apparently bypasses all states with $J \geq 7/2$ (see Table XI) except the 2934-keV, $7/2^-$ state, which has a population of 0.2 mb (see Table XII). Similarly, the decay nearly bypasses all $1/2^+$ states, except, of course, the first-excited $1/2^+$ state at 841 keV. Those at 4053, 4375, 5475, 5616, and 5916 keV (see Table XI) are populated very weakly, if at all; receiving at most 1.1 mb for the 5616-keV level (our energy—5613 keV).

Table XIII shows branching ratios for strongly populated levels. For these levels, the current ratios are generally better than those available from previous measurements.[25]

VII. COMPLETENESS

In Tables I, V, and X, the intensities of γ rays (I_γ) are given in units of mb, but the respective conversion factors to obtain photons per 100 neutron captures are also given in footnote *b* of those tables.

If a level scheme is complete, the quantities ΣI_γ(Primary), $\Sigma E_\gamma I_\gamma / S_n$, and ΣI_γ(Secondary to the ground state) should all be the same within their stated uncertainties. It can be seen from Table XIV that the "completeness" is excellent for ^{32}S, ^{34}S, and ^{36}S. It is reasonable (>80%) even for the ^{33}S$(n,\gamma)^{34}$S reaction, which has a large Q value of 11417 keV and hence a greatly increased probability that many weak transitions go undetected.

Even with thermal neutrons, the ^{32}S$(n,\alpha)^{29}$Si and the ^{33}S$(n,\alpha)^{30}$Si reactions can proceed because of their positive Q values. The former reaction is known to be weak (<10 mb), but the latter reaction has an appreciable cross section of ≈190 mb [Ref. 34]. From the absence of the corresponding γ ray, we estimate that any branching to the 2.235-MeV, first-excited state in ^{30}Si must be <1 mb. The ^{33}S$(n,p)^{33}$P reaction can also proceed, but is known to be very weak (<3 mb) at thermal neutron energies.

The cross sections listed in the last column of Table XIV together with the (n,α) cross sections mentioned in the preceding paragraph imply an absorption cross section of 516 ± 15 mb for natural S. This value is in excellent agreement with 531 ± 15 mb obtained from a recent $MnSO_4$-bath activation measurement.[35] However, our (n,γ) cross section of 294 ± 15 mb for ^{34}S is higher than the cross sections reported from previous activation measurements. The latter values are 260 ± 50 mb (Ref. 36), 270 ± 50 mb (Ref. 37), 238 ± 12 mb (Ref. 38), and 230 ± 3 mb (Ref. 39). Our value is based on the ^{32}S(n,γ) cross section and the target composition (^{34}S/^{32}S = 3.56 ± 0.02) determined by mass spectroscopy. We have no explanation for the discrepancy in the ^{34}S(n,γ) cross section and a remeasurement of this cross section would be of interest.

As expected, the majority of primary transitions are $E1$ in all three schemes. Primary $M1$ transitions account for <1% of the total capture cross section in ^{35}S (S_n = 6986 keV). Based on the currently available J^π assignments (see Table XI), they account for ≈5% of the cross section in ^{33}S (S_n = 8642 keV). It was noted earlier (see Sec. IV C) that primary $M1$ transitions were relatively strong in ^{34}S (S_n = 11417 keV), thus accounting for >30% of the cross section. The intensity carried away by primary $M1$ transitions therefore appears to increase with the neutron separation energy. The solitary examples of primary $E2$ transitions show an opposite trend. The 4269-keV $E2$ transition in ^{35}S (see Fig. 3) is unusually strong (0.34%), the 5774-keV $E2$ transition in ^{33}S (see Fig. 7) is moderately so (0.07%), and the 6728-keV $E2$ transition in ^{34}S (see Fig. 5) is extremely weak (≈0.015%). Having noted these systematic trends, primary $M1$ and $E2$ transitions will not be discussed in

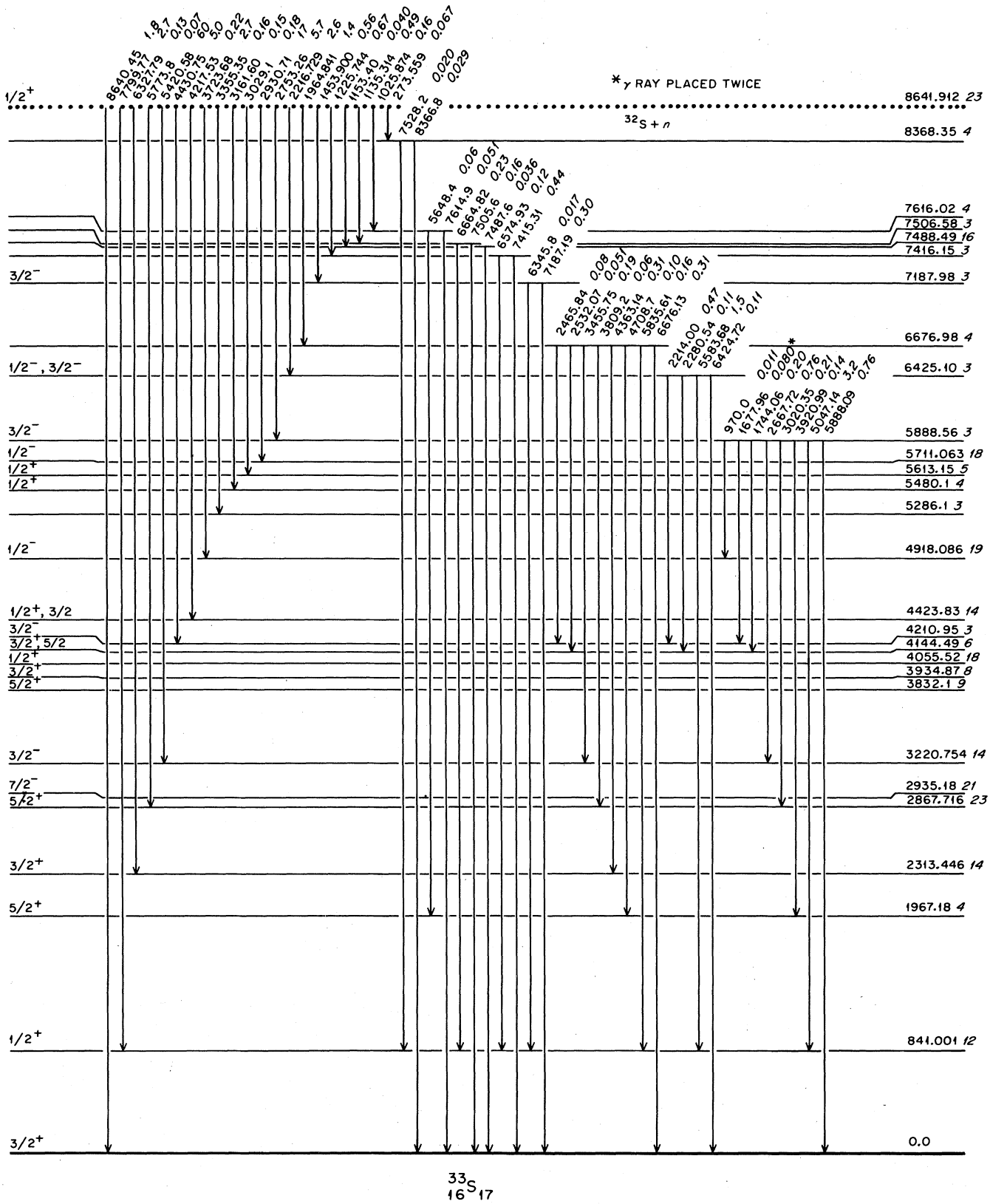

FIG. 7. Level scheme for ^{33}S based on the current data. This part shows the decay modes for levels above 5.8 MeV. See also the caption for Fig. 3.

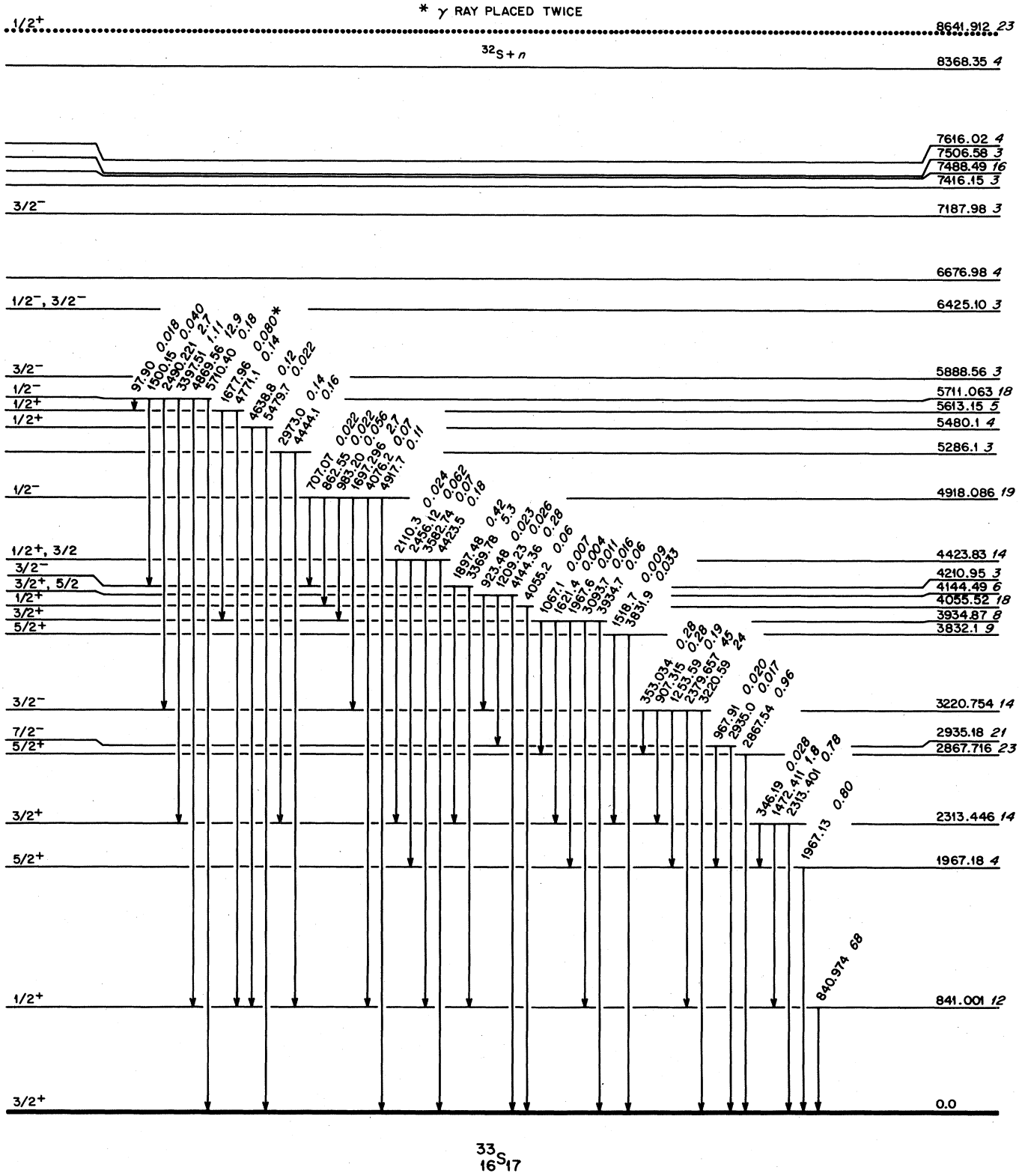

$^{33}_{16}S_{17}$

FIG. 7. (continued). Level scheme for ^{33}S based on the current data. This part shows the decay modes for levels below 5.8 MeV. See also the caption for Fig. 3.

TABLE XII. Gamma-ray intensity balance in the reaction $^{32}S(n,\gamma)^{33}S$.

E(level) (keV)	Intensity in (mb)	Intensity out (mb)	Intensity net (mb)
0	507		
841	374	349	25
1967	3.0	4.1	−1.1
2313	12.3	13.3	−1.0
2868	3.2	4.8	−1.6
2935	0.1	0.2	−0.1
3221	338	357	−19
3832		0.2	−0.2
3935	0.7	0.5	0.2
4056	0.1	0.3	−0.2
4144	1.8	1.7	0.1
4211	29	29	0
4424	1.1	1.7	−0.6
4918	13.5	15.0	−1.5
5286	0.8	1.5	−0.7
5480	0.7	0.7	0.0
5613	1.0	1.1	−0.1
5711	87	86	1
5889	29	27	2
6425	13	11	2
6677	7.1	6.4	0.7
7188	2.8	1.6	1.2
7416	3.4	2.8	0.6
7488	0.2	0.2	0.0
7507	2.5	2.0	0.5
7616	0.8	0.6	0.2
8368	0.3	0.2	0.1
8642		518	

any detail in the remainder of this paper. We will focus attention instead on the $E1$ transitions.

VIII. INTRODUCTION TO THEORY

In the following sections (Sec. IX–XII), we shall describe models for the electric dipole γ-ray emissions following the capture of slow neutrons. These models stem from the central assumption of a neutron changing its state of motion in the potential field of the target nucleus. They have had considerable success in explaining many low-energy neutron capture observations (Refs. 4, 7–13, and 40). Because of the precision and completeness of the current data on the S isotopes, we have recapitulated and extended the formal description of such models with the aim of obtaining accurate numerical estimates for off-resonance capture (Sec. XIII). The formal development is given in terms of $\mathcal{R}$-matrix theory. This approach gives rise to no problems of ambiguity of interpretation provided that the definition of such quantities as the channel radius is properly recognized. Relations between this formalism and the $\mathcal{K}$-matrix and shell-model formalisms have been discussed by Cugnon and Mahaux.[5]

The basic expression that we seek to evaluate is Eq. (3) of Sec. IX. In Sec. X we describe first the origi-

TABLE XIII. Gamma-ray branching ratios (in %) of selected ^{33}S levels (E_x in keV).

J_i	E_{x_i}	$J_f \rightarrow$ / $E_{x_f} \rightarrow$	$3/2^+$ 0	$1/2^+$ 841	$5/2^+$ 1967	$3/2^+$ 2313	$5/2^+$ 2868	$7/2^-$ 2935	$3/2^-$ 3221	$5/2^+$ 3832	$3/2^+$ 3935	$1/2^+$ 4056	$3/2^+,5/2$ 4145	$3/2^-$ 4211
$5/2^+$	1967		≈100	<2										
$3/2^+$	2313		30 2	69 3	1.1 2									
$5/2^+$	2868		≈100	<3	<1	<2								
$3/2^-$	3221		35 2	64 2	0.3 1	0.4 1	0.4 1	<0.1						
$3/2^+,5/2$	4145		85 9					8 1	7 2					
$3/2^-$	4211		<1	93 4	<2	7 1	<1	<1	<1	<1				
$1/2^-$	4918		4 1	2 1	<2	<2	<2	<2	90 4	<1	1.9 3	0.8 2	<0.4	0.8 2
$1/2^-$	5711		1.1 3	76 2	<0.3	7 1	<0.5	<0.5	16 1	<0.3	<0.3	<0.3	<0.3	0.2[a] 1
$3/2^-$	5889		14 1	60 2	2.5 6	<1	4 1	<2	14 2	<2	<2	<2	4 1	<2[b]
$1/2^-,3/2^-$	6425		5 1	68 4	<3	<3	<3	<3	<3	<3	c	<3	5 1	22 2
	6677		25 2	13 2	8 2	24 2	5 2	<3	15 2	<3	<3	<2	4 1	6 1

[a]Additional branch of 0.1% to 5613 keV level.
[b]Additional branch of 0.2% to 4918 keV level.
[c]Obscured by a nearby strong peak.

TABLE XIV. Completeness of sulfur thermal capture measurements.

Target	Number of primary γ rays	Number of secondary γ rays	ΣI_γ Primary (mb)	$\frac{\Sigma E_\gamma I_\gamma}{S_n}$ (mb)	ΣI_γ Secondary to g.s. (mb)	Adopted cross section (mb)
^{32}S	21	82	518 ± 14	517 ± 14	507 ± 14	518 ± 14
^{33}S	61	210	379 ± 20	402 ± 20	454 ± 25	454 ± 25
^{34}S	12	47	282 ± 15	283 ± 15	294 ± 15	294 ± 15
^{36}S	5	10	233 ± 20	233 ± 20	220 ± 23	230[a] ± 20

[a]Based on the subsequent β^- decay of ^{37}S (see Ref. 2).

nal channel capture cross section estimates of Lane and Lynn.[4] These authors recognized that the principal contribution to the matrix element appearing in Eq. (3) below would come from the wave functions in the entrance neutron channel outside the nuclear potential radius. In the extreme off-resonance situation, it is assumed that the internal wave function in the scattering process is negligible (hard-sphere scattering) and the scattering length is equal to the nuclear potential radius. A very simple expression for the capture cross section in terms of the nuclear potential radius and the binding energy of the final (p-wave) single-particle neutron state results; this is hard-sphere capture described in Sec. X A. The adjustments to this expression which are required because of the modification of the scattering length by nearby or distant resonance levels are discussed in Sec. X B; in the generalized channel capture model of this subsection, it is still assumed however that the wave function of the initial state within the nuclear radius can be neglected.

In more realistic developments of this kind of model, it is recognized (1) that the channel contribution to the capture matrix element will be modified by the extension and detailed variation of the neutron-nucleus potential well beyond the effective or conventional nuclear potential radius and (2) that the contribution from the wave function in the internal region will not be completely negligible. As discussed in Sec. XI A, by taking the projection of the internal compound nucleus wave function upon the channel function, an expression for the contribution of the internal wave function to the capture matrix element in the neutron-nucleus potential model can be found. With the internal region thus included, the formal expression for the capture cross section averaged over an energy interval containing many resonances can be shown to be interpretable as a sum of two parts, differing in phase by the factor i, one of which (known as the valency component) is the average over fine-structure resonances, and the other part is a smooth background term (known as the potential capture cross section). In Sec. XI B a similar separation is effected for the formal capture amplitude of a neutron undergoing scattering by a complex potential well (optical model). A formal connection can be made between the scattering properties of the optical model and the average scattering properties (potential scattering length and neutron strength function) of the neutron-nucleus system by equating real and imaginary parts of the reduced $\mathcal{R}$ function of the model and the system. In principle, this procedure allows formal constraints to be placed upon the parameters of the optical model. A similar identification of the potential and average valency capture amplitudes with the real and imaginary capture amplitudes of the optical model can be postulated, and this identification is found to be completely consistent with the identification of scattering properties, provided that the imaginary component of the optical potential is constant in radial form. For other forms the identification of capture amplitudes is only approximate, but the validity of this approximation is demonstrated by numerical calculations (Appendix A). Our overall approach follows the line originally taken by Lane and Lynn[4] in distinction to the more phenomenological approach taken by Ho and Lone[40] in their first paper. These authors identified the average resonance capture with the fluctuating component of the capture amplitude in analogy with the separation made by Feshbach, Porter, and Weisskopf[41] of compound nucleus formation from shape elastic scattering.

The sensitivity of the optical model estimates of the capture cross sections to the detailed form of the optical model is investigated in Sec. XII. There it is found that the differences from the values given by the generalized channel capture expression deduced in Sec. XI are quite modest. We conclude therefore that for practical purposes the generalized channel capture expression can be used for analyzing our sulfur data, provided that the cross sections are multiplied by a model-dependent correction factor. We have computed this factor numerically for a range of optical model parameters. The analysis of the sulfur data according to this prescription is discussed in Sec. XIII.

IX. BASIC EXPRESSIONS FOR THE CAPTURE PROBABILITY

In the perturbation theory applicable for electromagnetic interactions amongst particles, the transition probability for a change of the system from initial state i to final state f is

$$T_{if} = \frac{2\pi}{\hbar} |\langle \Psi_i | \mathcal{H} | \phi_f \rangle|^2 \, d\rho \ , \tag{1}$$

where $\mathcal{H}$ is the electromagnetic perturbation operator and $d\rho$ is the density of photon states with direction vector within the solid-angle element $d\Omega$. The transition probability T becomes the square modulus $|U_{c\gamma}|^2$ of the collision matrix element for the transition $\gamma(i\rightarrow f)$ in capture from the entrance channel c if $\Psi_i = \Psi^{(c)}$, where $\Psi^{(c)}$ is the wave function of the system when there is unit incoming flux in channel c. Likewise, T becomes the cross section $\sigma_{\gamma(i\rightarrow f)}$ if the entrance channel c arises from an incident plane wave of unit flux, whence $\Psi_i = [i\pi^{1/2}(2l+1)^{1/2}/k_c]\Psi^{(c)}$, l being the orbital angular momentum associated with c and k_c the wave number of relative motion in the entrance channel. Hence,

$$\sigma_{\gamma(i\rightarrow f)} = T_{if} = (\pi/k_c^2)(2l+1)|U_{c\gamma(i\rightarrow f)}|^2 . \quad (2)$$

This strictly applies to spinless particles; if intrinsic spin is considered, the factor $(2l+1)$ must be replaced by a quantity that depends on the total angular momentum and channel spin as well as orbital angular momentum (see Sec. X B).

The expansion of the perturbation operator $\mathcal{H}$ into vector spherical harmonics yields the following expression, which is limited to multipolarity $\mathcal{L}\mathcal{M}$ and type T (electric E or magnetic M), for the transition probability integrated over all angles:

$$\sigma_{\gamma(i\rightarrow f)} = T_{if} = \left| \frac{(8\pi)^{1/2}(\mathcal{L}+1)^{1/2}}{(2\mathcal{L}+1)!!\,\mathcal{L}^{1/2}} \times \frac{k_\gamma^{\mathcal{L}+1/2}}{\hbar^{1/2}} \langle \Psi_i | \mathcal{H}_{T\mathcal{M}}{}^{\mathcal{L}} | \Phi_f \rangle \right|^2 , \quad (3)$$

where k_γ is the photon wave number ($k_\gamma = E_\gamma/\hbar c$) and the multipole operator $\mathcal{H}_{T\mathcal{M}}{}^{\mathcal{L}}$ has the form (at the long wavelength limit $k_\gamma r \ll 1$) of

$$\mathcal{H}_{E\mathcal{M}}{}^{(1)} = \sum_k e_k r_k Y_{\mathcal{M}}{}^{(1)}(\theta_k, \phi_k) \quad (4)$$

for electric dipole transitions, and

$$\mathcal{H}_{M\mathcal{M}}{}^{(1)} = \left(\frac{3}{4\pi}\right)^{1/2} \frac{\hbar}{2mc} \sum_k (e_k L_{k,\mathcal{M}} + e_k \mu_k \sigma_{k,\mathcal{M}}) \quad (5)$$

for magnetic dipole transitions. In these expressions, the sums are over all particles k (protons and neutrons) in the radiating nuclear system; e_k are the electric charges of those particles, and r_k, θ_k, ϕ_k their spherical polar coordinates; $Y_{\mathcal{M}}{}^{(\mathcal{L})}$ are the spherical harmonics, m is the nucleon mass, c is the velocity of light, and e is the proton electric charge. The quantities $L_{k,\mathcal{M}}$ and $\sigma_{k,\mathcal{M}}$ are the spherical components of the angular momentum and intrinsic spin vectors of the kth particle, respectively, and μ_k is the intrinsic magnetic moment of the kth particle in units of the nuclear magneton ($e\hbar/2mc$). If the coordinates of a given particle k are expressed in the center of mass frame, the electric dipole operator [Eq. (4)] must be written in terms of the effective charges for protons $\bar{e}_k = e(1 - Z/A)$ and for neutrons $\bar{e}_k = eZ/A$, which replace the e_k of Eq. (4), the sum then running over all nucleons and not just the protons.

X. SLOW NEUTRON CHANNEL CAPTURE

A. Special case of hard-sphere capture

Simple basic formulas for the capture cross section of s-wave neutrons can be obtained from the preceding expressions if the bombarding energy is "off-resonance" and if the final state is a single neutron p-wave state. If the edge of the nuclear force region is assumed to be sharp (this sharp edge will hereafter be called the nuclear potential radius R), the radial wave function of the neutron + target nucleus system (formally called the "projection on the entrance channel") has the form, outside the nuclear potential radius, of

$$u(r) = (2\pi^{1/2}/v^{1/2}k_n)e^{-ik_nR}\sin[k_n(r-R)] , \quad (6)$$

where k_n is the neutron wave number [$k_n = (2mE)^{1/2}/\hbar$], E is the neutron energy in the center of mass frame, m is now the reduced mass of the neutron + nucleus system, and v is the relative velocity. The wave function u is shown schematically in Fig. 8. Although this radial wave function continues within the nucleus, the internal oscillating component of small amplitude can be neglected in this model when computing the radial matrix element required in Eq. (3). Because only the channel region is considered, this model is a specialized version of what is called "channel capture."

The final state, assumed to be a p-wave neutron orbiting in the potential field of the target nucleus, has radial wave function for $r > R$ given by

$$w(r) = N[1 + (\kappa r)^{-1}]e^{-\kappa r} , \quad (7)$$

where the normalization constant N can be evaluated at $r=R$ as $N=w(R)\kappa R(1+\kappa R)^{-1}e^{\kappa R}$, and the reciprocal attenuation length $\kappa = (2m E_f)^{1/2}/\hbar$, E_f being the eigenvalue of the final bound state. The bound state wave function is also shown in Fig. 8.

The resulting expression for the radial factor of the matrix element occurring in Eq. (3) is

$$\int_R^\infty dr\, u(r) r w(r) = \frac{2\pi^{1/2}}{v^{1/2}} \frac{R}{\kappa^2} \left(\frac{3+\kappa R}{1+\kappa R}\right) w(R) e^{ik_nR} . \quad (8)$$

For a square-well potential, the value of the bound state single-particle wave function at the edge of the potential can be taken to be $w^2(R) \approx 2/R$. For s-wave capture of a spinless particle, the angular part of the matrix element $\int d\Omega\, Y_0{}^{(0)*} Y_{\mathcal{M}}{}^{(1)} Y_{-\mathcal{M}}{}^{(1)}$ reduces to $1/2(\pi)^{1/2}$. Here, the spherical harmonics $Y_0{}^{(0)}$ and $Y_{-\mathcal{M}}{}^{(1)}$ are the

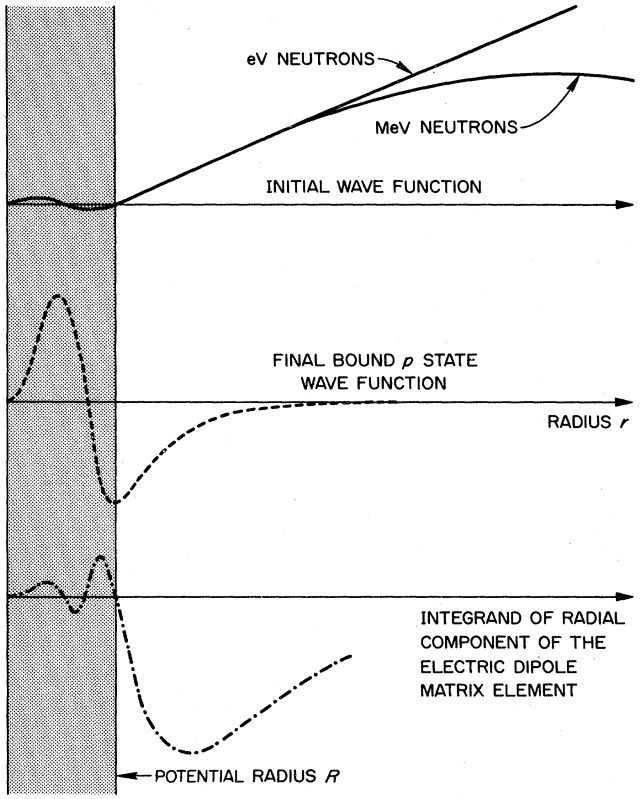

FIG. 8. Schematic diagram of wave functions involved in "off-resonance" neutron capture.

angular components of the initial (s wave) and bound (p wave) wave functions, respectively, while $Y_{\mathcal{M}}^{(1)}$ is the spherical component of the $E1$ operator. Allowing for a weighting factor of 3 for the magnetic substates of the final p-wave state, the so-called hard-sphere capture cross-section expression of Lane and Lynn[4] can be readily obtained:

$$\sigma_{\rm HS} = \frac{\bar{e}^2}{\hbar v}\,\frac{32\pi}{3}\,\frac{R^5 k_\gamma{}^3}{y^4}\left(\frac{y+3}{y+1}\right)^2 , \tag{9}$$

where y denotes κR.

If the single-particle p-wave state is fractionated, Eq. (9) has to be multiplied by the single-particle fractionation factor $\theta_f{}^2$ of the final state f. For neutron capture the neutron spin must be taken into account. The main effect of this is to cause splitting of the single-particle state by spin-orbit coupling, in which case a weighting factor $\mathcal{W}_j$ must be applied to Eq. (9) with a value of 2/3 for the $j = 3/2$ final state and a value of 1/3 for the $j = 1/2$ final state. For slow neutrons (so that $|E_f| \approx E_\gamma$) Eq. (9) reduces numerically to

$$\sigma_{\gamma(i\to f)({\rm HS})} = \sigma_{\rm HS}\,\theta_f{}^2\,\mathcal{W}_j = \frac{0.0614}{R\sqrt{E_{\rm lab}}}\left(\frac{Z}{A}\right)^2 \times\left[\frac{M_t + m_n}{M_t}\right]^3 y^2\left(\frac{y+3}{y+1}\right)^2 \theta_f{}^2\mathcal{W}_j , \tag{10}$$

if R is in units of fm and $E_{\rm lab}$ in eV. The masses of the target nucleus and neutron are denoted by M_t and m_n respectively. It is to be emphasized that Eqs. (8), (9), and (10) are very specialized expessions only to be employed for realistic estimates when the neutron potential scattering length is very close to the nuclear potential radius.

One interesting consequence of Eq. (10) is that, for $y \gg 1$ or $y \ll 1$, the energy variation of the term $[(y+3)/(y+1)]^2$ is negligible; hence, the capture cross section is nearly proportional to the first power of the γ-ray energy rather than to its cube. The latter is the usual crude assumption for the energy behavior of dipole transitions.

B. Generalized channel capture

Because of resonances, the radial wave function in the channel does not, in general, have a node at the nuclear potential radius R as in Eq. (6). In the channel region, which we take as $r > R$ in the ideal case of a sharp-edged nucleus, the wave function has the form

$$\Psi_{\rm ext} = \frac{\pi^{1/2}}{v^{1/2}}\,{\rm i}\sum_l \frac{{\rm i}^l\,(2l+1)^{1/2}}{k_n r}\,[I_l(r) - U_l O_l(r)]\,Y_o{}^l(\theta,\phi) \tag{11}$$

if particle spins are again ignored. In Eq. (11), I_l and O_l denote incoming and outgoing waves, respectively, of orbital momentum l, and U_l is the collision function giving the amplitude of outgoing wave O_l resulting from unit amplitude in the incoming channel l. The collision function can be expressed in $\mathcal{R}$-matrix theory in the form

$$U_l = {\rm e}^{-2{\rm i}\phi_l}\,\frac{1 + {\rm i}P_l\mathcal{R}_l}{1 - {\rm i}P_l\mathcal{R}_l} , \tag{12}$$

where P_l is the centrifugal barrier penetration factor for the elastic neutron channel of orbital angular momentum l, $\mathcal{R}_l$ is the reduced $\mathcal{R}$ function for that channel l, and ϕ_l is its hard-sphere scattering phase factor.

If the discussion is now limited to s-wave neutrons, we can extract the radial wave function in the channel from Ψ_{ext} using

$$\phi_o = P_o = k_n R;\ I_o = e^{-ik_n r};\ \text{and}\ \ O_o = e^{ik_n r} \tag{13}$$

to give

$$u(r) = \frac{i\pi^{1/2}}{v^{1/2}k_n}\left[I_o(r) - e^{-2i\phi_o}O_o(r) - \frac{2iP_o\mathcal{R}_o}{1 - iP_o\mathcal{R}_o}e^{-2i\phi_o}O_o(r)\right]$$
$$= \frac{2\pi^{1/2}e^{-ik_n R}}{v^{1/2}k_n(1 - iP_o\mathcal{R}_o)}\{\sin[k_n(r - R)] + P_o\mathcal{R}_o\cos[k_n(r - R)]\}\ . \tag{14}$$

In the long wavelength approximation, the radial overlap integral is

$$\int_R^\infty dr\, u(r)rw(r) = \frac{2\pi^{1/2}}{v^{1/2}}\frac{e^{-ik_n R}}{(1 - iP_o\mathcal{R}_o)}\frac{R}{\kappa^2}\left[\left(\frac{3 + \kappa R}{1 + \kappa R}\right) + \kappa R\mathcal{R}_o\left(\frac{2 + \kappa R}{1 + \kappa R}\right)\right]w(R)\ , \tag{15}$$

with $w^2(R) \approx 2/R$ for a square-well potential form for the final state.

In this generalized case, the radial overlap integral, being dependent on the details of the resonance levels that enter the $\mathcal{R}$ function, is therefore dependent on J, the total angular momentum of the initial system, which for s-wave neutrons can have the two values $J = I + ½$ or $|I - ½|$, where I is the spin of the target nucleus. Therefore, $\mathcal{R}_l$ should be replaced by $\mathcal{R}_J$. The angular and spin factor of the transition probability, summed over all magnetic substates of the final state (spin J_f) irrespective of photon polarization $\mathcal{M}$ and averaged over all magnetic substates of the initial state is

$$\frac{|\langle J\|\mathbf{Y}_1\|J_f\rangle|^2}{(2J + 1)} = \frac{3}{2\pi}(2J_f + 1)(2j + 1)W^2(½JjJ_f; I1)W^2(0½1j; ½1)(0010|0110)^2\ , \tag{16}$$

where $W(j_1j_2j_4j_5; j_3j_6)$ is the recoupling coefficient of Racah, and j is the spin-orbit coupled angular momentum of the final state, j being coupled in turn to the target spin I to give J_f.

The result, from Eqs. (3), (15), and (16), for the channel capture cross section is

$$\sigma_{\gamma(i\to f)(CH)} = \frac{\bar{e}^2}{\hbar v}\frac{32\pi}{3}\frac{R^5k_\gamma{}^3}{y^4}\sum_{J=|I-½|}^{I+½} g_J\frac{1}{|1 - iP_o\mathcal{R}_J|^2}$$
$$\times\left[\left(\frac{y + 3}{y + 1}\right)^2 + 2y\,\mathrm{Re}\mathcal{R}_J\frac{(y + 3)(y + 2)}{(y + 1)^2} + y^2(\mathrm{Re}\mathcal{R}_J)^2\left(\frac{y + 2}{y + 1}\right)^2 + y^2(\mathrm{Im}\mathcal{R}_J)^2\left(\frac{y + 2}{y + 1}\right)^2\right]\mathcal{W}_{J_f}\theta_f{}^2 \tag{17a}$$
$$= \frac{0.0614}{R\sqrt{E_{lab}}}\left(\frac{Z}{A}\right)^2\left[\frac{M_t + m_n}{M_t}\right]^3\sum g_J\frac{1}{|1 - iP_o\mathcal{R}_J|^2}\left[y^2\left(\frac{y + 3}{y + 1}\right)^2\right.$$
$$\left. + 2\mathrm{Re}\mathcal{R}_J\frac{y^3(y + 3)(y + 2)}{(y + 1)^2} + |\mathcal{R}_J|^2y^4\left(\frac{y + 2}{y + 1}\right)^2\right]\mathcal{W}_{J_f}\theta_f{}^2, \tag{17b}$$

where R is expressed in fm and E in eV, g_J is the spin statistical factor $(2J + 1)/[2(2I + 1)]$, and $\mathcal{W}_{J_f}$ is the spin-coupling factor included in the right hand side of Eq. (16). This factor is given by

$$\mathcal{W}_{J_f} = 2(2J_f + 1)(2j + 1)W^2(½JjJ_f; I1)W^2(0½1j; ½1)(0010|0110)^2. \tag{18}$$

Equation (17b) was given earlier by Lane and Lynn[4] and used by them to explain quantitatively a considerable range of off-resonance thermal neutron capture data available at that time.

Equation (18) depends on J, I, and j as well as on J_f. Table XV shows numerical values for this factor. Of the two quantities $\mathrm{Re}\mathcal{R}_J$ and $\mathrm{Im}\mathcal{R}_J$, the former will normally be the more significant in the off-resonance situation to which Eq. (17) will be applicable. The reduced $\mathcal{R}$ function is

TABLE XV. Value of the spin-dependent factor $\mathcal{W}_{J_f}$ [see Eq. (18)] in the electric dipole matrix element for s-wave neutron capture.

		$I\rightarrow$	0	$^1/_2$	$^1/_2$	$^3/_2$	$^3/_2$	$^5/_2$	$^5/_2$	$^7/_2$	$^7/_2$	$^9/_2$	$^9/_2$
J_f	j	$J\rightarrow$	$^1/_2$	0	1	1	2	2	3	3	4	4	5
$^1/_2$	$^1/_2$		$^1/_3$										
$^3/_2$	$^1/_2$		0										
$^3/_2$	$^3/_2$		$^2/_3$										
0	$^1/_2$			0	$^1/_9$	0							
0	$^3/_2$			0	0	$^1/_9$							
1	$^1/_2$			$^1/_3$	$^2/_9$	$^1/_{18}$	$^1/_6$	0					
1	$^3/_2$			$^2/_3$	$^1/_9$	$^5/_{18}$	$^1/_{30}$	$^1/_5$					
2	$^1/_2$				0	$^5/_{18}$	$^1/_6$	$^2/_{27}$	$^5/_{27}$	0			
2	$^3/_2$				$^5/_9$	$^5/_{18}$	$^1/_6$	$^7/_{27}$	$^{10}/_{189}$	$^5/_{21}$			
3	$^1/_2$						0	$^7/_{27}$	$^4/_{27}$	$^1/_{12}$	$^7/_{36}$	0	
3	$^3/_2$						$^7/_{15}$	$^{28}/_{135}$	$^5/_{27}$	$^1/_4$	$^7/_{108}$	$^7/_{27}$	
4	$^1/_2$								0	$^1/_4$	$^5/_{36}$	$^{12}/_{135}$	$^1/_5$
4	$^3/_2$								$^9/_{21}$	$^5/_{28}$	$^7/_{36}$	$^{11}/_{45}$	$^4/_{55}$
5	$^1/_2$										0	$^{11}/_{45}$	$^2/_{15}$
5	$^3/_2$										$^{11}/_{27}$	$^{22}/_{135}$	$^1/_5$
6	$^1/_2$												0
6	$^3/_2$												$^{13}/_{33}$

$$\mathcal{R}_J = \sum_\lambda \frac{\gamma_{\lambda(n)}{}^2}{E_\lambda - E - (i/2)\,\Gamma_{\lambda(e)}} , \tag{19}$$

the sum being over all levels λ of total angular momentum J with eigenvalue E_λ and total width $\Gamma_\lambda = 2P_o\gamma_{\lambda(n)}{}^2 + \Gamma_{\lambda(e)}$. Here $\gamma_{\lambda(n)}{}^2$ is the reduced width for the neutron channel, and $\Gamma_{\lambda(e)}$ is the width for all other reaction channels.

When $|E_\lambda - E| \gg \Gamma$ for all λ the quantity $\mathrm{Re}\mathcal{R}_J$ is directly related to the scattering length $a_{sc,J}$ at energy E for initial spin state J:

$$a_{sc,J} \approx R\left[1 - \sum \frac{\Gamma_{\lambda(n)}/(2k_nR)}{E_\lambda - E}\right] \approx R(1 - \mathrm{Re}\mathcal{R}_J). \tag{20}$$

At thermal neutron energies, the scattering length can be determined from the total and coherent scattering cross sections,

$$\sigma_{\mathrm{th,total}} = 4\pi \sum_{J=|I-½|}^{I+½} g_J (a_{sc,J})^2 , \tag{21}$$

and

$$\sigma_{\mathrm{th,coh}} = 4\pi \left| \sum_{J=|I-½|}^{I+½} g_J\, a_{sc,J} \right|^2 = 4\pi\, a_{\mathrm{coh}}{}^2 . \tag{22}$$

When $I \neq 0$, there are two possible sets of values for $a_{sc,J}$ determined from Eqs. (21) and (22). This ambiguity cannot be removed. However, if the sign of the coherent scattering length a_{coh} is known, this ambiguity is limited to a twofold nature rather than the fourfold ambiguity if this sign is unknown. When $I = 0$, the value of $a_{sc,J}$ ($\equiv a_{sc,½}$) is unique and is equal to the coherent scattering length.

The development of Eqs. (10) and (17) for the capture cross section has been made on the basis of complete ignorance of the contribution of the internal region (and other channels) to the capture matrix element. Therefore, these equations can be expected to be useful well away from resonances. Estimates of the magnitude of the hard-sphere channel capture to that expected from the internal region have been given by Lane and Lynn.[4]

In a formal sense all previous equations for the channel capture must be generalized by replacing R by the channel radius a_c that demarcates the internal region from the external region of the entrance channel; this radius must be chosen outside the region of nuclear interaction but, formally, needs no other restriction. There are two necessary conditions for the dominance of these channel contributions. As stated already, one is that the reaction is nonresonant. The second is that the channel radius a_c should not be unnecessarily large; if it is larger than is physically reasonable, significant parts of the matrix element will be lost. But what is meant by physically reasonable? The normal convention, as employed above in the derivation of channel capture, is to assume that the nuclear potential well has a very sharp edge and that the usual measure of nuclear potential radius by high-energy nucleon scattering will suffice to define a minimum and usable value for the channel radius. By this convention

$$a_c = R \approx 1.35\,A^{1/3}\ \text{fm} \ . \tag{23}$$

However, the diffuse nature of the surface of the nucleus, as expressed, for example, by the Woods-Saxon potential, will almost certainly imply that there is some nuclear interaction of a complicated type (residual nucleon-nucleon interactions for instance) beyond the radius given in Eq. (23). In any case, because the neutron incoming and outgoing wave functions in the channel that have been employed for the calculation of Eqs. (11) and (13) are based on the assumption that there is not even a smooth nonzero central potential outside the channel radius, these expressions would have to be modified for the choice of a realistic potential beyond the nominal channel radius on these grounds alone. In the next step of the calculation, the wave function in the interior region is discussed with the limitation that only the analytic continuation of the channel wave function into the interior is considered.

XI. POTENTIAL AND VALENCY CAPTURE

A. Capture cross section averaged over resonance levels

The physical idea of a single-particle transition that underlies the channel capture estimates of cross section given above can be formulated to include the internal region. We require expressions that describe the initial state wave function Ψ_i of Eq. (1) in both the internal nuclear and external regions of the configuration space. In the entrance channel ($r > a_c$), the wave function for the external region, in the absence of nuclear spin, is given by Eqs. (11), (12), (14), and (19). With the limitation to s-wave neutrons and the inclusion of particle spins, the external wave function due to an incident plane wave of unit flux of neutrons in magnetic substate μ on nuclei in magnetic substate m is

$$\Psi_{\text{ext},l=0} = \frac{i\pi^{1/2}}{k_n} \sum_{J=|I-1/2|}^{|I+1/2|} (Im\tfrac{1}{2}\mu|I\tfrac{1}{2}JM)(\mathcal{I}_{JM} - U_J\mathcal{O}_{JM}) \ , \tag{24}$$

where the channel incoming and outgoing wave functions are

$$\mathcal{I}_{JM} = I_o Y_o{}^o \psi_{JM}/v^{1/2}r, \text{ and } \mathcal{O}_{JM} = O_o Y_o{}^o \psi_{JM}/v^{1/2}r \ . \tag{25a) and (25b}$$

The channel wave function ψ_{JM} is given by $\sum\sum(Im'\tfrac{1}{2}\mu'|I\tfrac{1}{2}JM)\chi_{Im'}\zeta_{\frac{1}{2}\mu'}$, where the double summation extends over $\mu' = -\tfrac{1}{2}$ to $+\tfrac{1}{2}$ and $m' = -I$ to $+I$. Here, χ_{Im} is the intrinsic wave function, and $\zeta_{\frac{1}{2}\mu}$ is the neutron spin wave function. U_J is the collision function for the nucleon system in a state of total angular momentum J: $U_J = \exp(-2i\phi_o)(1 + iP_o\mathcal{R}_J)/(1-iP_o\mathcal{R}_J)$, this form arising from the matching of the external wave function to the internal wave function described below.

In the reduced $\mathcal{R}$-matrix approach, the corresponding wave function in the internal region is

$$\Psi_{\text{int}} \approx \sum_{J=|I-1/2|}^{I+1/2} (Im\tfrac{1}{2}\mu|I\tfrac{1}{2}JM)\,\frac{\pi^{1/2}\hbar^{1/2}e^{-i\phi_o}}{k_n}\,\frac{2^{1/2}P_o{}^{1/2}\sum_\lambda \gamma_{\lambda(n)}X_{\lambda(JM)}/(E - E_\lambda - \tfrac{1}{2}i\Gamma_{\lambda(e)})}{(1 - iP_o\mathcal{R}_J)} \ , \tag{26}$$

where $X_{\lambda(JM)}$ is the wave function of the $\mathcal{R}$-matrix eigenstate λ; the latter is defined in $\mathcal{R}$-matrix theory as the eigensolution of the Schrödinger equation for the nuclear Hamiltonian in the internal region with suitable real boundary conditions imposed at the channel boundaries.

Using Eqs. (24) and (26), the radiative transition probability [Eq. (1)] and hence the capture cross section [Eq. (2)] for unpolarized neutrons and unpolarized radiation is

$$\sigma_{\gamma(i\to f)} = \frac{8\pi(\mathcal{L}+1)k_\gamma{}^{2\mathcal{L}+1}}{\mathcal{L}[(2\mathcal{L}+1)!!]^2\hbar} \sum_{J=|I-1/2|}^{I+1/2} \frac{1}{2(2I+1)} \sum_{\mu=-1/2}^{1/2} \sum_{m=-I}^{I} (Im\tfrac{1}{2}\mu|I\tfrac{1}{2}JM)^2 \sum_{\mathcal{M}M_f} \left| \frac{\pi^{1/2}\hbar^{1/2}e^{-i\phi_o}}{k_n(1 - iP_o\mathcal{R}_J)} \right.$$

$$\times \sum_\lambda \frac{\Gamma_{\lambda(n)}{}^{1/2}\langle X_{\lambda(JM)}|\mathcal{H}_{T\mathcal{M}}{}^{\mathcal{L}}|\Phi_{f(J_fM_f)}\rangle_{\text{int}}}{E_\lambda - E - \tfrac{1}{2}i\Gamma_{\lambda(e)}} + \frac{\pi^{1/2}e^{-2i\phi_o}}{k_n(1-iP_o\mathcal{R}_J)} 2P_o\mathcal{R}_J\langle\mathcal{O}_{JM}|\mathcal{H}_{T\mathcal{M}}{}^{\mathcal{L}}|\Phi_{f(J_fM_f)}\rangle_{\text{ext}}$$

$$\left. + \frac{i\pi^{1/2}}{k_n}\langle\mathcal{I}_{JM} - e^{-2i\phi_o}\mathcal{O}_{JM}|\mathcal{H}_{T\mathcal{M}}{}^{\mathcal{L}}|\Phi_{f(J_fM_f)}\rangle_{\text{ext}}\right|^2 \ , \tag{27}$$

the subscripts "int" and "ext" indicating that the integration to form the matrix elements is to be confined to the internal or channel regions of configuration space, respectively.

The phase relationships among the various components of the matrix element of Eq. (27) can be brought out more clearly by extracting the factor $\Omega_J = \exp(-i\phi_o)/(1 - iP_o\mathcal{R}_J)$ from every term. With some simple rearrangement and simultaneous extraction of the spin and angular components of the matrix element, we obtain, for electric dipole emission,

$$\sigma_{\gamma(i\to f)} = \frac{\pi}{k_n^2}\frac{16\pi k_\gamma^3}{9}\sum_{J=|I-\frac{1}{2}|}^{I+\frac{1}{2}}\frac{2J+1}{2(2I+1)}\frac{|\langle J\|\mathbf{Y}_1\|J_f\rangle|^2}{2J+1}\times\left|\Omega_J\sum_\lambda\frac{\Gamma_{\lambda(n)}^{\frac{1}{2}}\langle X_\lambda|\bar{e}r|w(r)\rangle_{\text{int}}}{E_\lambda - E - \frac{1}{2}i\,\Gamma_{\lambda(e)}}\right.$$

$$\left. + \Omega_J P_o\mathcal{R}_J\langle(I_o e^{i\phi_o} + O_o e^{-i\phi_o})/(\hbar^{\frac{1}{2}}v^{\frac{1}{2}})|\bar{e}r|w(r)\rangle_{\text{ext}} + i\Omega_J\langle(I_o e^{i\phi_o} - O_o e^{-i\phi_o})/(\hbar^{\frac{1}{2}}v^{\frac{1}{2}})|\bar{e}r|w(r)\rangle_{\text{ext}}\right|^2, \quad (28)$$

the electric dipole operator of Eq. (4) having been approximated to the single-particle form. The terms $(I_o e^{i\phi_o} + O_o e^{-i\phi_o})$ and $i(I_o e^{i\phi_o} - O_o e^{-i\phi_o})$ are real (this is true for general orbital angular momentum l) and, in the case of s waves, are equal to 2 cos $k_n(r - a_c)$ and 2 sin $k_n(r - a_c)$, respectively.

Expression (28) can be evaluated at the complex energy $E + iF$, where $F \gg D_J$, the spacing of levels λ of total angular momentum J, but much smaller than the required averaging interval on the real energy scale, resulting in the following expression for the capture cross section averaged over energy levels λ:

$$\bar{\sigma}_{\gamma(i\to f)} = \frac{\pi}{k_n^2}\frac{16\pi k_\gamma^3}{9}\sum_{J=|I-\frac{1}{2}|}^{I+\frac{1}{2}}\frac{2J+1}{2(2I+1)}\frac{|\langle J\|\mathbf{Y}_1\|J_f\rangle|^2}{2J+1}$$

$$\times\left|\frac{e^{-i\phi_o}}{1 - iP_o\overline{\mathcal{R}}_J}\left\{\int\frac{dE_\lambda}{D_J}\frac{\overline{[\Gamma_{\lambda(n)}^{\frac{1}{2}}(\langle X_\lambda|\bar{e}r|w(r)\rangle_{\text{int}} + \Gamma_{\lambda(n)}^{\frac{1}{2}}\langle\cos k_n(r - a_c)/\hbar^{\frac{1}{2}}v^{\frac{1}{2}}|\bar{e}r|w(r)\rangle_{\text{ext}})]}}{E_\lambda - E - i(\frac{1}{2}\Gamma_{\lambda(e)} + F)}\right.\right.$$

$$\left.\left. + \langle 2\sin k_n(r - a_c)/\hbar^{\frac{1}{2}}v^{\frac{1}{2}}|\bar{e}r|w(r)\rangle_{\text{ext}}\right\}\right|^2\theta_f^2. \quad (29)$$

The quantity $\overline{\mathcal{R}}_J$ is the reduced $\mathcal{R}$ function evaluated at $E + iF$, while the bar over the term in square brackets on the right hand side of Eq. (29) indicates that this term is to be averaged over a large set of local levels λ. This last particular averaging process essentially isolates the radial overlap integral between the final state and the projection of the internal state X_λ upon the channel extrapolated into the internal region. To extract the single-particle aspects of the capture cross section, we use the projection $\langle Y_o{}^o\psi_{JM}|X_{\lambda(JM)}\rangle$, which gives the radial wave function $u_{\lambda(r)}/r$ continued into the internal region. This procedure is formally sufficient to yield a background term [the real part of the projection of the expression within the curly brackets of the right hand side of Eq. (29)] and an average resonance-related term (the imaginary part of the same expression) and can, with appropriate definition of $\mathcal{R}^\infty$, s_o, and $\Gamma_{\gamma(i\to f)(\text{val})}$, lead directly to the cross sections in Eqs. (35) and (38). These cross sections can then be modelled directly by computing an appropriate optical-model wave function and the corresponding electric dipole matrix element, as demonstrated formally by Lane and Mughabghab,[11] and by Cugnon and Mahaux.[5] As pointed out by the latter authors,[5] this procedure, in practice, depends on choosing the correct optical model from the possible set that will satisfy the observed scattering properties. In order to make the physics more apparent we have chosen instead to base the remainder of the development on the intermediate coupling model and its relation to an optical model as outlined originally for a square well by Lane and Lynn.[4] If u_λ is now expanded in terms of radial wave functions of a basis set of single-particle wave functions $U_p(r)$, an expression for the neutron width amplitude can be obtained thus:

$$u_\lambda(r) = \sum_p C_{\lambda(p)}U_p(r);\ \Gamma_{\lambda(n)}^{\frac{1}{2}} = (2P_0)^{\frac{1}{2}}\left(\frac{\hbar^2}{2ma_c}\right)^{\frac{1}{2}}\sum_p C_{\lambda(p)}U_p(a_c), \quad (30)$$

in which the expansion coefficients $C_{\lambda(p)}$ are real quantities.

Hence,

$$\Gamma_{\lambda(n)}{}^{1/2}X_\lambda = (2P_o)^{1/2}\left(\frac{\hbar^2}{2ma_c}\right)^{1/2}\left[\sum_p C_{\lambda(p)}{}^2U_p(a_c)U_p(r) + \sum_p\sum_{p'\neq p} C_{\lambda(p)}C_{\lambda(p')}U_p(a_c)U_{p'}(r)\right]$$

$$+ \text{ other terms proportional to } 1 - \langle Y_0{}^0\psi_{JM}|X_{\lambda(JM)}\rangle \text{ having random signs with respect to } \lambda, \tag{31}$$

and

$$\frac{\Gamma_{\lambda(n)}\cos k_n(r-a_c)}{\hbar^{1/2}v^{1/2}} = (2P_o)\left(\frac{\hbar^2}{2ma_c}\right)\left[\sum_p C_{\lambda(p)}{}^2U_p{}^2(a_c) + \sum_p\sum_{p'\neq p} C_{\lambda(p)}C_{\lambda(p')}U_p(a_c)U_{p'}(a_c)\right]\frac{\cos k_n(r-a_c)}{\hbar^{1/2}v^{1/2}} \quad . \tag{32}$$

In the right hand side of Eqs. (31) and (32), the $p'\neq p$ cross terms are expected to vanish, on averaging, in the normal compound nucleus picture, which would suggest no correlation in the signs of $C_{\lambda(p)}$ and $C_{\lambda(p')}$.

Introduction of Eqs. (31) and (32) into Eq. (29) gives

$$\bar{\sigma}_{\gamma(i\to f)} = \frac{\pi}{k_n{}^2}\frac{4k_\gamma{}^3}{3}\sum_{J=|I-1/2|}^{I+1/2} g_J\mathcal{W}_{J_f}\left|\frac{e^{-i\phi_o}}{1+\pi P_o s_J - iP_o\mathcal{R}_J{}^\infty}\left\{\left(\frac{P_o\hbar^2}{ma_c}\right)^{1/2}\sum_p U_p(a_c)\right.\right.$$

$$\times\int\frac{dE_\lambda}{D_J}C_p{}^2(E_\lambda)\frac{\langle U_p(r)|\bar{e}r|w(r)\rangle_{\text{int}} + U_p(a_c)\langle\cos k_n(r-a_c)|\bar{e}r|w(r)\rangle_{\text{ext}}}{E_\lambda - E - i(\tfrac{1}{2}\Gamma_{\lambda(e)}+F)}$$

$$\left.\left. + \langle 2\sin k_n(r-a_c)/\hbar^{1/2}v^{1/2}|\bar{e}r|w(r)\rangle_{\text{ext}}\right\}\right|^2\theta_f{}^2, \tag{33}$$

where we have represented the overall functional dependence of $\overline{C_{\lambda(p)}{}^2}$ on E_λ by $C_p{}^2(E_\lambda)$, have employed Eqs. (16) and (18), and have substituted the terms for the effects of far-away and local levels in place of the real and imaginary parts of the averaged reduced $\mathcal{R}$ function:

$$\bar{\mathcal{R}}_J = \sum_\lambda\frac{\gamma_{\lambda(n)}{}^2}{E_\lambda - E - i(\tfrac{1}{2}\Gamma_{\lambda(e)}+F)}$$

$$\approx\int\frac{dE_\lambda}{D_J}\frac{\gamma_{\lambda(n)}{}^2(E_\lambda-E)}{(E_\lambda-E)^2+F^2} + iF\int\frac{dE_\lambda}{D_J}\frac{\gamma_{\lambda(n)}{}^2}{(E_\lambda-E)^2+F^2} = \mathcal{R}_J{}^\infty + i\pi s_J \quad , \tag{34a}$$

where s_J is the neutron strength function. In terms of Eq. (30),

$$\mathcal{R}_J{}^\infty = \left(\frac{\hbar^2}{2ma_c}\right)\sum_p U_p{}^2(a_c)\int\frac{dE_\lambda}{D_J}\frac{C_p{}^2(E_\lambda)(E_\lambda-E)}{(E_\lambda-E)^2+F^2}, \tag{34b}$$

and

$$\pi s_J = \left(\frac{\hbar^2}{2ma_c}\right)\sum_p U_p{}^2(a_c)\,F\int\frac{dE_\lambda}{D_J}\frac{C_p{}^2(E_\lambda)}{(E_\lambda-E)^2+F^2} \quad . \tag{34c}$$

The expression for the average capture cross section given in Eq. (33) can be viewed as the sum of two parts: one, which we can term the valency component, being related to the fine-structure resonances,[4] and the other, a smooth non-resonant component. The valency component of the capture cross section is

$$\bar{\sigma}_{\gamma(i\to f)(\text{val})} = \frac{\pi}{k_n{}^2}\sum_{J=|I-1/2|}^{I+1/2} g_J\frac{2\pi P_o s_J}{(1+\pi P_o s_J)^2 + (P_o\mathcal{R}_J{}^\infty)^2}\left(\frac{\pi\Gamma_{\gamma(i\to f)(\text{val})}}{D_J}\right), \tag{35}$$

where the average valency capture width is

$$\Gamma_{\gamma(i\to f)(\mathrm{val})}=\frac{4k_\gamma{}^3\mathcal{W}_{J_f}}{3}D_J\left|\sum_p\overline{C_{\lambda(p)}{}^2}^{\frac{1}{2}}\left\{\langle U_p(r)|\bar{e}r|w(r)\rangle_{\mathrm{int}}+U_p(a_c)\langle\cos k_n(r-a_c)|\bar{e}r|w(r)\rangle_{\mathrm{ext}}\right\}\right|^2\theta_f{}^2\ , \tag{36}$$

with

$$\overline{C_{\lambda(p)}{}^2}=\frac{F}{\pi}\int\frac{\mathrm{d}E_\lambda}{D_J}\frac{C_p{}^2(E_\lambda)}{(E_\lambda-E)^2+F^2}\ . \tag{37}$$

Note that $\bar{\sigma}_{\gamma(i\to f)(\mathrm{val})}$ is not a cross section averaged over resonances in the Hauser-Feshbach sense, but, rather, the average of a resonance-resonance interference term.[4] The valency component arises from the imaginary part of the capture amplitude on the right hand side of Eq. (33) after the factor $\bar{\Omega}_J=\exp(-\mathrm{i}\phi_0)/(1+\pi P_o s_J-\mathrm{i}P_o\mathcal{R}_J{}^\infty)$ is removed.

The real part of the capture amplitude yields the smooth background component of the capture cross section; this component includes channel components of the kind expressed in Eq. (17), with $\mathcal{R}_J$ now limited to $\mathcal{R}_J{}^\infty$, as well as an internal component. Assuming a single principal term in the sum over p,

$$\sigma_{\gamma(i\to f)(\mathrm{back})}=\frac{16\pi k_\gamma{}^3}{3}\frac{1}{\hbar v}\frac{1}{k_n{}^2}\sum_J\frac{g_J\mathcal{W}_{J_f}}{(1+\pi P_o s_J)^2+(P_o\mathcal{R}_J{}^\infty)^2}\Big|P_o\mathcal{R}_J{}^\infty\{\langle U_p(r)/U_p(a_c)|\bar{e}r|w(r)\rangle_{\mathrm{int}}$$

$$+\langle\cos k_n(r-a_c)|\bar{e}r|w(r)\rangle_{\mathrm{ext}}\}+\langle\sin k_n(r-a_c)|\bar{e}r|w(r)\rangle_{\mathrm{ext}}\Big|^2\ , \tag{38}$$

$$=\frac{\bar{e}^2}{\hbar v}\frac{32\pi k_\gamma{}^3}{3}\frac{a_c{}^6w^2(a_c)}{2y^4}\sum_J\frac{g_J\mathcal{W}_{J_f}}{(1+\pi P_o s_J)^2+(P_o\mathcal{R}_J{}^\infty)^2}$$

$$\times\left|\mathcal{R}_J{}^\infty\{\kappa^2\langle U_p(r)/U_p(a_c)|r|w(r)/w(a_c)\rangle_{\mathrm{int}}+y(y+2)/(y+1)\}+(y+3)/(y+1)\right|^2\ , \tag{39}$$

where $y=\kappa a_c$. Because the evaluation of the background component can be modeled with the aid of the optical potential, it is referred to as the potential capture cross section. Equation (39) can be regarded as an extended form of the background channel capture cross section. It includes the contribution from the extension of the channel into the internal region, but excludes the contributions to the wave function from local levels.

B. Optical model capture cross section

The next step in obtaining estimates for the average capture cross section is to model the spreading of the single-particle states into the fine-structure states of the compound nucleus; i.e., to model the behavior of $\overline{C_{\lambda(p)}{}^2}$, $\mathcal{R}_J{}^\infty$, and s_J, and from these the potential scattering length and average compound nucleus formation cross section. This is generally done within the framework of the optical model. Such a procedure was first adopted in Ref. 4 for a square complex potential, and here it is developed for more general forms. The expressions for the capture cross section, scattering properties, and strength function are derived from the optical model $\mathcal{R}$ function (discussed more fully in Appendix A):

$$\mathcal{R}_{\mathrm{opt}}=\left(\frac{\hbar^2}{2ma_c}\right)\sum_q\frac{V_q{}^2(a_c)\mathrm{e}^{-\mathrm{i}\omega_q}}{E_q-E-\mathrm{i}W_q}\ , \tag{40}$$

where the eigenstates are the solutions of the Schrödinger equation for a complex potential well with a boundary condition identical to that imposed at the channel boundary a_c in defining E_λ of Eq. (19) and X_λ of Eq. (26); the radial wave functions of these eigenstates are denoted by $V_q(r)$ and their eigenvalues by $E_q-\mathrm{i}W_q$. The radial wave functions are, in general, complex. The factor $\exp(-\mathrm{i}\omega_q)$ in Eq. (40) is a phase factor allowing the normalization of the complex eigenfunction V_q: $\int V_q{}^2(r)\,\mathrm{d}r=\exp(\mathrm{i}\omega_q)$, where the integral extends from zero to a_c. The phase of $V_q(r)$ is, in fact, arbitrary. We shall choose it in our development below so that $V_q(a_c)$ is real. The real and imaginary parts of $\mathcal{R}_{\mathrm{opt}}$ yield the optical model values of the potential scattering cross section and neutron strength function at low energies:

$$\mathcal{R}_{\text{opt}} = \mathcal{R}_{\text{opt}}^{\infty} + \mathrm{i}\pi s_{\text{opt}} = \left(\frac{\hbar^2}{2ma_c}\right) \sum_q \frac{V_q^2(a_c)[(E_q - E)\cos\omega_q + W_q \sin\omega_q]}{(E_q - E)^2 + W_q^2}$$

$$+ \mathrm{i}\left(\frac{\hbar^2}{2ma_c}\right) \sum_q \frac{V_q^2(a_c)[W_q \cos\omega_q - (E_q - E)\sin\omega_q]}{(E_q - E)^2 + W_q^2} \quad . \tag{41}$$

The optical model internal wave function corresponding to the $\mathcal{R}$ function [Eq. (34)] is [c f. Eq. (26)]

$$\Psi_{\text{int}}^{\text{opt}} = \frac{\pi^{1/2}\hbar^{1/2}}{k_n} \frac{\mathrm{e}^{-\mathrm{i}\phi_{\text{opt}}}}{\sqrt{(1 + \pi P_o s_{\text{opt}})^2 + (P\mathcal{R}_{\text{opt}}^{\infty})^2}} \left(\frac{P_o\hbar^2}{ma_c}\right)^{1/2} \sum_q \frac{V_q(a_c)\mathrm{e}^{-\mathrm{i}\omega_q} V_q(r) Y_o^0}{E_q - E - \mathrm{i}W_q} \quad , \tag{42}$$

where the optical model phase shift is

$$\phi_{\text{opt}} = \phi_o + \arctan\left[P_o\mathcal{R}_{\text{opt}}^{\infty}/(1 + \pi P_o s_{\text{opt}})\right] \quad . \tag{43}$$

The external wave function is

$$\Psi_{\text{ext}}^{\text{opt}} = \frac{\mathrm{i}\pi^{1/2}}{k_n r v^{1/2}} (I_o - U_{\text{opt}} O_o) Y_o^o \quad , \tag{44}$$

where

$$U_{\text{opt}} = \mathrm{e}^{-2\mathrm{i}\phi_o}(1 + \mathrm{i}P_o\mathcal{R}_{\text{opt}})/(1 - \mathrm{i}P_o\mathcal{R}_{\text{opt}}) \quad . \tag{45}$$

Substitution of Eq. (40) into Eqs. (44) and (45) gives

$$\Psi_{\text{ext}}^{\text{opt}} = \frac{\mathrm{i}\pi^{1/2} Y_o^o}{k_n r v^{1/2}} \left\{ \left[\Omega_{\text{opt}}(\mathrm{e}^{\mathrm{i}\phi_o} I_o - \mathrm{e}^{-\mathrm{i}\phi_o} O_o) \right.\right.$$

$$\left. - \mathrm{i}\Omega_{\text{opt}} \left(\frac{P_o\hbar^2}{ma_c}\right) (\mathrm{e}^{\mathrm{i}\phi_o} I_o + \mathrm{e}^{-\mathrm{i}\phi_o} O_o) \sum_q \frac{V_q^2(a_c)(E_q \cos\omega_q - E\cos\omega_q + W_q \sin\omega_q)}{(E_q - E)^2 + W_q^2} \right]$$

$$\left. + \Omega_{\text{opt}} \left(\frac{P_o\hbar^2}{ma_c}\right) (\mathrm{e}^{\mathrm{i}\phi_o} I_o + \mathrm{e}^{-\mathrm{i}\phi_o} O_o) \sum_q \frac{V_q^2(a_c)(W_q \cos\omega_q - E_q \sin\omega_q + E\sin\omega_q)}{(E_q - E)^2 + W_q^2} \right\} , \tag{46}$$

where

$$\Omega_{\text{opt}} = \frac{\mathrm{e}^{-\mathrm{i}\phi_{\text{opt}}}}{\sqrt{(1 + \pi P_o s_{\text{opt}})^2 + (P\mathcal{R}_{\text{opt}}^{\infty})^2}} \quad .$$

Within the curly brackets on the right-hand side of Eq. (46), the term in square brackets has the phase $\exp(-\mathrm{i}\phi_{\text{opt}})$ compared with that of $\mathrm{i}\exp(-\mathrm{i}\phi_{\text{opt}})$ for the remaining term. The internal wave function, Eq. (42), can also be similarly separated into corresponding terms of opposite phase. From these expressions for the wave function, the optical model cross section may be obtained:

$$\sigma_{\gamma(i\to f)(\mathrm{opt})} = \frac{1}{\hbar v}\frac{4k_\gamma^3}{3}\frac{\pi}{k_n^2}\left|\Omega_{\mathrm{opt}}\langle 2\sin[k_n(r-a_c)]|\bar{e}r|w(r)\rangle_{\mathrm{ext}}\right.$$

$$+\Omega_{\mathrm{opt}}\left(\frac{P_o\hbar^2}{ma_c}\right)\sum_q \mathrm{Re}\left[\frac{V_q(a_c)e^{-i\omega_q}\langle V_q(r)|\bar{e}r|w(r)\rangle_{\mathrm{int}} + V_q^2(a_c)e^{-i\omega_q}\langle\cos[k_n(r-a_c)]|\bar{e}r|w(r)\rangle_{\mathrm{ext}}}{E_q - E - iW_q}\right]$$

$$\left.+i\Omega_{\mathrm{opt}}\left(\frac{P_o\hbar^2}{ma_c}\right)\sum_q \mathrm{Im}\left[\frac{V_q(a_c)e^{-i\omega_q}\langle V_q(r)|\bar{e}r|w(r)\rangle_{\mathrm{int}} + V_q^2(a_c)e^{-i\omega_q}\langle\cos[k_n(r-a_c)]|\bar{e}r|w(r)\rangle_{\mathrm{ext}}}{E_q - E - iW_q}\right]\right|^2 \mathcal{W}_j \quad . \quad (47)$$

The applicability of the optical model depends on the identification of $\mathcal{R}_{\mathrm{opt}}$ [Eq. (41)] with $\overline{\mathcal{R}}_J$ [Eq. (34)]. Equating real and imaginary parts, we have

$$\mathcal{R}_J^{\infty} = \left(\frac{\hbar^2}{2ma_c}\right)\sum_p U_p^2(a_c)\int\frac{dE_\lambda}{D_J}\frac{C_p^2(E_\lambda)(E_\lambda - E)}{(E_\lambda - E)^2 + F^2}$$

$$= \mathcal{R}_{\mathrm{opt}}{}^{\infty} = \left(\frac{\hbar^2}{2ma_c}\right)\sum_q \frac{V_q^2(a_c)[(E_q - E)\cos\omega_q + W_q\sin\omega_q]}{(E_q - E)^2 + W_q^2} \quad , \quad (48)$$

$$\pi s_J = \left(\frac{\hbar^2}{2ma_c}\right)\sum_p U_p^2(a_c)\,F\int\frac{dE_\lambda}{D_J}\frac{C_p^2(E_\lambda)}{(E_\lambda - E)^2 + F^2}$$

$$= \pi s_{\mathrm{opt}} = \left(\frac{\hbar^2}{2ma_c}\right)\sum_q \frac{V_q^2(a_c)[W_q\cos\omega_q - (E_q - E)\sin\omega_q]}{(E_q - E)^2 + W_q^2} \quad . \quad (49)$$

For weak or intermediate mixing of the single-particle basis states p [see Eq. (30)] into the compound nucleus motion, Eqs. (48) and (49) suggest the identification of individual terms in the sum over p with corresponding terms in the sum over the optical model states q [See Eq. (40)]. Equations (46) and (47) allow the mixing function $C_p^2(E_\lambda)$ to be represented by the optical model. The most transparent is the Cauchy form,

$$\frac{\overline{C_p^2(E_\lambda)}}{D_J} = \frac{1}{\pi}\frac{G_p}{(E_p - E_\lambda)^2 + G_p^2} \quad , \quad (50)$$

which allows the real R function $\mathcal{R}_J^{\infty}$ and the strength function s_J to be represented (see Appendix A) by an optical model with constant imaginary component $\mathcal{W}(r) = \mathcal{W}_o$ in the potential well from $r = 0$ to the channel radius a_c, giving

$$\mathcal{R}_J{}^{\infty} = \left(\frac{\hbar^2}{2ma_c}\right)\sum_p \frac{U_p^2(a_c)(E_p - E)}{(E_p - E)^2 + G_p^2} = \mathcal{R}_{\mathrm{opt}}{}^{\infty} = \left(\frac{\hbar^2}{2ma_c}\right)\sum_q \frac{V_q^2(a_c)(E_q - E)}{(E_q - E)^2 + \mathcal{W}_o^2} \quad , \quad (51)$$

$$\pi s_J = \left(\frac{\hbar^2}{2ma_c}\right)\sum_p \frac{U_p^2(a_c)G_p}{(E_p - E)^2 + G_p^2} = \pi s_{\mathrm{opt}} = \left(\frac{\hbar^2}{2ma_c}\right)\sum \frac{V_q^2(a_c)\mathcal{W}_o^2}{(E_q - E)^2 + \mathcal{W}_o^2} \quad , \quad (52)$$

and permitting the identifications $E_p = E_q$, $U_p(a_c) = V_q(a_c)$, and $G_p = \mathcal{W}_o = W_q$. In general, for forms that differ from Eq. (50), a suitable optical model will have a radially varying imaginary component in the potential, and these simple identifications will not hold; in particular, $V_q^2(a_c)\exp(-i\omega_q)$ will be complex and hence not equal to $U_p(a_c)$, which is real.

The identification of the scattering properties (real $\mathcal{R}$ function and strength function) of the energy-averaged real scattering problem with the equivalent properties of an optical model suggests the further identification of their capture amplitudes. By equating real and imaginary parts (with respect to Ω_{opt}) of the capture amplitudes of Eqs. (47) and (33), we would require

$$\langle 2\sin[k_n(r-a_c)]|\bar{e}r|w(r)\rangle_{\text{ext}} + \left(\frac{P_o\hbar^2}{ma_c}\right)\sum_p U_p^2(a_c)\left\{\langle U_p(r)/U_p(a_c)|\bar{e}r|w(r)\rangle_{\text{int}} + \langle\cos[k_n(r-a_c)]|\bar{e}r|w(r)\rangle_{\text{ext}}\right\}\text{Re}\int\frac{dE_\lambda}{D_J}\frac{C_p^2(E_\lambda)}{E_\lambda - E - iF} = \langle 2\sin[k_n(r-a_c)]|\bar{e}r|w(r)\rangle_{\text{ext}}$$

$$+\left(\frac{P_o\hbar^2}{ma_c}\right)\sum_q \text{Re}\left\{\frac{V_q^2(a_c)e^{-i\omega_q}[\langle V_q(r)/V_q(a_c)|\bar{e}r|w(r)\rangle_{\text{int}} + \langle\cos[k_n(r-a_c)]|\bar{e}r|w(r)\rangle_{\text{ext}}}{E_q - E - iW_q}\right\}, \quad (53a)$$

and

$$\sum_p U_p^2(a_c)\left\{\langle U_p(r)/U_p(a_c)|\bar{e}r|w(r)\rangle_{\text{int}} + \langle\cos[k_n(r-a_c)]|\bar{e}r|w(r)\rangle_{\text{ext}}\right\}\text{Im}\int\frac{dE_\lambda}{D_J}\frac{C_p^2(E_\lambda)}{E_\lambda - E - iF}$$

$$= \sum_q \text{Im}\left\{\frac{V_q^2(a_c)e^{-i\omega_q}[\langle V_q(r)/V_q(a_c)|\bar{e}r|w(r)\rangle_{\text{int}} + \langle\cos[k_n(r-a_c)]|\bar{e}r|w(r)\rangle_{\text{ext}}}{E_q - E - iW_q}\right\}. \quad (54a)$$

If the radial overlap integral $\{\langle V_q(r)/V_q(a_c)|r|w(r)\rangle_{\text{int}} + \langle\cos k_n(r-a_c)|r|w(r)\rangle_{\text{ext}}\}$ is denoted by $M_q\exp(i\phi_q)$, the right-hand sides of Eqs. (53a) and (54a) can be written as

$$\mathcal{M}_{\text{pot}}^{\text{opt}} = \frac{\bar{e}}{(\hbar v)^{1/2}}\left\{\langle 2\sin k_n(r-a_c)|r|w(r)\rangle_{\text{ext}} + 2P_o\sum_q\frac{\Upsilon_q^2(a_c)M_q[(E_q-E)\cos(\omega_q-\phi_q) + W_q\sin(\omega_q-\phi_q)]}{(E_q-E)^2 + W_q^2}\right\} \quad (53b)$$

and

$$\mathcal{M}_{\text{val}}^{\text{opt}} = \frac{2P_o\bar{e}}{(\hbar v)^{1/2}}\sum_q\frac{\Upsilon_q^2(a_c)M_q[W_q\cos(\omega_q-\phi_q) - (E_q-E)\sin(\omega_q-\phi_q)]}{(E_q-E)^2 + W_q^2}, \quad (54b)$$

respectively. In these equations, the quantity $\Upsilon_q^2 = (\hbar^2/2Ma_c)\,V_q^2(a_c)$ is the $\mathcal{R}$-matrix optical model state reduced width.

For Eqs. (48) and (49) still to hold term by term, there is a general requirement that the quantity $\langle V_q(r)/V_q(a_c)|\bar{e}r|w(r)\rangle_{\text{int}}$ should be real. This will be true for optical potentials with constant imaginary component [corresponding to the Cauchy mixing function, Eq. (48)], but not for general forms. At first sight, this loss of generality would seem to disagree with the results of Lane and Mughabghab[11] that the potential and average resonance components of the capture amplitude can be identified with the respective optical model amplitude of appropriate phase. Instead, this loss really implies that the precise identification of U_p with the optical model $\mathcal{R}$-matrix states will not hold. Thus for optical models with radially varying imaginary components, the real component of the potential will not, in general, be identical with the real well (shell-model potential) that best describes the single-particle states U_p. (The question of the relation between the shell-model potential and the optical-model potential has also been discussed by Cugnon and Mahaux[5] with numerical examples). Nevertheless, for commonly used forms of the optical model, the imaginary part of these matrix elements will generally be small compared to the real part (see Appendix A and its Tables). Hence, we can expect that the real part (after removal of the factor Ω_{opt}) of the capture amplitude of an optical model based on observed shell-model states and neutron scattering properties will be a good approximation to the background component of the cross section extracted from Eq. (33), which we term the potential capture cross section $\sigma_{\gamma,\text{pot}}$. Similarly, the imaginary part will represent the valency term averaged over fine structure resonances [see Eq. (35)]. Thus, the optical model capture cross section of Eq. (47) can be written as

$$\sigma_\gamma^{\text{opt}} = \left|e^{-i\phi_{\text{opt}}}(\sigma_{\gamma,\text{pot}}^{\text{opt}\,1/2} + i\sigma_{\gamma,\text{val}}^{\text{opt}\,1/2})\right|^2, \quad (55a)$$

where

$$\sigma_{\gamma,\mathrm{pot}}^{\mathrm{opt}\ 1/2} = \sqrt{\frac{\pi}{k_n^2}\frac{4k_\gamma^3}{3}}\, e^{i\phi_{\mathrm{opt}}}\,\Omega_{\mathrm{opt}}\,\mathcal{M}_{\mathrm{pot}}^{\mathrm{opt}}\ , \tag{55b}$$

and

$$\sigma_{\gamma,\mathrm{val}}^{\mathrm{opt}\ 1/2} = \sqrt{\frac{\pi}{k_n^2}\frac{4k_\gamma^3}{3}}\, e^{i\phi_{\mathrm{opt}}}\,\Omega_{\mathrm{opt}}\,\mathcal{M}_{\mathrm{val}}^{\mathrm{opt}}\ , \tag{55c}$$

are (approximately) real quantities to be computed numerically from the optical model. Some comparisons of optical model direct calculations with the results of the more exact expressions based on the optical model $\mathcal{R}$-matrix expansion are shown in Table A.III. Such comparisons indicate that the approximations embedded in Eq. (55) are reasonable.

From the term $\sigma_{\gamma,\mathrm{val}}^{\mathrm{opt}}$ of Eq. (55), an expression for the optical model value of the valency component of the capture cross section can be obtained that is completely analogous to Eq. (35):

$$\sigma_{\gamma,\mathrm{val}}^{\mathrm{opt}} = \frac{\pi}{k_n^2}\left|\Omega_{\mathrm{opt}}\right|^2 2\pi P_o s_{\mathrm{opt}}\frac{\pi\Gamma_{\gamma,\mathrm{val}}^{\mathrm{opt}}}{D_J}\ . \tag{56}$$

The precise conditions demanded for this model to be valid will depend on the physical situation. The most stringent condition would be $|\phi_q| \ll |\omega_q|$, but this condition may not always be necessary. For example, if $W_q \ll |E_q - E|$, for all q, the background capture cross section will be approximated by the optical model prescription, provided $|\phi_q| \ll 1$. The closer the imaginary term is to a radially constant volume term, the better the approximation of the optical model to the real well that gives the single-particle states which are at the root of the physical description.

Equation (55) provides the basis for calculating the model-dependent cross sections that we employ for comparison with our experimental data on sulfur isotopes. Optical model calculations to estimate the global behavior of the potential capture cross section have been made previously[4,5] for A $\geq$ 40. A range of detailed optical model calculations of scattering properties and capture cross sections is presented in the next section, with the primary aim of establishing the sensitivity of the capture cross section to the detailed form of the optical potential in the mass number range 30 to 70.

XII. OPTICAL MODEL CALCULATIONS

For low energy s-wave neutron scattering from the lighter nuclei ($A < 100$), the principal data available to determine the most satisfactory optical model are the neutron strength functions given by the resonance parameters. The strength functions are known most accurately for the heavier nuclei (which have higher level densities) in the above mass range. Hence, in the lower range $30 < A < 40$, which comprises the sulfur isotopes studied in this paper, the optical model is essentially, but incompletely, determined from the 3s strength function size resonance. The strength function reaches peak values of $\overline{\Gamma_{\lambda(n)}^{(0)}}/D_J \equiv 2P_0(E = 1\,\mathrm{eV})s_o > 10^{-3}$ at $A \approx 53$. This information will serve only to determine limited features of the optical model, essentially the value of the depth-radius function of the real part of the potential and the magnitude of its imaginary part. Therefore, we adopt for the current work some of the more refined features (such as the surface diffuseness parameter) of the optical model that have been determined from global fits and interpretations of bound single-particle states.

For our calculations, we have employed the Woods-Saxon radial form for the optical scattering potential with the option of a surface-centered imaginary term:

$$\mathcal{U}(r) = \mathcal{V}(r) + i\mathcal{W}(r)\ , \tag{57a}$$

$$\mathcal{V}(r) = \mathcal{V}_0/\{1 + \exp[(r - R)/d]\}\ , \tag{57b}$$

$$\mathcal{W}(r) = \mathcal{W}_v(r) + \mathcal{W}_s(r)\ , \tag{57c}$$

$$\mathcal{W}_v(r) = \mathcal{W}_0/\{1 + \exp[(r - R)/d]\}\ , \tag{57d}$$

$$\mathcal{W}_s(r) = \mathcal{Z}_0 \exp[-(r - R)^2/b^2]\ . \tag{57e}$$

Some information about the computer program used for our calculations is given in Appendix B. We have chosen[42] $\mathcal{V}_0 = -42.8$ MeV for the real central depth and $d = 0.69$ fm for the diffuseness parameter. With this value of $\mathcal{V}_0$, the relationship $R = (1.16\,A^{1/3} + 0.6)$ fm centers the 3s strength function peak at $A = 55$ and the 2s peak at $A = 8$ or 9 for zero neutron energy. These peaks agree approximately with the strength function data.[43]

We have also employed three choices of the imaginary term that successfully yield approximate fits to the strength function data. The choices are:

(i) a volume form $\mathcal{W}_v(r)$ with imaginary central depth $\mathcal{W}_0 = -2.5$ MeV,

(ii) a moderately-spread surface form $\mathcal{W}_s(r)$ with width parameter $b = 0.665$ fm, and peak magnitude $\mathcal{Z}_0 = -11$ MeV, and

(iii) a narrowly-spread surface from $\mathcal{W}_s(r)$ with $b = 0.332$ fm and $\mathcal{Z}_0 = -29.2$ MeV.

For these choices, the strength function $\overline{\Gamma_{\lambda(n)}^{(0)}}/D_J$, the potential scattering parameter a_{pot}, and $\mathcal{R}_{\mathrm{eff}}^{\infty}$ (the value of the real $\mathcal{R}$ function for effective channel radius $a_c = R$) are shown in Figs. 9 and 10. It is clear from these figures that a proper choice of the imaginary term for analyzing our sulfur results depends in a sensitive manner on only the strength function data below the 3s-size resonance; the experimental data in this region are poor.

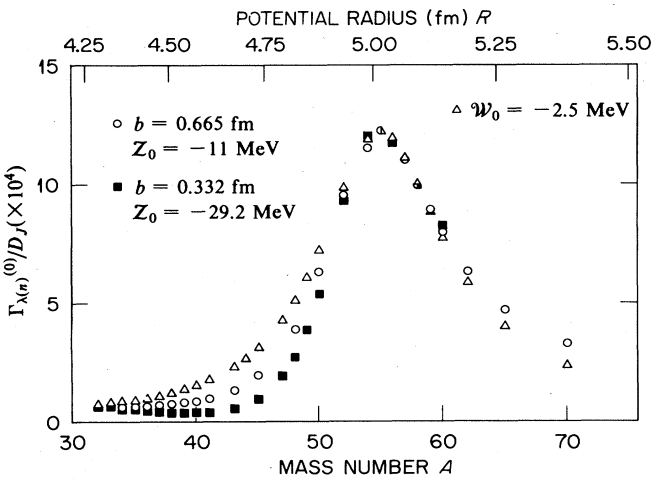

FIG. 9. Calculated s-wave neutron strength function from the volume absorption model (triangles) and from the surface absorption model (circles and squares).

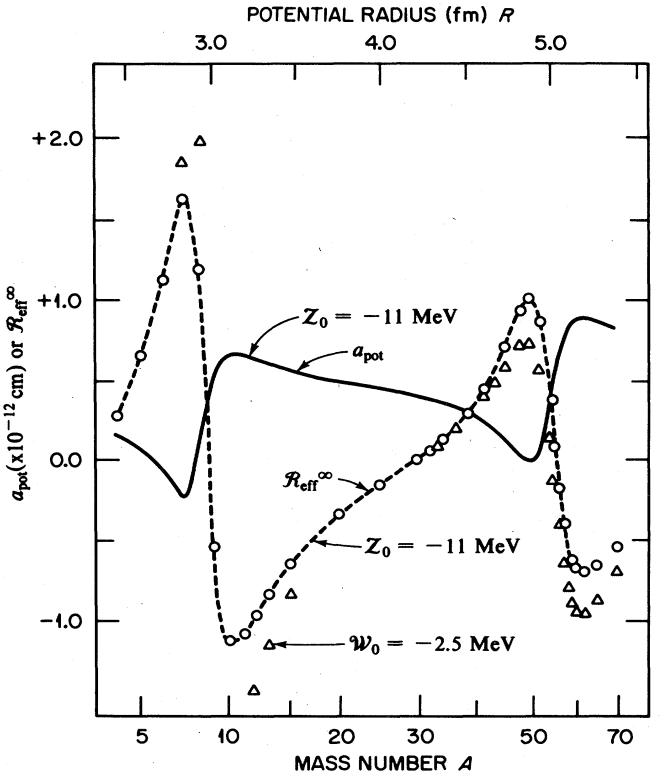

FIG. 10. The potential scattering length for the surface absorption model (solid curve) and the corresponding value of the real part of the effective reduced $\mathcal{R}$ function (dashed curve). The latter was calculated with the assumption that the channel radius a_c is equal to the nuclear potential radius R. The triangles are for the volume absorption model.

We have, therefore, employed all three versions of the optical potential to calculate the capture cross section of primary γ rays to the $p_{1/2}$ and $p_{3/2}$ single-particle states. These states were calculated in a real potential of identical form and parameters as that of the optical potential except for the addition of a spin-orbit term:

$$\mathcal{V}_{so}(r,k,j_k) = (\mathbf{k}\cdot\sigma_{\mathbf{k}})K_s\mathcal{V}_o \times \exp[(r-R)/d]/rd\{1+\exp[(r-R)/d]\}^2 , \quad (58)$$

where k is the orbital angular momentum and j_k is the spin formed by coupling k to the neutron spin. The parameters employed are $K_s = 0.00435$; $\mathbf{k}\cdot\sigma_{\mathbf{k}} = 1$ for $k = 1$, $j_k = 3/2$; and $\mathbf{k}\cdot\sigma_{\mathbf{k}} = -2$ for $k = 1$, $j_k = 1/2$. The calculated p-wave eigenvalues are shown in Fig. 11.

Calculated capture cross sections are shown in Figs. 12–16. The valency capture cross section [the squared imaginary part of $\Omega_{\text{opt}}{}^{-1}$ ($\sigma_{\gamma(i\to f)(\text{opt})})^{1/2}$—see Eq. (47)] is not presented as such, but rather the quantity $\Gamma_{\gamma,\text{val}}^{\text{opt}}/D_J E_\gamma{}^3$ that has been extracted from it [see Eq. (56)]. This, in turn, is reduced to an effective charge $Ze/A = e/2$ and divided by the neutron strength function $\overline{\Gamma_{\lambda(n)}{}^{(0)}}/D_J$, which governs the content of the single-particle state in the initial compound nucleus wave function. The resulting expression for the optical model radiation strength function is

$$s_{\gamma,\text{val}}^{\text{opt}} = \frac{10^{-4}}{E_\gamma{}^3(\text{in MeV})}\left(\frac{\overline{\Gamma_{\lambda(n)}{}^{(0)}}}{D_J}\right)^{-1}\left(\frac{A}{2Z}\right)^2\frac{\Gamma_{\gamma,\text{val}}^{\text{opt}}}{D_J} . \quad (59)$$

The results are shown in Fig. 12 as a function of the binding energies of the $1p_{1/2}$ and $2p_{1/2}$ final states. The smooth monotonic form indicates that there is no residual sensitivity to the neutron strength function. The

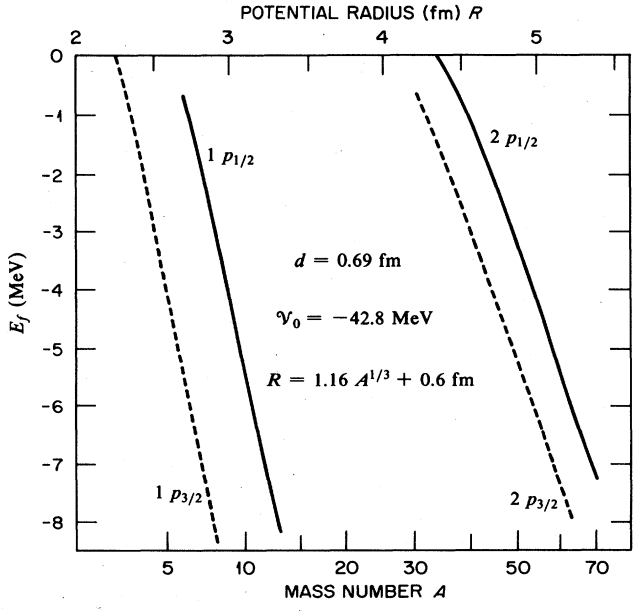

FIG. 11. Eigenvalues of p-wave single-particle neutron states calculated for the real part of a Woods-Saxon potential.

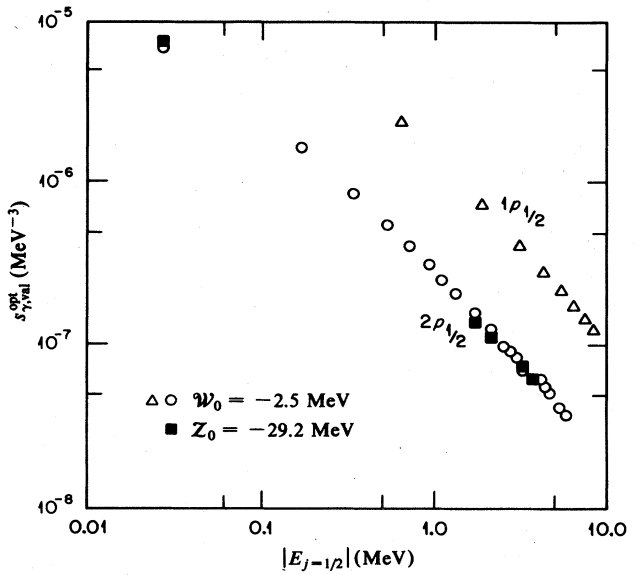

FIG. 12. Reduced valency strength [see Eq. (59)] plotted as a function of the binding energy of the $p_{1/2}$ state for the volume absorption model (circles and triangles) and the surface absorption model (squares).

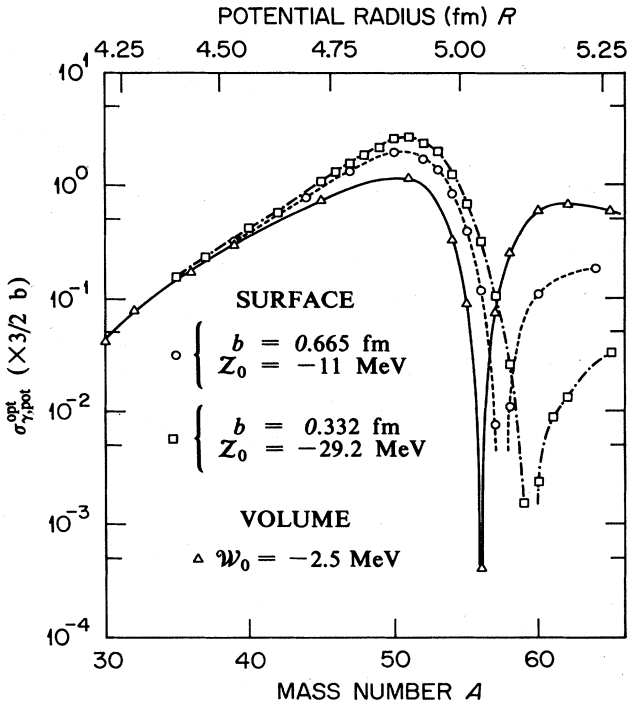

FIG. 13. Potential capture cross section [see Eq. (55b)] as a function of mass number for three versions of the optical model.

strong fall on the logarithmic plot indicates the major influence of the contribution of the channel region (which depends, in turn, on the p-wave tail) to the radial overlap integral for the transition. The valency radiation width is proportional to the square of the γ-ray energy rather than to its cube. The latter is expected from basic statistical models. The virtual indistinguishability (see the lower curve of Fig. 12) of the calculations based on the surface absorption model from those of the volume absorption model seems to indicate the general reliability of the method as a means of computing the valency radiation width. The results for the $p_{3/2}$ states were qualitatively similar but are not shown here.

Of more importance for our immediate purposes are the results on the background (direct) or potential capture cross section $\sigma_{\gamma,\mathrm{pot}}$. Results for the three models are shown in Fig. 13 as a function of the mass number. For this quantity, there is clearly strong model sensitivity for $A > 44$. This model sensitivity is certainly associated with the behavior of the potential scattering length (c f. Fig. 10). Therefore, in Fig. 14 we plot the potential capture cross section as a function of $\mathcal{R}_{\mathrm{eff}}^{\infty}$. This figure shows a very strong dependence of background capture on $\mathcal{R}_{\mathrm{eff}}^{\infty}$, which leaves little further dependence on the details of the form of absorption in the optical potential, except when the potential capture cross section is very small, in which case strong cancellation occurs in the contribution of the matrix element from the region $r > R$. In fact, comparison of the results of these optical model calculations with the channel capture expression

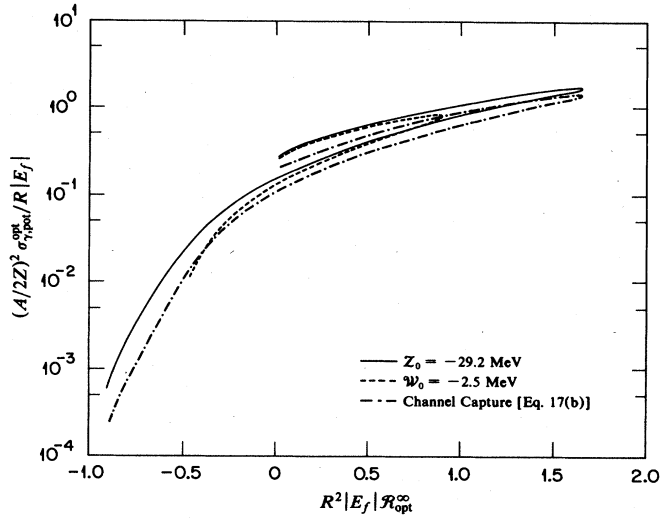

FIG. 14. Potential capture cross section as a function of the distance level parameter. Both quantities have been modified to take partial account of their variations due to differences in binding of the final state, the effective charge, and the nuclear radius. The channel capture cross section is also plotted for comparison.

Eq. (17b), with $\mathcal{R}_{\mathrm{eff}}^{\infty}$ substituted for $\mathcal{R}_J$, shows that the latter expression constitutes a quite good approximation for the background capture cross section (except, again, for very small $\sigma_{\gamma,\mathrm{pot}}$).

In some cases, if the hard sphere-component can be ignored, the capture cross section can be developed from Eq. (28) into a valency form—suitable for energies near but not exactly on fine-structure resonances—involving the reduced valency radiation strength function $s_{\gamma,\mathrm{val}}$ plotted in Fig. 12:

$$\sigma_{\gamma(\mathrm{OR})} = 4\pi R^2 \frac{10^4 E_\gamma{}^3(\mathrm{MeV}^3)}{\sqrt{E(\mathrm{eV})}} \left(\frac{2Z}{A}\right)^2 s_{\gamma,\mathrm{val}} \times \sum g_J \mathcal{W}_{J_f} |\Omega_J|^2 |\mathrm{Re}\,\mathcal{R}_J|^2 \theta_f{}^2 \ . \quad (60)$$

For this expression to be useful, $|\mathrm{Re}\mathcal{R}_J|$ would normally have to be considerably greater than unity—i.e. $|E - E_\lambda| \ll D$ for the nearest resonance level λ. For thermal neutrons, this limitation implies a very large scattering length; for the sulfur isotopes analyzed below, $|\mathrm{Re}\mathcal{R}_J| \ll 1$. Therefore, we return to the comparison between the results given by the approximate channel capture expression and those of the more exact optical model calculations.

XIII. ANALYSIS OF SULFUR DATA

For the practical purposes of analyzing the sulfur data, it now appears that the simplest reliable method for theoretical estimations is to use Eq. (17b) for the channel capture cross section [with a suitable choice of the nuclear potential radius R, and with $\mathrm{Re}\mathcal{R}_J$ determined from thermal neutron scattering properties according to Eqs. (20)–(22)] and then apply a correction factor C_{opt}, depending on the choice of the optical model parameters. We call the calculated cross section thus defined the model-modified channel capture cross section $\sigma_{\gamma(\mathrm{M-CH})}$:

$$\sigma_{\gamma(\mathrm{M-CH})} = C_{\mathrm{opt}}\, \sigma_{\gamma,\mathrm{CH}} \ , \quad (61)$$

where C_{opt} is the ratio of $\sigma^{\mathrm{opt}}_{\gamma,\mathrm{pot}}$ as introduced in Eq. (55) and $\sigma_{\gamma,\mathrm{CH}}$ of Eq. (17b). In the latter equation, we substitute $\mathcal{R}_J = \mathcal{R}^{\infty}_{\mathrm{opt}}$.

The reasons for adopting this approach are as follows. Firstly, at thermal neutron energies the neutron reaction with sulfur isotopes is well off-resonance, and we can neglect any contribution from the valency term $\sigma_{\gamma,\mathrm{val}}$ in Eq. (35). Secondly, although this energy is off-resonance, it is most unlikely to be a "typical" off-resonance situation, described by $\mathcal{R}_J = \mathcal{R}^{\infty}$, in which the effects of wings of local levels are completely absent. In other words, we need to modify the potential capture cross section $\sigma^{\mathrm{opt}}_{\gamma,\mathrm{pot}}$ as given in Eq. (55) to allow for local levels as described by $\mathcal{R}_J = \mathcal{R}^{\infty} + \mathcal{R}_J{}^{\mathrm{loc}}$. Equation (17b) allows us to do this if we know $\mathcal{R}_J$ from thermal scattering properties. Moreover, thirdly, the contribution of the internal component of the matrix element and the modification of the external part owing to the diffuse nature of the optical potential beyond the nuclear radius must be included as accurately as possible. This we do by the inclusion of the factor C_{opt}.

The degree of validity of the channel-capture approximation can be expected to depend on the surface diffuseness parameter d, the magnitude and form of the imaginary potential, and the sign of the spin-orbit coupling. In Fig. 15 we see the effect on C_{opt} of changing d as a function of the p-wave final-state binding energy. The last variable implicitly includes changing values of $\mathcal{R}^{\infty}_{\mathrm{opt}}$. The discontinuities that occur in the curves for larger values of d are associated with the narrow mass-number ranges of rapidly changing potential-scattering properties where the potential-capture cross section becomes very low because of major cancellations in the components of the radial matrix element. In these cases, the radial matrix element becomes very sensitive to the detailed forms of the wave function near the potential radius and to the contribution from the internal region. Apart from these discontinuities, the major feature that is apparent in Fig. 15 is the rather strong dependence of C_{opt} on d; this dependence is due to the weakened attenuation of the tail of the final-state wave function when the potential diffuseness is large. It is also apparent that C_{opt} falls with decreasing final-state binding energy and that the channel-capture approximation seemingly deteriorates below $d \sim 0.4$ fm, whereas one would intuitively expect the approximation to be particularly good for small d (square-well approximation). These observations can be explained by the fact that the approximation $w^2(R) \sim 2/R$ (employed for the value of the final state wave function at the channel radius) used to derive Eqs. (9) and (17) is rather crude. Over the range of final-state energy and mass number covered in our set of calculations, this approximation is always an

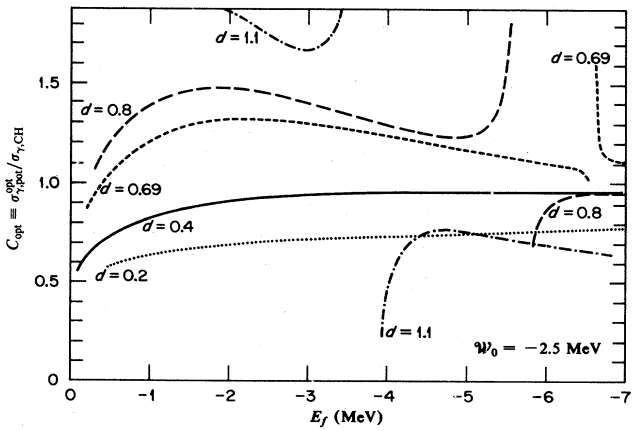

FIG. 15. Dependence of the ratio of potential capture cross section [see Eq. (55b)] to channel capture cross section [see Eq. (17b)] on the surface diffuseness parameter d. Calculations have been made for $j_f = 3/2$ and the volume absorption model. The discontinuities occur when $\sigma_{\gamma,\mathrm{CH}}$ goes to zero.

overestimate (by at least a factor of 1.25) and is particularly poor for small binding energies for which $|w(R)|$ falls rapidly. It should also be noted that for a given binding energy, $|w(R)|$ is smaller for larger surface diffuseness. However, this effect on the magnitude of the potential-capture cross section is more than offset by the effect of the decreasing attenuation of the external wave function mentioned above.

The effect of other features of the optical model potential is shown in Fig. 16. Apart from the discontinuities with the change of sign of the potential-capture amplitude, the sets of curves clearly fall into two groups associated with the difference in spin-orbit coupling of the final state. The generally lower ratio of the $j_f = 1/2$ case is due to the more rapid attenuation (at a given binding energy) of the external wave function due to the added positive potential energy of the spin-orbit term. For a given spin-orbit coupling, however, the potential-capture cross section is, as noted above, insensitive to the details of the optical model for low and moderate values of absorption.

With the $C_{\rm opt}$ approach, we must also consider the complications introduced by the fractionation of the single-particle p-wave state amongst the actual final states, which are spread over a considerable range of energy. In extracting $C_{\rm opt}$ from a diagram such as Fig. 15 or 16, we use the centroid energy of the single-particle state rather than the energies of the individual final states; in this way, we can match the correction factor as accurately as possible to the desired optical model.

An alternative approach to adapting the model for dealing with problems of fragmentation of the p-wave single-particle state is to adopt a specialized optical model for every radiative transition. Thus, the real well-depth $\mathcal{V}_0$, the surface diffuseness d, and the imaginary potential [$\mathcal{W}_0$ or $\mathcal{Z}_0$ and its Gaussian spreading width, b] can all be adjusted within a phenomenologically reasonable range to reproduce both the scattering cross section actually observed at thermal neutron energies and the individual final-state binding energy. We have studied this approach for the sulfur isotopes using a nuclear potential radius of 4.321 fm. We find that varying the real well depth between $\mathcal{V}_0 = -42.8$ and -56 MeV and the surface diffuseness parameter between $d = 0.5$ and 0.8 fm results in values of $C_{\rm opt}$ for the $j_f = 3/2$ state that range from $C_{\rm opt} = 1.22$ (for $\mathcal{V}_0 = -52.4$ MeV, $d = 0.5$ fm, and $E_f = -5.5$ MeV) to $C_{\rm opt} = 1.58$ (for $\mathcal{V}_0 = -44.85$ MeV, $d = 0.8$ fm, and $E_f = -2.45$ MeV). However, varying the surface diffuseness parameter over such a wide range in order to achieve specialized optical models suitable for the wide spread of final-state energies is not satisfactory because it allows too great a deviation of the final-state wave function in the channel from its physically acceptable form. Such a deviation is reflected in the rather wide range of $C_{\rm opt}$ that we have found.

Varying the imaginary potential ($\mathcal{W}_0$ in our study) is a much more reasonable procedure. A reasonable value of surface diffuseness (in this case the "standard" value of $d = 0.69$ fm) is fixed, and this ensures realistic behavior of the final-state wave function in the channel. The variation of the absorption can be considered as a phenomenological, albeit crude, way of accounting for local fine-structure resonance effects that influence the thermal scattering properties. With this procedure and the assumption that $\mathcal{R}_{\rm opt}^{\infty}$ is equal to the observed $\mathcal{R}_J$ we find for ^{32}S + n, for example, for which $\mathcal{R}_J = 0.366$ (when $R = 4.321$ fm), that the $j_f = 3/2$ final state eigenvalue can be varied from -5.05 MeV ($\mathcal{V}_0 = -51$ MeV, $\mathcal{W}_0 = -5$ MeV) with $C_{\rm opt} = 1.43$ to a value of -2.9 MeV ($\mathcal{V}_0 = -46.7$ MeV, $\mathcal{W}_0 = -1.25$ MeV) with $C_{\rm opt} = 1.44$. This range is covered by the branch of $\mathcal{R}_{\rm opt}^{\infty}$ that describes scattering conditions below the s-wave strength function giant resonance. It is possible also to use the branch of $\mathcal{R}_{\rm opt}^{\infty}$ stemming from its reversal of slope through the giant resonance to derive a second range of $C_{\rm opt}$ values. The full range of optical model parameters (and the corresponding $C_{\rm opt}$ values) is given in Appendix C.

Level schemes devoid of superfluous details are desirable prior to attempting a comparison between theory (just outlined) and experiment (previously described). On the one hand, we wish to omit the weaker transitions so that the overall decay patterns become more visible at a glance. On the other hand, because the theory makes use of the $l = 1$ (d,p) spectroscopic strengths, we wish to preserve all of those states with such known (d,p) strengths. Skeleton level schemes based on these criteria are shown in Figs. 17–20. The ^{37}S scheme is from Ref. 2 and the (d,p) strengths are averages of values reported in Refs. 20 and 44.

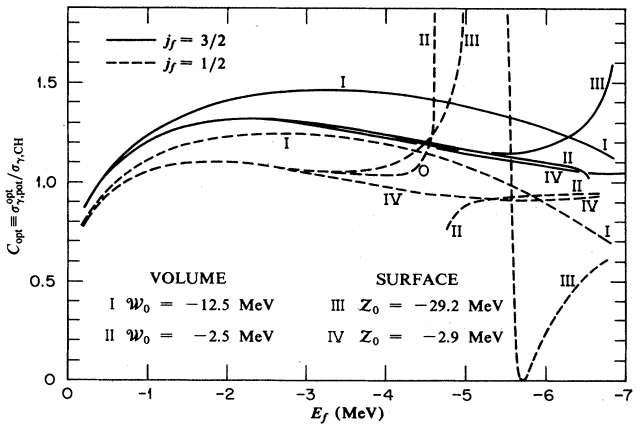

FIG. 16. Dependence of the ratio of potential capture cross section [see Eq. (55b)] to channel capture cross section [see Eq. (17b)] on the magnitude of the imaginary potential. Calculations have been made for surface and volume absorption and for both values of spin-orbit coupling. The surface diffuseness parameter is fixed at $d = 0.69$ fm. The discontinuities occur when $\sigma_{\gamma,\rm CH}$ goes to zero.

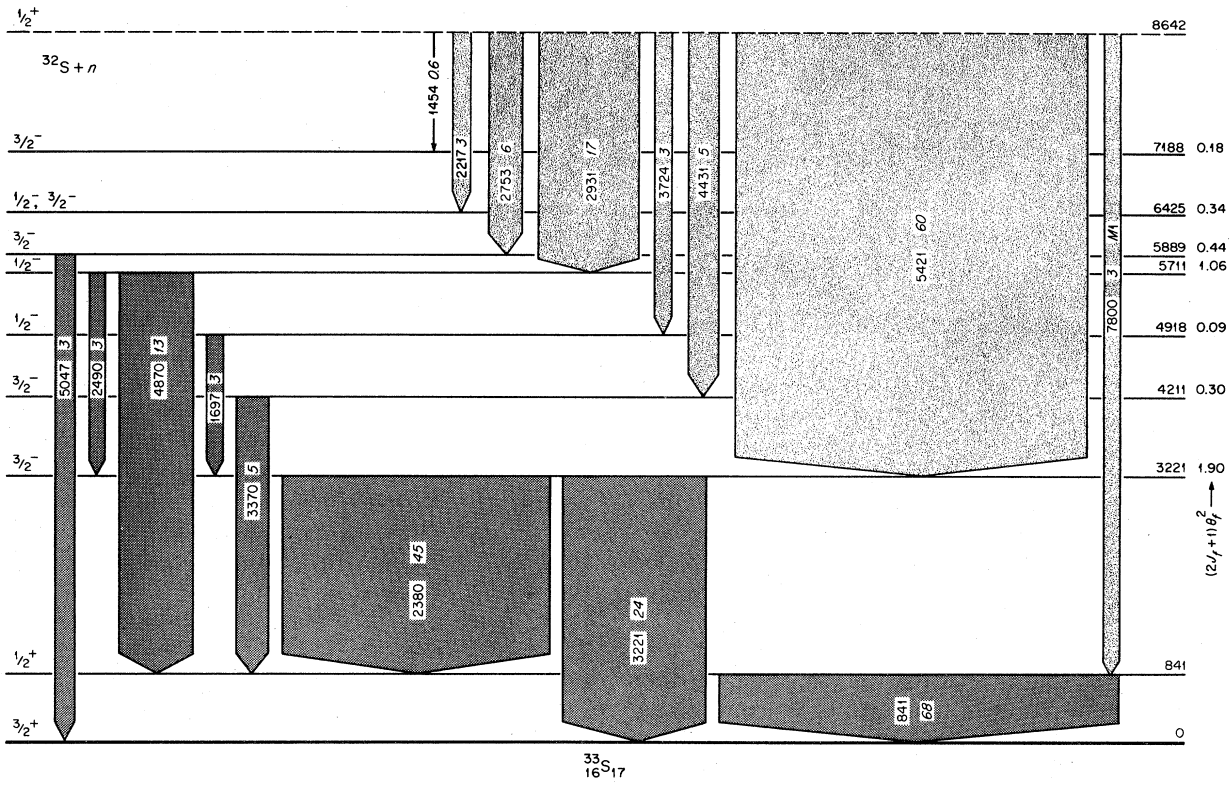

FIG. 17. Skeleton level scheme for ^{33}S. The primary transitions shown account for ≈98% of the capture cross section. The $l = 1$ (d,p) spectroscopic strengths are from Ref. 33.

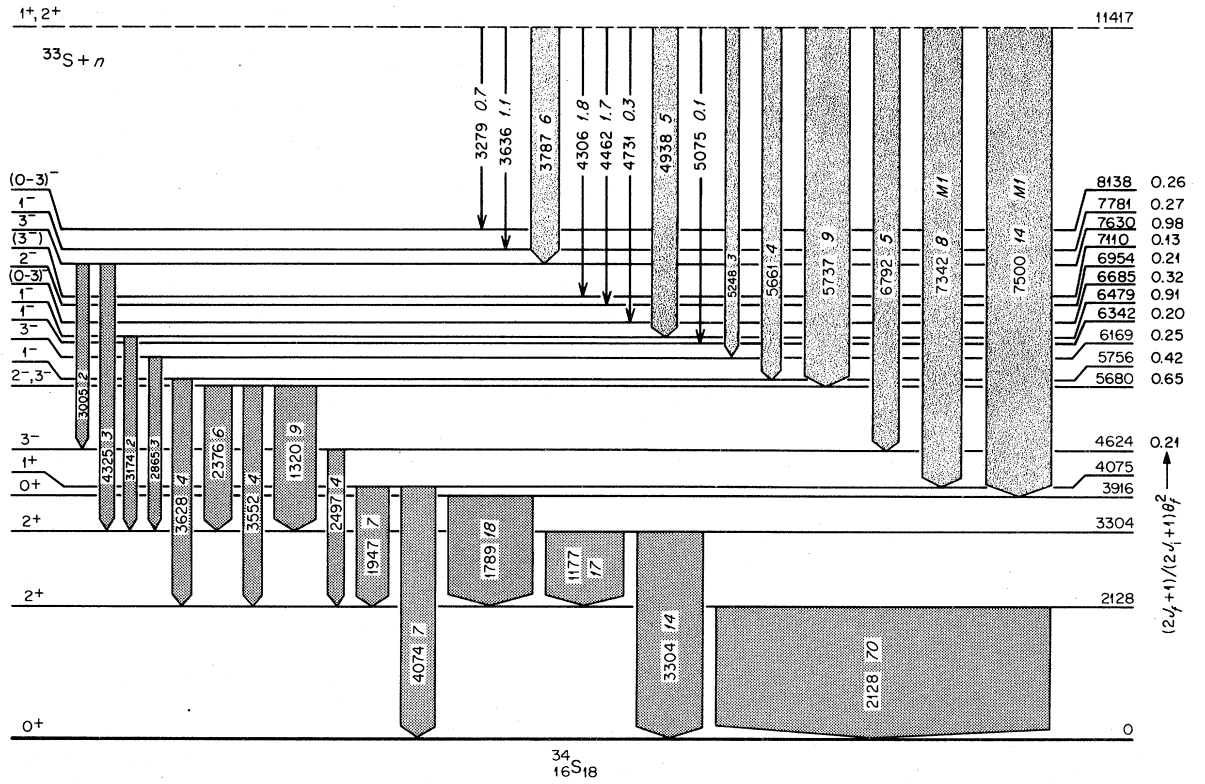

FIG. 18. Skeleton level scheme for ^{34}S. The primary transitions shown account for ≈60% of the capture cross section. The $l = 1$ (d,p) spectroscopic strengths are from Ref. 28.

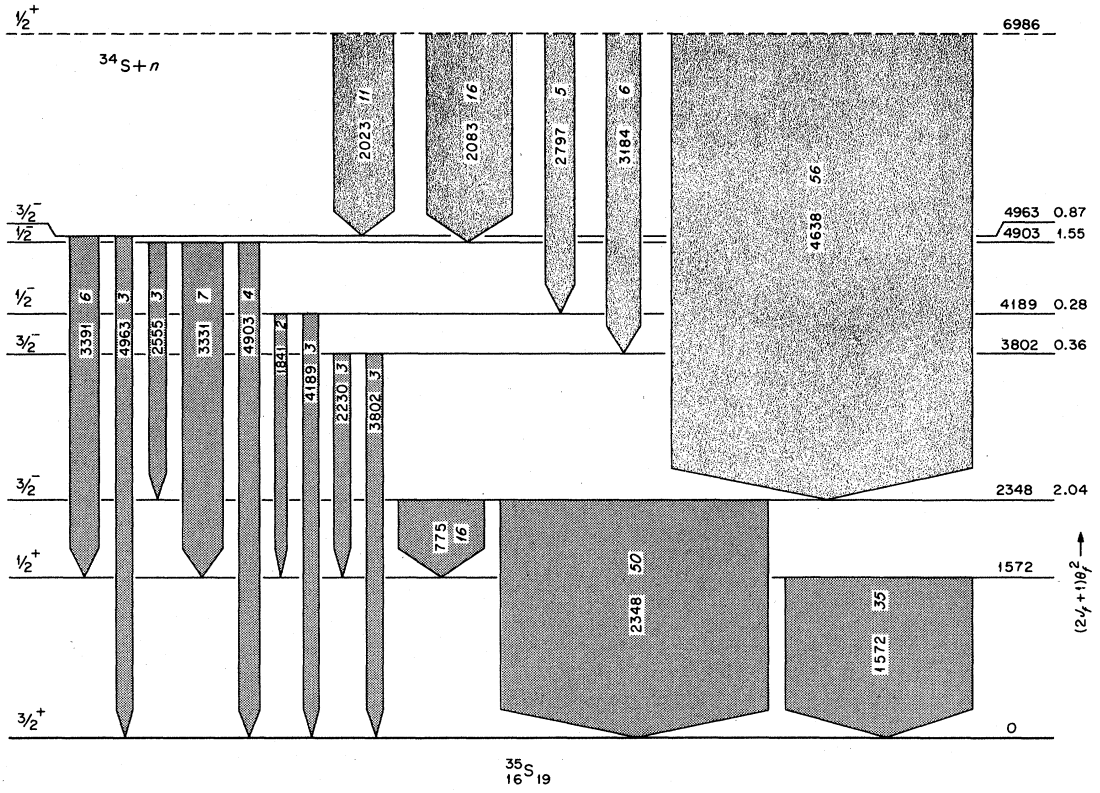

FIG. 19. Skeleton level scheme for ^{35}S. The primary transitions shown account for ≈94% of the capture cross section. The $l = 1$ (d,p) spectroscopic strengths are from Ref. 19.

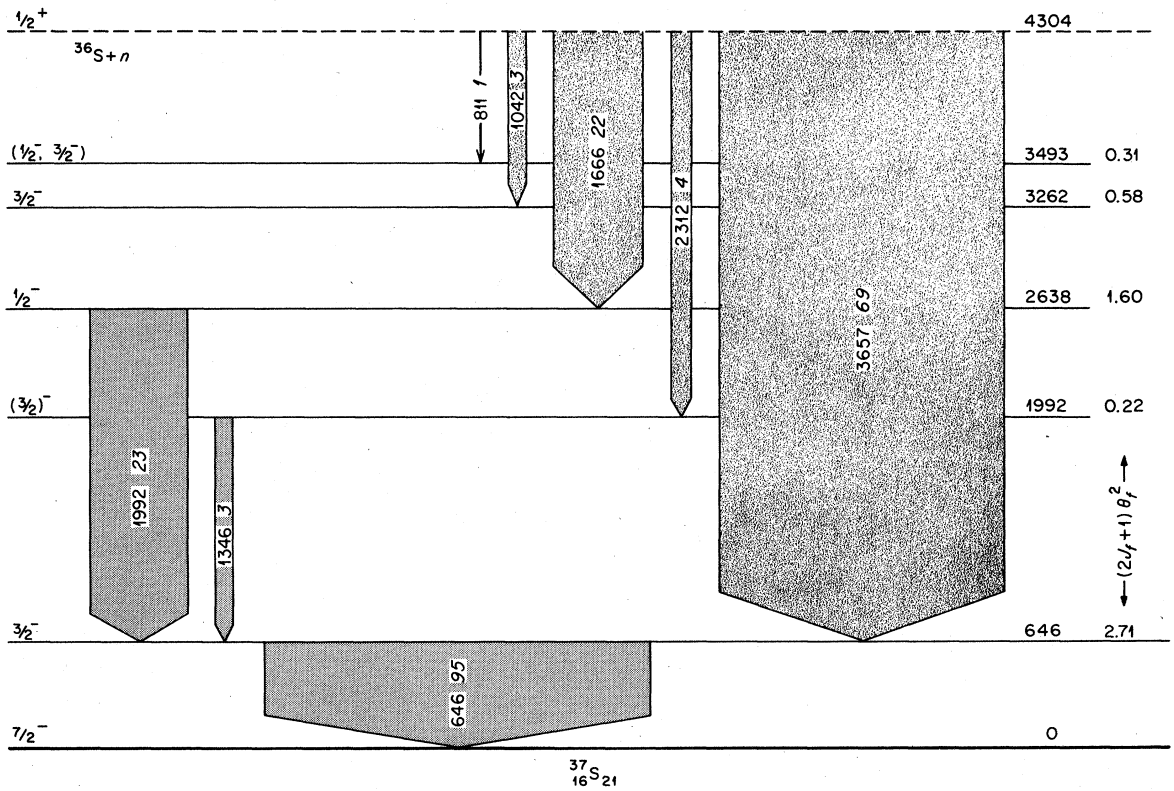

FIG. 20. Skeleton level scheme for ^{37}S. The primary transitions shown account for ≈100% of the capture cross section. The $l = 1$ (d,p) spectroscopic strengths are averages of values reported in Refs. 20 and 44.

The γ-ray energy dependence of the hard-sphere capture cross section has been already remarked upon in connection with Eq. (10). For channel capture dominated by the wings of local levels, the cross section is proportional to the square of the energy [the dominance of the y^4 term in Eq. (17b)]. This kind of general behavior in the data is established by studying the correlation coefficient between the electric dipole capture cross sections (to specific final states) divided by the nth power of the γ-ray energy, and the reduced single-particle p-state width θ_f^2. This is shown in Fig. 21 as a function of n for the four sulfur isotopes studied in this and previous[2] works. For the ^{34}S target the correlation coefficient peaks below $n = 1$ with a value of 1; it is still greater than 0.96 at $n = 1$, and falls away sharply for $n > 1$. This hard-sphere capture behavior is also borne out by the ^{36}S and ^{32}S targets, although the correlation coefficients are not nearly as strongly peaked and do not fall away steeply until $n > 1.5$ for ^{36}S and $n > 2$ for ^{32}S. For the ^{33}S target, the correlation coefficient does not reach unity (this is expected because of complexity of spin-coupling effects); and, although it peaks slightly at $n = 2$ (suggesting resonance effects in channel capture), no strong evidence on the γ-ray energy dependence is provided by the data.

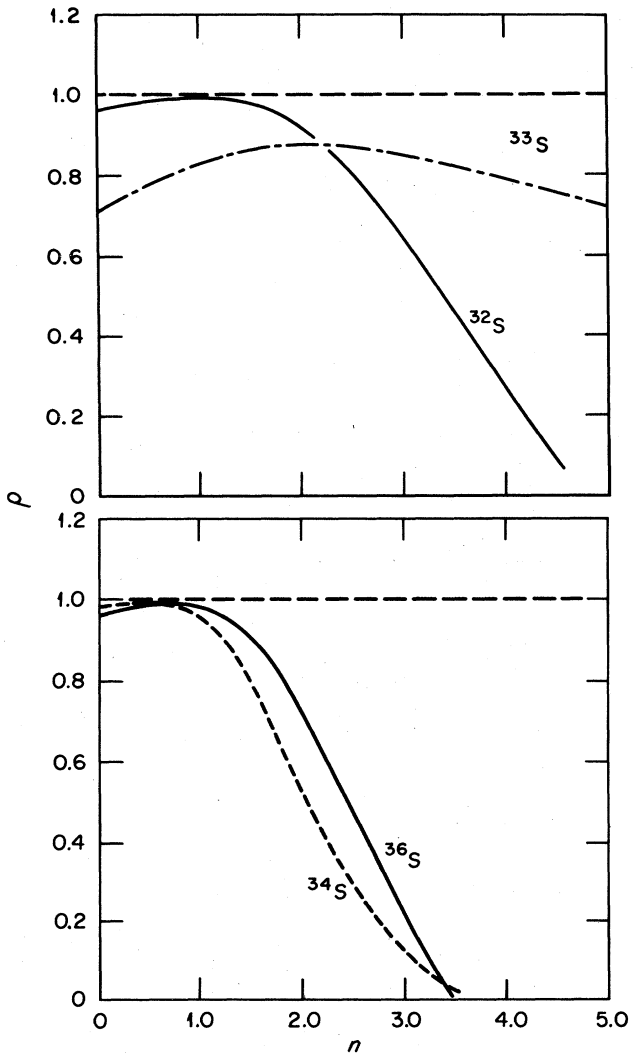

FIG. 21. The ordinate shows the correlation coefficient between the electric dipole capture cross section divided by the nth power of the primary γ-ray energy and the reduced single-particle width θ_f^2. The curves are labelled by the targets studied.

The choice of nuclear potential radius R can be made from an analysis of the centroid energies of the single-particle $p_{3/2}$ and $p_{1/2}$ states determined from (d,p) stripping data for these isotopes. The data on ^{32}S(d,p) suggest that the $p_{3/2}$ is centered at $E_f \sim -3.6$ MeV, and the $p_{1/2}$ state at $E_f \sim -2.1$ MeV. The data on ^{34}S(d,p) put the $p_{3/2}$ state in this nucleus at about -3.2 MeV. The consensus of these values would suggest, from Fig. 11, a nuclear potential radius of $R \sim 4.6$ fm, which we shall employ as a starting value for analyzing the capture data on all the sulfur isotopes.

The scattering data for the extraction of $\mathcal{R}_J$ values for the sulfur isotopes have been measured by Koester *et al.*[45] For ^{32}S + n, the scattering length is 2.740 ± 0.003 fm; this yields $\mathcal{R}_{J=1/2} = 0.404$ for $R = 4.6$ fm. This value combined with the standard values of C_{opt}, calculated from the optical model described in Section XII with parameters $\mathcal{V}_0 = -42.8$ MeV, $\mathcal{W}_0 = -2.5$ MeV, $R = 4.6$ fm, and $d = 0.69$ fm, yields calculated values shown in column (a) of Table XVI for the thermal cross sections for transitions in ^{33}S. The values of C_{opt} used were 1.36 for $j_f = 3/2$ final states and 1.17 for $j_f = 1/2$ final states. Alternatively we have used a potential radius of 4.2 fm ($\mathcal{R}_{1/2} = 0.347$) with the same standard C_{opt} factors to give a second estimate [column (b)] based on what is believed to be a better value for the potential radius of the sulfur isotopes. The third value listed [column (c)] is based on individual C_{opt} factors computed for each individual transition from an optical model specialized for that transition (see Appendix C). In this case the radius employed, $R = 4.321$ fm, is that of our "standard" potential given below Eq. 57, and $\mathcal{R}_{1/2} = 0.366$.

The second even target nucleus ^{34}S has a scattering length $a_{sc,J} = 3.40 \pm 0.03$ fm, which implies $\mathcal{R}_{1/2} = 0.261$ for the potential radius $R = 4.6$ fm; $\mathcal{R}_{1/2} = 0.191$ for $R = 4.2$ fm, and $\mathcal{R}_{1/2} = 0.213$ for $R = 4.321$ fm. As before, standard C_{opt} factors are used for the first two choices and specialized model factors for the third.

The same procedure is adopted for calculation of the cross sections of the odd isotope ^{33}S. Here, the coherent scattering cross section is known quite well as 2.68 ± 0.2 b. Until recently, the total scattering cross section was known very inaccurately: $\sigma_{\text{th,total}} = 2.8 \pm 0.7$ b. Preliminary analysis of very recent data from a total cross-section measurement by Moxon[46] indicates that the total scattering cross section is very close to the coherent scattering cross section (within the experimen-

tal error of the latter). This indicates that the scattering lengths for both channel spins, $J = 1$ and $J = 2$, are approximately equal at the value $a_{sc,J} = 4.68$ fm. Therefore, for the three choices of potential radius, the $\mathcal{R}_J$ values are -0.0043, -0.1, and -0.07, respectively.

The third approach to calculating the cross sections [column (c) of Table XVI] is based on specialized C_{opt} factors and seems to us to be the most self consistent. It gives values midway between those of the other two methods [columns (a) and (b)] based on "standard" C_{opt} factors and centroid energies of the single-particle $p_{1/2}$ and $p_{3/2}$ states. The overall agreement between column (c) and the experimental data is good; the ratios of calculated to experimental values for the stronger transitions generally fall within three standard deviations of unity. However, some of the weaker transitions deviate considerably from the theoretical estimates. This is especially noticeable in the $^{33}S + n$ case. Here, the 5075 keV transition is only 0.4 mb compared with an expected value of 9.0 mb and the 4731 keV transition is only 1.6 mb whereas 14 mb is expected.

These discrepancies may well result from a compound-nucleus contribution to the total radiative matrix element. Assuming that this is the case, the minimum strength of the compound-nucleus component can be deduced from the expression

$$\sigma_{\gamma(\text{CN})} = [\sigma_{\gamma(\text{M-CH})}^{1/2} - \sigma_{\gamma}^{1/2}]^2 \ . \tag{62}$$

For each isotope there is a considerable scatter in the values of $\sigma_{\gamma(\text{CN})}$ thus deduced, as would be expected from a Porter-Thomas statistical distribution of these components. For the three cases, the mean value of $\sigma_{\gamma(\text{CN})}/E_\gamma{}^3$ is found to be:

$^{32}S + n$: $\sigma_{\gamma(\text{CN})}/E_\gamma{}^3 = 0.110$ mb MeV^{-3},
$\Sigma\, \sigma_{\gamma(\text{CN})} = 7.2$ mb for 7 transitions;

$^{33}S + n$: $\sigma_{\gamma(\text{CN})}/E_\gamma{}^3 = 0.018$ mb MeV^{-3},
$\Sigma\, \sigma_{\gamma(\text{CN})} = 17.0$ mb for 12 transitions;

and

$^{34}S + n$: $\sigma_{\gamma(\text{CN})}/E_\gamma{}^3 = 0.049$ mb MeV^{-3},
$\Sigma\, \sigma_{\gamma(\text{CN})} = 5.2$ mb for 5 transitions.

These values are to be compared with the estimates derived by assuming that the neutron energy lies midway beween levels in a uniform picket-fence model of the resonance structure and by using the formula for partial radiation widths derived by Cameron[47] from a global analysis of experimental data; these estimates ($\sigma_{\gamma(\text{CN})}/E_\gamma{}^3 = 0.009$ mb MeV^{-3}) are in reasonable agreement with the values for $^{33}S + n$ and $^{34}S + n$ above. In the case of $^{32}S + n$, $\mathcal{R}_{1/2}$ is high, indicating a strong and possibly closer than average (i.e., less than half the mean level spacing) fine-structure resonance that will considerably augment the compound-nucleus contribution to the capture cross section. The parameters of such a resonance are known from total neutron cross-section studies by Halperin *et al.*[48] Using the quoted neutron width $\Gamma_n = 15$ keV and resonance energy, 102.7 keV, together with an estimate of total radiation width $\Gamma_\gamma = 0.3$ eV based on Cameron's formula and a level density function,

$$D_{J^\pi=1/2^-}^{-1} + D_{J^\pi=3/2^-}^{-1} = 0.3 \exp(E^*/2.13)\ \text{MeV}^{-1} \ ,$$

with a cut-off to zero below an excitation energy $E^* = 3$ MeV (no $J^\pi = 1/2^-$ or $3/2^-$ levels occurring so low), we estimate that the contribution of this resonance to the thermal capture cross section is about 6 mb. This estimate is in close agreement with the summed estimates of $\sigma_{\gamma(\text{CN})}$ for $^{32}S + n$ deduced above. Thus, even in this case it is interesting and instructive to see how the potential-plus-channel capture mechanism dominates the compound-nucleus contribution. For $^{32}S + n$, the theoretical total potential capture cross section for the transitions listed in Table XVI is 556 mb, which clearly accounts for virtually all of the observed thermal-capture cross-section value of 530 ± 40 mb. For $^{33}S + n$, the summed theoretical cross section (making a best-guess attribution of spin-orbit coupling when this is ambiguous) is 225 mb, compared with the experimental total capture cross section of 350 ± 40 mb; and for $^{34}S + n$ it is 344 mb compared with 270 ± 40 mb.

We have dealt with the case of $^{36}S + n$ separately in Table XVII because the potential scattering length is not known. In this case we have employed $R = 4.6$ fm for the potential radius, a range of $\mathcal{R}_{1/2}$ values (namely 0.0, 0.2 and 0.4) and the "standard" C_{opt} factors. It is apparent that best agreement is obtained with the experimental data for a $\mathcal{R}_{1/2}$ value of about 0.2. Again, the agreement of theory with the data shows the dominance of the potential capture plus channel mechanism over the compound-nucleus contribution. The sum of the theoretical estimates for the five transitions listed in Table XVII is 254 mb (for $\mathcal{R}_{1/2} = 0.2$), compared with the experimental total capture cross section of 230 ± 20 mb.

The overall predominance in the thermal region of potential plus channel capture over the compound-nucleus contribution (deduced from theory and experiment) suggests that the simple valence mechanism may also be significant, if not predominant, in the resonances. The radiation widths of the broad s-wave scattering resonances of these very light nuclides are extremely difficult to measure. The available evidence, supported by our analysis above of the thermal neutron spectroscopic data, suggests that they are of the order of 1 to 2 eV, considerably greater than the value of 0.3 eV deduced for the compound nucleus mechanism from Cameron's statistical formula. We can, in fact, use the computed value of the valence radiation strength function given in Fig. 12 [see also Eqs. (56) and (59)] to deduce the valence total radiation width of the 102.7-keV resonance in the cross section of ^{32}S. The expression for the partial radiation widths to the final states listed in Table XVI is

Table XVI. Comparison between theory and experiment for the cross sections of primary γ-ray transitions following thermal neutron capture by ^{32}S, ^{33}S, and ^{34}S. The (a), (b), and (c) types of calculations are described in Sec. XII.

Final nucleus	Level energy (keV)	J_f^π	Primary γ-ray energy (keV)	Calculation of $\sigma_{\gamma(M-CH)}$ (in mb)						Expt. σ_γ (mb)
				$j \to 1/2$	1/2	1/2	3/2	3/2	3/2	
				$R \to 4.6$ fm	4.2 fm	4.321 fm	4.6 fm	4.2 fm	4.321 fm	
				(a)	(b)	(c)	(a)	(b)	(c)	
^{33}S	3221	$3/2^-$	5421	...	...	...	396	310	347	302 ± 27
	4211	$3/2^-$	4431	...	...	...	49.1	38.9	44.4	25.2 ± 2.3
	4918	$1/2^-$	3724	10.3	8.3	9.6	...	...	...	13.5 ± 1.3
	5711	$1/2^-$	2931	92.8	75.5	88.2	...	...	...	87 ± 9
	5889	$3/2^-$	2753	...	...	...	41.8	34.1	38.4	28.7 ± 2.8
	6425	$1/2^-$ or $3/2^-$	2217	21.9 ...	18.1 ...	21.0 ...	... 25.4	... 21.1	... 23.0	13.3 ± 1.2
	7188	$3/2^-$	1454	...	...	...	8.6	7.3	7.3	2.8 ± 0.3
^{34}S	4624	3^-	6792	...	...	...	15.3	9.7	12.3	24.2 ± 2.3
	5680	2^- or 3^-	5737	36.1 ...	23.8 ...	30.3 ...	41.9 41.9	27.7 27.7	36.6 36.6	43 ± 4
	5756	1^-	5661	23.1	15.3	19.4	26.8	17.8	23.5	18.4 ± 1.8
	6169	3^-	5248	...	...	...	15.1	10.2	13.5	11.8 ± 1.1
	6342	1^-	5075	10.2	6.9	9.0	11.8	8.0	10.8	0.4 ± 0.1
	6479	1^-	4938	45.2	30.8	40.2	52.5	35.8	48.0	22.2 ± 2.1
	6685	0^- 1^- 2^- 3^-	4731	... 15.4 15.4 ...	... 10.6 10.6 ...	... 14.0 14.0 ...	18.0 18.0 18.0 18.0	12.4 12.4 12.4 12.4	16.5 16.5 16.5 16.5	1.6 ± 0.2
	6954	2^-	4462	9.7	6.8	9.0	11.3	7.9	10.5	7.9 ± 0.8
	7110	$(3)^-$	4306	...	...	...	6.8	4.8	6.4	8.3 ± 0.8
	7630	3^-	3787	...	...	...	46.7	33.6	44.4	26.5 ± 2.5
	7781	1^-	3636	10.8	7.8	10.3	12.5	9.0	11.9	5.2 ± 0.6
	8138	0^- 1^- 2^- 3^-	3279	... 9.6 9.6 ...	... 7.1 7.1 ...	... 9.4 9.4 ...	11.2 11.2 11.2 11.2	8.2 8.2 8.2 8.2	10.8 10.8 10.8 10.8	3.2 ± 0.4
^{35}S	2348	$3/2^-$	4638	...	...	...	227	175	205	163 ± 15
	3802	$3/2^-$	3184	...	...	...	27.1	21.5	25.2	18.2 ± 1.7
	4189	$1/2^-$	2797	15.9	12.8	14.7	...	...	...	15.9 ± 1.5
	4903	$1/2^-$	2083	65.4	53.6	61.8	...	...	...	46 ± 5
	4963	$3/2^-$	2023	...	...	...	41.7	34.2	37.5	33.6 ± 3.0

Table XVII. Comparison between theory and experiment (Ref.2) for the cross sections of primary γ-ray transitions following thermal neutron capture by ^{36}S. The calculations are based on a nuclear potential radius of 4.6 fm.

Final nucleus	Level energy (keV)	J_f^π	Primary γ-ray energy (keV)	Calculation of $\sigma_{\gamma(M-CH)}$ (in mb)						Expt. σ_γ (mb)
				$j \to 1/2$	1/2	1/2	3/2	3/2	3/2	
				$\mathcal{R}_{1/2} \to 0.0$	0.2	0.4	0.0	0.2	0.4	
^{37}S	646	$3/2^-$	3657	...	...	...	108	184	279	161 ± 18
	1992	$(3/2)^-$	2312	...	...	...	6.3	9.5	13.6	9.4 ± 1.2
	2638	$1/2^-$	1666	30.8	44.1	59.9	...	...	...	52 ± 7
	3262	$3/2^-$	1042	...	...	...	9.1	12.1	15.6	8.1 ± 1.0
	3493	$1/2^-$ or $3/2^-$	811	3.5 ...	4.5 ...	5.6 ...	... 4.0	... 5.2	... 6.5	2.4 ± 0.3

$$\Gamma_{\gamma,\mathrm{val}} = 10^4 E_\gamma{}^3 \left[\frac{2Z}{A}\right]^2 s_{\gamma,\mathrm{val}}^{\mathrm{opt}}\, \Gamma_n{}^{(0)}\, \mathcal{W}_{J_f}\, \theta_f{}^2 \ , \quad (63)$$

where E_γ is in MeV. The sum of the valence radiation widths to these states is 1.7 eV, compared with the estimate of 0.25 eV from the Cameron formula. The relative intensities of the transition from this resonance are in semi-quantitative agreement with the measured spectrum.[49] The largest partial width (to the state at 3.22 MeV with $\Gamma_{\gamma,\mathrm{val}} = 1.04$ eV), is about three times that of the next largest (to the state at 5.71 MeV with $\Gamma_{\gamma,\mathrm{val}} = 0.4$ eV). The Cameron compound nucleus estimates for these widths are 0.1 eV and 0.017 eV, respectively. The remaining valence partial radiation widths are of the same order of magnitude as the compound nucleus estimates.

XIV. SUMMARY AND CONCLUSIONS

We have investigated the γ-ray emission after thermal neutron capture by ^{32}S, ^{33}S, and ^{34}S targets. The emission from a ^{36}S target was reported separately.[2] A large number of γ rays was detected: ~100 from ^{32}S, ~270 from ^{33}S, ~60 from ^{34}S, and ~15 from ^{36}S. Most of these γ rays were incorporated into level schemes that required 26 excited states in the final nucleus ^{33}S, 70 in ^{34}S, 20 in ^{35}S, and 7 in ^{37}S. The measurements are complete in the sense that the assigned primary transitions account for >95% of the capture cross section for the ^{32}S, ^{34}S, and ^{36}S targets and as much as 83% for the ^{33}S target. The ^{33}S target is inherently difficult to study because ^{34}S has a very high neutron-separation energy.

Perhaps the most striking feature of this vast and comprehensive array of data on the thermal neutron capture transitions in the isotopes of sulfur is the overwhelming predominance of certain primary electric dipole transitions to final states that are also strongly excited in the (d,p) stripping reactions on these isotopes. These transitions are therefore clear candidates for explanation by the theory of low-energy direct capture. According to this theory, the main contribution to the matrix element describing the capture amplitude comes from the overlap of the channels of the incident and bound single-particle neutron in the initial and final states, respectively. We have reviewed and developed this theory of potential capture and have shown by methods of $\mathcal{R}$-matrix theory that our prescription is a reasonably sound one for calculating the potential capture cross section. (This cross section is due to the distortion of the incident wave function both by the overall potential field and the long-range effects of distant resonance levels.) We have done this by calculating capture in an optical model potential (duly separating out a term due to average effects of capture in local resonances). We then presented numerical estimates for the capture cross section in an optical model potential of realistic Woods-Saxon form and compared these with the corresponding simplified formula for the channel capture cross section. We have shown that there is considerable dependence of the magnitude of the potential capture cross section as compared with the channel capture estimate on the parameterization of the optical model, especially on the edge diffuseness and, to a lesser extent, on the absorption potential. We have shown that for a realistic degree of potential edge diffuseness, the potential capture cross section of light to medium nuclides can be 10 to 30% greater than the equivalent channel capture estimate for $j_f = 1/2$ final states and 30 to 60% greater for $j_f = 3/2$ final states. We have presented prescriptions for adapting the channel-capture formula (which incorporates an $\mathcal{R}$-function parameter to account for the effect on the incident channel wave function of local and distant resonance levels) to take account of the optical model features.

We have used this quantitative theory of potential capture to make detailed theoretical estimates of the cross sections of the principal $E1$ primary transitions in all those sulfur isotopes we have studied via thermal neutron capture. In the first place we can expect, as is well-known, that the $E1$ transition strengths, after removal of a certain gamma-ray energy dependence, should be fully correlated with the p-wave spectroscopic factors of the final states as deduced from (d,p) stripping measurements. We have checked this correlation and shown that it is complete when the extracted gamma-ray energy factor has simply a linear dependence on energy. A linear dependence is expected from the current theory in a fully off-resonance situation, as distinct from the normal cubic dependence usually assumed for $E1$ transitions from compound nuclear processes.

The cross sections of most of the strong $E1$ transitions in this series agree with our best theoretical estimates within 30% or so (compared with experimental errors of the order of 10%). There are a few weak transitions in the experimental data to states with quite significant spectroscopic factors [as deduced from (d,p) stripping reactions]; these states should therefore have moderately large cross sections according to the theory. From these cross sections, together with the scatter of the other cross sections about their theoretical expectations, we have been able to deduce an estimate of the compound-nucleus contribution to capture from local resonances. This turns out in all cases to be in semi-quantitative agreement with the estimate we can form from our global knowledge of radiative capture in neutron resonances. This indirect information on the strength of the strictly compound-nucleus contribution to neutron capture by the sulfur isotopes, together with our estimates of the strength of valence capture in s-wave resonances derived from the optical model calculations, allows us to infer that the valence mechanism will be predominant also in strong s-wave neutron resonances. Thus the

analysis of the extensive data accumulated on the series of sulfur isotopes allows us to make two conclusions: (1) the electric dipole potential and channel capture is a significant (if not predominant) mechanism for capture of slow neutrons at off-resonant energies by medium-light nuclei and (2) the closely related valence mechanism is important at resonance energies, even for nuclei in which the valence conditions are not enhanced by association with the giant resonance in the s-wave (or p-wave) neutron strength function.

ACKNOWLEDGEMENTS

We thank M. C. Moxon for carrying out total cross-section measurements on ^{33}S and making available his preliminary results. We thank him again and H. Weigmann for helpful discussions concerning this paper. We are grateful to D. A. McClure and G. G. Slaughter for computer programs that automatically generated several tables from punched cards. In this connection, we would like to also mention and thank Betty McHargue and Nancy Smith. R. W. Sharpe provided expert editorial assistance. One of us, Eric Lynn, is grateful to the Oak Ridge National Laboratory for providing kind hospitality during the summers of 1982 and 1983. The current research was sponsored by the Division of Basic Energy Sciences, U.S. Department of Energy, under contract No. DE-AC05-84OR21400 with the Martin Marietta Energy Systems. Inc. (Oak Ridge), and contract No. W-7405-Eng-36 with the University of California (Los Alamos).

APPENDIX A

$\mathcal{R}$-matrix representation of optical models

We start from the radial component, limited to s waves, of the Schrödinger equation for the optical model

$$-\frac{\hbar^2}{2m}\frac{\partial^2 V}{\partial r^2}+[\mathcal{V}(r)+\mathrm{i}\mathcal{W}(r)]V=EV. \tag{A.1}$$

At two different energies E_1 and E_2, we have eigensolutions V_1 and V_2. Multiplying the equations for V_1 and V_2 by V_2 and V_1, respectively, and integrating from 0 to the channel radius a, we obtain by subtraction

$$\int_0^a \mathrm{d}r\left[V_2\frac{\partial^2 V_1}{\partial r^2}-V_1\frac{\partial^2 V_2}{\partial r^2}\right]+\frac{2m}{\hbar^2}(E_1-E_2)\int_0^a \mathrm{d}r\, V_1V_2=0\ . \tag{A.2}$$

V_1 and V_2 must be regular at the origin; hence, integration of the first term by parts gives

$$\left[V_2\frac{\partial V_1}{\partial r}-V_1\frac{\partial V_2}{\partial r}\right]_{r=a}+\frac{2m}{\hbar^2}(E_1-E_2)\int_0^a \mathrm{d}r\, V_1V_2=0\ . \tag{A.3}$$

If a boundary condition

$$\left[\frac{1}{V_q}\frac{\partial V_q}{\partial r}\right]_{r=a}=B \tag{A.4}$$

is imposed, a set of discrete eigenstates V_q with complex eigenvalues $(E_q-\mathrm{i}W_q)$ can be established. Equations (A.3) and (A.4) together allow the orthonormality relation

$$\int_0^a \mathrm{d}r\, V_q V_{q'}=\delta_{qq'}\mathrm{e}^{\mathrm{i}\omega_q} \tag{A.5}$$

to be established.

For a general solution of the Schrödinger equation (A.1) at arbitrary energy E, we can use the expression

$$V_E=\sum_q A_q V_q\ . \tag{A.6}$$

The expansion coefficients are given by

$$A_q e^{i\omega_q} = \int_0^a dr\, V_q V_E \ . \tag{A.7}$$

Therefore, from Eqs. (A.3) and (A.4),

$$A_q = \frac{\hbar^2}{2m}\left[\left(\frac{\partial V_E}{\partial r}\right)_{r=a} - BV_E(a)\right]\frac{V_q(a)e^{-i\omega_q}}{E_q - E - iW_q} \ , \tag{A.8}$$

that is

$$V_E(r) = \frac{\hbar^2}{2ma}\sum_q \frac{V_q(a)e^{-i\omega_q}V_q(r)}{E_q - E - iW_q}\left[a\left(\frac{\partial V_E}{\partial r}\right)_{r=a} - BaV_E(a)\right] \ , \tag{A.9}$$

which is the $\mathcal{R}$-matrix relationship connecting the derivative of V_E and its value. The $\mathcal{R}$ function from which the collision function and, hence, the cross sections of the optical model are calculated is

$$\mathcal{R} = \left(\frac{\hbar^2}{2ma}\right)\sum_q \frac{V_q^2(a)e^{-i\omega_q}}{E_q - E - iW_q} \ . \tag{A.10}$$

This expression is used in Eq. (40) of the main text.

For the complex potential $\mathcal{V}(r) + i\mathcal{W}(r)$, the eigenfunctions V_q will, in general, be complex. Proceeding as in the derivation of Eq. (A.3), but multiplying Eq. (A.1) and its conjugate by the conjugate of V, we can obtain the following relations [for real boundary condition Eq. (A.4)]:

$$(E_q - E_{q'})\int_0^a dr\,\mathrm{Re}(V_{q'}^* V_q) - (W_q + W_{q'})\int_0^a dr\,\mathrm{Im}(V_{q'}^* V_q) + 2\int_0^a dr\,\mathrm{Im}(V_{q'}^* V_q)\mathcal{W}(r) = 0 \ . \tag{A.11}$$

$$(W_q + W_{q'})\int_0^a dr\,\mathrm{Re}(V_{q'}^* V_q) + (E_q - E_{q'})\int_0^a dr\,\mathrm{Im}(V_{q'}^* V_q) - 2\int_0^a dr\,\mathrm{Re}(V_{q'}^* V_q)\mathcal{W}(r) = 0 \ . \tag{A.12}$$

We obtain from Eq. (A.12) a result

$$W_q = \int_0^a dr\,|V_q(r)|^2 W(r) \Big/ \int_0^a dr\,|V_q(r)|^2 \ , \tag{A.13}$$

which was given earlier by Porter.[50]

In one special case, when $\mathcal{W}(r)$ has the constant value $\mathcal{W}_0$ from $r = 0$ to a_c, the eigenfunctions are real although from Eq. (A.13) the eigenvalues have the imaginary component $\mathcal{W}_0$. Using these properties, we see immediately that the distant level $\mathcal{R}$ function and strength function of Eqs. (48) and (49) have the simple forms given in Eqs. (51) and (52), thus reflecting the Cauchy form of spreading [Eq. (50)] of the single-particle state into the compound nucleus state λ. The Cauchy form (Lorentz spreading) is the simplest form of mixing of a special state with a dense set of background states and is a consequence of constancy in the magnitude of the mixing matrix elements across the background region—i.e., a fully statistical mechanism for compound nucleus formation, which is intuitively consistent with the model of constant absorption potential $\mathcal{W}$ over the nuclear interior. Complexity of the eigenfunctions leads to departures of S_{opt} [see Eq. (52)] from the Lorentz form and, hence, to other forms for the spreading function $C_p^2(E_\lambda)$ into the fine structure states. The mechanism for such forms of spreading can be linked to more localized behavior of the absorbing term $\mathcal{W}$ in the Hamiltonian.

If $\mathcal{W}(r)$ has a more general behavior, numerical integration of Eq. (A.1) is required to determine the essential properties of the eigenfunctions. A computer program CPBDY has been written in FORTRAN to accomplish this. The potential $\mathcal{V} + i\mathcal{W}$ is assumed constant in a very small region of r from $r = 0$ to $r = r'$, so the wave function for the roughly estimated complex eigenvalue E_λ is assumed to have the spherical Bessel form $\rho j_l(\rho)$ in this region [for the generalized version of Eq. (1) in which a centrifugal term is included]. The argument ρ is complex and is equal to k_λ, where $k_\lambda^2 = (2m/\hbar^2)[E_\lambda - \mathcal{V}(0) - i\mathcal{W}(0)]$. The wave function and its derivative at r' are calculated and then integration of Eq. (A.1) by a standard technique to $r = r''$ is effected; this function is labled V_{out}. The value of r'' is such that it is reasonably close to the potential well radius R, while at the same time $E_\lambda - \mathcal{V}(r)$ is positive, and the wave function is far from a nodal position.

At the channel radius a, the wave function is assumed to have the value $V(a)=v+iu$, and its derivative is given by Eq. (A.4). For real boundary condition

$$\left[\frac{1}{v}\frac{\partial v}{\partial r}\right]_{r=a}=\left[\frac{1}{u}\frac{\partial u}{\partial r}\right]_{r=a}=B\ . \tag{A.14}$$

The ratio $u(a)/v(a)$ is estimated at the commencing iteration. From these conditions, the wave function $V_{\text{in}}(r)$ is integrated numerically inward to r''. From the degree of mismatch of $V_{\text{in}}(r'')$ and $V_{\text{out}}(r'')$, a new estimate of the eigenvalue E_λ is obtained:

$$E_\lambda(\text{new})=E_\lambda(\text{old})+\left[\frac{\hbar^2}{2m}\right]\left[\frac{(V_{\text{out}}'/V_{\text{out}})_{r=a}-(V_{\text{in}}'/V_{\text{in}})_{r=a}}{(1/V_{\text{out}}(a))^2\int_0^{r''}dr\,V_{\text{out}}^2+(1/V_{\text{in}}(a))^2\int_{or''}^{a}dr\,V_{\text{in}}^2}\right]\ . \tag{A.15}$$

Also new values of v and u for the reiterated solution of V_{in} are obtained by multiplication of the previous solution at $r=a$ by the ratio $V_{\text{in}}(r'')/V_{\text{out}}(r'')$.

When the criterion of convergence of the eigenvalue is satisfied (say, $|\text{Re}\Delta E|<0.0001\ |\text{Re}E_\lambda|$, $|\text{Im}\Delta E|<0.0001\ |\text{Im}E_\lambda|$), the real eigenvalue of the final bound state of the capture transition can be determined by similar methods, except that the solution $\mathcal{V}_{\text{in}}$ is started from its asymptotic form, the spherical Hankel function. With the definitive eigenvalues, the eigensolutions are reconstituted in parallel by numerical integration, normalization integrals and the radial overlap integral are formed, and finally the real and imaginary values of the normalized wave function at the channel radius, $V_q(a)$, with the phase ω_q set to zero are determined. (Note that this is a different convention from that used in the development of Sec. XI B, in which $V_q(a)$ is made real.)

Using the computer program, we have calculated the optical model $\mathcal{R}$-function eigenvalue for a few typical cases, concentrating on a nucleus $A=57$ close to the $3s$ neutron strength function resonance, on two nuclei ($A=50$ and 62) at half-maximum points with respect to this resonance, and on an off-resonance case $A=40$ near the sulfur region. We have used the parametrization given in Sec. XII for the volume absorption and narrowly-peaked surface absorption models. A typical set of eigenstates for the $A=57$ volume absorption case is shown in Table A.I and for the $A=40$ surface absorption case in Table A.II. From these, the strength function, $\mathcal{R}^\infty$, and capture amplitudes can be calculated according to Eqs. (41) and (47). (In substituting in these equations, because of the different convention on ω_q, the quantity $V_q(a)$ in the equation is taken to be the modulus of its value in the table, and ω_q the phase of the tabulated value). The calculated potential scattering and capture cross sections and the neutron and valence radiation strength functions are compared with direct optical model calculations in Table A.III.

TABLE A.I. $\mathcal{R}$-matrix states for the $A=57$ volume absorption case and $a_c=8.59$ fm.

E_q-iW_q(MeV)	$V_q(a_c)$ $[(10^{-12}\,\text{cm})^{-3/2}]$	$M_q e^{-i\phi_q}[(10^{-12}\,\text{cm})^{-3/2}]$
−33.88 − i2.329	0.0165 − i0.0031	−0.573 + i0.226
−15.42 − i1.875	0.208 − i0.0412	−1.613 − i0.252
−0.137 − i0.716	1.660 − i0.100	−0.234 − i0.022
11.64 − i1.157	1.940 + i0.043	0.0006 − i0.0093
33.34 − i1.297	1.721 + i0.012	0.0462 − i0.0031
61.00 − i1.363	1.727 + i0.303	0.0494 − i0.0119

TABLE A.II. $\mathcal{R}$-matrix states for the $A=40$ surface absorption case and $a_c=9.57$ fm.

E_q-iW_q(MeV)	$V_q(a_c)$ $[(10^{-12}\,\text{cm})^{-3/2}]$	$M_q e^{-i\phi_q}[(10^{-12}\,\text{cm})^{-3/2}]$
−31.77 − i0.769	0.00354 + i0.00135	−1.720 − i8.467
−10.78 − i4.811	0.1123 − i0.0741	−2.125 − i1.485
1.143 − i0.069	1.733 − i0.016	−0.292 − i0.004
10.61 − i1.33	1.721 − i0.117	−0.0056 − i0.016
27.36 − i2.85	1.617 + i0.099	−0.0100 + i0.0295
50.01 − i0.56	1.562 + i0.016	−0.0967 − i0.0005
76.97 − i2.60	1.525 − i0.033	−0.0945 − i0.0115
108.9 − i1.33	1.517 + i0.039	−0.0964 + i0.0039

TABLE A.III. Results of calculations of cross sections and strength functions using the $\mathcal{R}$-matrix parameters of Tables A.I and A.II compared with results of optical model calculations employing direct integration of the Schrödinger equation.

	Optical model direct calculation				Optical model $\mathcal{R}$-matrix calculation			
	$4\pi a_{\text{pot}}^2$ (b)	$\Gamma_{\lambda(n)}^{(0)}/D_J$	$\sigma_{\gamma,\text{pot}}$ (b)	$\Gamma_{\gamma,\text{val}}/D_J E_\gamma^3$ (MeV^{-3})	$4\pi a_{\text{pot}}^2$ (b)	$\Gamma_{\lambda(n)}^{(0)}/D_J$	$\sigma_{\gamma,\text{pot}}$ (b)	$\Gamma_{\gamma,\text{val}}/D_J E_\gamma^3$ (MeV^{-3})
$A = 57$	8.7	11.3×10^{-4}	0.11	33.4×10^{-8}	8.4	11.2×10^{-4}	0.05	33.6×10^{-8}
$A = 40$	0.94	0.39×10^{-4}	0.62	3.8×10^{-8}	1.25	0.40×10^{-4}	0.55	3.4×10^{-8}

The difference in the ratio of real and imaginary parts of the capture amplitude calculated in these two ways gives us a measure of the accuracy in calculating the background potential capture cross section and the average resonance valency cross section from the optical model according to the prescription of Sec. XI B. Near the 3s neutron strength function resonance, where the background capture cross section is very low, it turns out that this prescription is not too poor; even for the strongly peaked surface absorption model, agreement is to within $\approx$ 30%. On the slopes of the surface strength function resonance, where the background capture cross section reaches its maximum, and beyond, agreement is generally better than 20%.

APPENDIX B

Optical model computations of capture cross sections

We have computed the capture cross sections within the framework of the optical model using a Fortran computer program CPCEI. Specified input parameters are the optical model parameters of Eqs. (57) and (58), the neutron energy E, the state of orbital angular momentum l, and spin-orbit coupled angular momentum j_l, a rough estimate of the eigenvalue E_f of the final state, its orbital angular momentum k, and spin-orbit coupled angular momentum j_k. A starting radius r', where the potential is assumed constant, and a finishing radius a, beyond which the potential can be assumed to be zero, are also given as input.

The final-state eigenvalue for the radial part of the Schrödinger equation

$$-\frac{\hbar^2}{2m}\frac{\partial^2 w_f}{\partial r^2}+[\mathcal{V}(r)+\mathcal{V}_{\text{so}}(r,k,j_k)-E_f]w_f+\frac{\hbar^2 k(k+1)}{2mr^2}w_f=0 \quad \text{(B.1)}$$

is computed in a similar way to that described in CPBDY (Appendix A). The value of ρ used for the starting value of $w_{f,\text{in}}$, namely $\rho j_l(\rho)$ and its derivative, is equal to $r'\{2m[E_f-\mathcal{V}(r')]/\hbar^2\}^{1/2}$. The starting value of the logarithmic derivative is not taken from a specified boundary condition in this case, but from the asymptotic solution $w_{f,\text{out}}(r)\sim\kappa r h_k(\kappa r)$, where $h_k(\kappa r)$ is the spherical Hankel function and $\kappa=\{2m|E_f|/\hbar^2\}^{1/2}$. The two solutions are integrated to $r''=R$ and the eigenvalue correction is calculated according to Eq. A.15.

The wave function of the Schrödinger equation for a neutron at energy E within the complex potential,

$$-\frac{\hbar^2}{2m}\frac{\partial^4\psi}{\partial r^2}+[\mathcal{U}(r)+\mathcal{V}_{\text{so}}(r,l,j_l)-E]\psi+\frac{\hbar^2 l(l+1)}{2mr^2}\psi=0 \quad \text{(B.2)}$$

is then computed by straightforward methods (a Runge-Kutta routine is good enough), starting from the logarithmic derivative of the solution at small $r(r=r')$, where $\mathcal{U}(r)$ is assumed constant. This solution is $Krj_l(Kr)$, where K is the complex wave number $K=\{2m[E-\mathcal{U}(r')]/\hbar^2\}^{1/2}$. As this wave function is developed, the eigenfunction of the bound state f is calculated and Simpson quadrature is performed to form normalization integrals and the radial dipole overlap integral.

When the wave function is finally calculated out to $r=a$, its value and derivative there are used in conjunction with the values and derivatives of incoming waves I_l and outgoing waves O_l, calculated from spherical Bessel and Neumann functions,

$$I_l=-i\rho[j_l(\rho)-in_l(\rho)];\ O_l=-i\rho[j_l(\rho)-in_l(\rho)] \quad \text{(B.3)}$$

(where $\rho=kr$, and the wave number $k=\{2mE/\hbar^2\}^{1/2}$), to give the optical model collision function, $U_{l,\text{opt}}$ [c f. Eq. (44)]:

$$U_{l,\text{opt}}=\frac{I_l(\partial\psi/\partial r)-\psi(\partial I_l/\partial r)}{O_l(\partial\psi/\partial r)-\psi(\partial O_l/\partial r)}. \quad \text{(B.4)}$$

From the collision function, the optical model total cross section (tot), shape elastic (se), and compound nucleus (cn) formation cross sections can be calculated:

$$\sigma_{\text{opt}}(\text{tot})=(2\pi/k^2)(2l+1)(1-\text{Re}U_{l,\text{opt}}), \quad \text{(B.5)}$$

$$\sigma_{\text{opt}}(\text{se})=(\pi/k^2)(2l+1)|1-U_{l,\text{opt}}|^2 \quad \text{(B.6)}$$

$$\sigma_{\text{opt}}(\text{cn}) = (\pi/k^2)(2l + 1)(1 - |U_{l,\text{opt}}|^2) . \quad \text{(B.7)}$$

If the spin-orbit coupling representation is adhered to, the factor $(2l + 1)$ in the above equations is replaced by $(2j_l + 1)/2$.

The last quantity can be used to give the optical model transmission coefficient, T_l, normally defined by $\sigma_{\text{opt}}(\text{cn}) = (\pi/k^2)(2l + 1)T_l$, which in the low-energy limit reduces to $2\pi\bar{\Gamma}_l/\bar{D}_l$, giving a simple relation to the strength function s_l, namely $T_l = 4\pi P_l s_l$, but the latter can be better defined as the imaginary part of the $\mathcal{R}$ function [cf. Eqs. (12) and (34a)]. The real part of the $\mathcal{R}$ function, $\mathcal{R}_l^{\infty}$, gives the potential scattering cross section which, for low-energy s waves, is $\sigma_{\text{pot}} = 4\pi a^2(1 - \mathcal{R}_o^{\infty})^2$. It should be noted that this is not identical to the optical model shape elastic scattering cross section, which is greater by an amount $4\pi a^2 \cdot \pi^2 s_o^2$. The results of the calculations are employed in Figs. 9–16.

APPENDIX C

Specialized optical models for analyzing S data

The range of optical model potentials giving the specific value of $\mathcal{R}_{\text{opt}}^{\infty}$ (equal to the value of $\mathcal{R}_J$ observed in thermal neutron scattering) for three of the S isotopes and the corresponding ranges of E_f and C_{opt} are shown in the Table below. Note that in the case of $^{33}\text{S} + n$ for which $\sigma_{\text{th,coh}} \approx \sigma_{\text{th, total}} \approx 2.6$ b (hence $\mathcal{R}_J \approx -0.07$ for both values of initial state spin), values of C_{opt} can only be determined from the second branch of $\mathcal{R}_{\text{opt}}^{\infty}$.

TABLE C.I. Range of specialized C_{opt} factors

Target	$\mathcal{R}_{\text{opt}}^{\infty}$	$J_f = 3/2$ E_f	$\mathcal{V}_0$	$\mathcal{W}_0$	C_{opt}	$J_f = 1/2$ E_f	$\mathcal{V}_0$	$\mathcal{W}_0$	C_{opt}
^{32}S	0.366 (branch 1)	−5.05 ↕ −2.9	−51 ↕ −46.7	−5 ↕ −1.25	1.43 ↕ 1.44	−2.3 ↕ −0.8	−51 ↕ −46.7	−4 ↕ −1.25	1.28 ↕ 1.10
	0.366 (branch 2)	−6.5 ↕ −7.2	−53.7 ↕ −55	−4 ↕ −2.5	1.33 ↕ 1.28	−0.34 ↕ −4.0	−51 ↕ −47.3	−4 ↕ −2.5	1.27 ↕ 1.24
^{34}S	0.213 (branch 1)	−4 ↕ −2.1	−48.9 ↕ −44.8	−6 ↕ −1.25	1.49 ↕ 1.42	−1.6 ↕ −0.28	−48.9 ↕ −44.8	−6 ↕ −1.25	1.26 ↕ 0.95
	0.213 (branch 2)	−5.1 ↕ −7.3	−51 ↕ −55	−6 ↕ −2.5	1.46 ↕ 1.29	−2.3 ↕ −3.7	−51 ↕ −54.3	−6 ↕ −4	1.30 ↕ 1.28
^{33}S	−0.07 (branch 2)	−4.9 ↕ −7.2	−50.7 ↕ −55.1	−10 ↕ −4	1.60 ↕ 1.38	−2.2 ↕ −4.05	−50.7 ↕ −55.1	−10 ↕ −4	1.38 ↕ 1.37

*Permanent address: Middle Tennessee State University, Murfreesboro, Tennessee 37132.

†Permanent address: Tennessee Technological University, Cookeville, Tennessee 38501.

‡Permanent address: Atomic Energy Research Establishment, Harwell, England.

[1]S. Raman, E. T. Jurney, D. A. Outlaw, and I. S. Towner, Phys. Rev. C **27**, 1188 (1983).

[2]S. Raman, W. Ratynski, E. T. Jurney, M. E. Bunker, and J. W. Starner, Phys. Rev. C **30**, 26 (1984).

[3]R. F. Carlton, S. Raman, and E. T. Jurney, Bull. Am. Phys. Soc. **24**, 818 (1979); S. Raman, R. F. Carlton, and E. T. Jurney, contributed paper in *Proceedings of the International Conference on Nuclear Physics* (Berkeley, 1980) p. 236; R. F. Carlton, S. Raman, and E. T. Jurney, Bull. Am. Phys. Soc. **25**, 543 (1980); S. Raman, W. Ratynski, and E. T. Jurney, in *Neutron Capture Gamma Ray Spectroscopy and Related Topics 1981,* edited by T. von Egidy, F. Gönnenwein, and B. Maier (Institute of Physics, Bristol, 1982), p. 169.

[4]A. M. Lane and J. E. Lynn, Nucl. Phys. **17**, 563 (1960); **17**, 686 (1960). J. E. Lynn, *The Theory of Neutron Resonance Reactions* (Clarendon, Oxford, 1968).

[5]J. Cugnon and C. Mahaux, Ann. Phys. (N.Y.) **94**, 128 (1975).

[6]B. J. Allen and A. R. de L. Musgrove, in *Advances in Nuclear Physics, edited* by M. Baranger and E. Vogt (Plenum, New York 1978), Vol. 10, p. 129.

[7]S. F. Mughabghab, R. E. Chrien, O. A. Wasson, G. W. Cole, and M. R. Bhat, Phys. Rev. Lett. **26**, 1118 (1971).
[8]R. E. Chrien, G. W. Cole, G. G. Slaughter, and J. A. Harvey, Phys. Rev. C **13**, 578 (1976).
[9]S. Raman, G. G. Slaughter, J. C. Wells, Jr., and B. J. Allen, Phys. Rev. C **22**, 328 (1980).
[10]A. M. Lane, Phys. Lett. **31B**, 344 (1970); Ann. Phys. (N.Y.) **63**, 171 (1971); Phys. Lett. **50B**, 204 (1974).
[11]A. M. Lane and S. F. Mughabghab, Phys. Rev. C **10**, 412 (1974).
[12]S. F. Mughabghab, Phys. Lett. **81B**, 93 (1979).
[13]J. Kopecky, A. M. J. Spits, and A. M. Lane, Phys. Lett. **49B**, 323 (1974).
[14]L. G. Smith and A. H. Wapstra, Phys. Rev. C **11**, 1392 (1975); A. H. Wapstra, in *Proceedings of the Second International Conference on Neutron Capture Gamma Ray Spectroscopy,* edited by K. Abrahams, F. Stecher-Rasmussen, and P. van Assche (Reactor Centrum Nederland, Petten, 1975), p. 686.
[15]E. R. Cohen and A. H. Wapstra, Nucl. Instrum. Methods **211**, 153 (1983).
[16]S. F. Mughabghab and D. I. Garber, *Neutron Cross Sections, Volume I, Resonance Parameters,* Brookhaven National Laboratory Report BNL-325 (1973).
[17]S. Raman, in *Neutron Capture Gamma Ray Spectroscopy and Related Topics 1981,* edited by T. von Egidy, F. Gönnenwein, and B. Maier (Institute of Physics, Bristol, 1982), p. 357.
[18]J. D. Jafar, A. A. Abdullah, N. K. Al-Kuraishi, M. S. Alvash, M. A. Khalil, and A. M. Demidov, Yad. Fiz. **15**, 1039 (1972) [Sov. J. Nucl. Phys. **15**, 605 (1972)]. In the AIP translation, the name of the first author is misspelled as Dzh. D. Dzhafar.
[19]R. Abegg and S. K. Datta, Nucl. Phys. A **287**, 94 (1977).
[20]Š. Piskoř, P. Franc, J. Křemének, and W. Schäferlingová, Nucl. Phys. **A414**, 219 (1984).
[21]M. A. Lone, R. A. Leavitt, and D. A. Harrison, At. Data Nucl. Data Tables **26**, 483 (1981); U. Reus and W. Westmeir, ibid **29**, 2 (1983).
[22]A. Guichard, H. Nann, and B. H. Wildenthal, Phys. Rev. C **12**, 1109 (1975).
[23]Th. W. van der Mark and L. K. ter Veld, Nucl. Phys. **A181**, 196 (1972).
[24]R. M. Freeman, R. Faerber, M. Toulemonde, and A. Gallman, Nucl. Phys. **A197**, 529 (1972).
[25]P. M. Endt and C. van der Leun, Nucl. Phys. **A310**, 1 (1978).
[26]A. H. Wapstra and K. Bos, At. Data and Nucl. Data Tables **19**, 177 (1977).
[27]G. E. Thomas, D. E. Blatchley, and L. M. Bollinger, Nucl. Instrum. Methods **56**, 325 (1967).
[28]D. J. Crozier, Nucl. Phys. **A198**, 209 (1972).
[29]V. R. Burmistrov, Izv. Akad. Nauk SSSR (ser. fiz.) **23**, 898 (1959).
[30]G. van Middelkoop and P. Spilling, Nucl. Phys. **72**, 1 (1965); G. van Middelkoop and H. Gruppelaar, Nucl. Phys. **80**, 321 (1966).
[31]T. J. Kennett, N. P. Archer, and L. B. Hughes, Nucl. Phys. **A96**, 658 (1967).
[32]P. M. Endt and C. H. Paris, Phys. Rev. **110**, 89 (1958).
[33]M. C. Mermaz, C. A. Whitten, Jr., J. W. Champlin, A. J. Howard, and D. A. Bromley, Phys. Rev. C **4**, 1778 (1971).
[34]S. F. Mughabghab, M. Divadeenam, and N. E. Holden, *Neutron Cross Sections,* Vol. 1 (Academic, New York 1981), p. 16-6.
[35]A. Arbildo and J. C. Robertson, Trans. Am. Nucl. Soc. **46**, 757 (1984).
[36]L. Seren, H. N. Friedlander, and S. H. Turkel, Phys. Rev. **72**, 888 (1947).
[37]R. W. Durham and F. Girardi, Nuovo Cimento Suppl. **19**, 4 (1961).
[38]D. S. Kappe, Dissertation Abstr. B **27**, 919 (1966).
[39]H. Ishikawa, Nucl. Instrum. Methods **109**, 493 (1973).
[40]Y. K. Ho and M. A. Lone, Nucl. Phys. **A406,** 1 (1983); **A406,** 18 (1983).
[41]H. Feshbach, C. E. Porter, and V. F. Weisskopf, Phys. Rev. **96,** 448 (1954).
[42]A. A. Ross, H. Mark, and R. D. Lawson, Phys. Rev. **102**, 1613 (1956).
[43]P. A. Moldauer, Nucl. Phys. **47**, 65 (1963); The effect of the diffuseness parameter on the strength function has been discussed by E. Vogt, Rev. Mod. Phys. **34**, 723 (1962).
[44]C. E. Thorn, J. W. Olness, E. K. Warburton, and S. Raman, Phys. Rev. C**30**, 1442 (1984).
[45]L. Koester, K. Knopf, and W. Waschkowski, Z. Physik A **289**, 399 (1979).
[46]M. C. Moxon, private communication.
[47]A. G. W. Cameron, Can. J. Phys. **37**, 322 (1959).
[48]J. Halperin, C. H. Johnson, R. R. Winters, and R. L. Macklin, Phys. Rev. C **21**, 545 (1980).
[49]J. R. Bird, B. J. Allen, I. Bergqvist, and J. A. Biggerstaff, At. Data Nucl. Data Tables, **11**, 456 (1973).
[50]C. E. Porter, Phys. Rev. **100**, 935 (1955).